Tubulin biochemistry confers intrinsic differences in microtubule dynamics and drug sensitivity between species

DISSERTATION

zur Erlangung des akademischen Grades

Doctor rerum naturalium

(*Dr. rer. nat.*)

eingereicht an der

Lebenswissenschaftlichen Fakultät der Humboldt-Universität zu Berlin

von

M.Sc., William Graham Hirst

Präsidentin der Humboldt-Universität zu Berlin:

Prof. Dr.-Ing. Dr. Sabine Kunst

Dekan der Lebenswissenschaftlichen Fakultät der Humboldt-Universität zu Berlin:

Prof. Dr. Dr. Christian Ulrichs

Gutachter:

1. Prof. Dr. Simone Reber

2. Prof. Dr. Kai Matuschewski

3. Prof. Dr. Kevin Saliba

Tag der mündlichen Prüfung: 19. Mai 2021

Declaration

I hereby declare that except where specific reference is made to the work of others, the contents of this dissertation are original and have not been submitted in whole or in part for consideration for any other degree or qualification in this, or any other university. This dissertation is my own work and contains nothing which is the outcome of work done in collaboration with others, except as specified in the text and Acknowledgements. I further declare that no collaboration with commercial institutions or doctoral degree supervisors took place.

Ich erkläre hiermit, dass der Inhalt dieser Dissertation, sofern nicht ausdrücklich auf die Arbeit anderer verwiesen wird, original ist und weder ganz noch teilweise für einen anderen Abschluss oder eine andere Qualifikation an dieser oder einer anderen Universität eingereicht wurde. Diese Dissertation ist meine eigene Arbeit und enthält nichts, was das Ergebnis der Arbeit ist, die in Zusammenarbeit mit anderen durchgeführt wurde, außer wie im Text und in den Anerkennungen angegeben. Ich erkläre ferner, dass keine Zusammenarbeit mit kommerziellen Einrichtungen oder Betreuern stattgefunden hat.

William Hirst
November 2020

Acknowledgements

First and foremost, I would like to thank Simone for her mentorship throughout the past several years and for instilling in me the confidence to focus my efforts into this doctoral thesis. I am grateful that you have both challenged me to improve and have advocated for me throughout this process, and for consistently supporting and guiding me to become a better scientist.

I would like to thank Kevin Saliba for welcoming me to your lab during my exchange at the ANU in Australia and for your perspective and support during my stay and since then. Although the time was short, the experience was valuable and an essential part of the work I've built upon since then.

I would also like to thank Kai Matuschewski for supporting me from the start of this project, for hosting me at Molecular Parasitology, and for your valuable mentorship and advice throughout.

This work was also made possible by the contributions of time and resources of several collaborators, whom I would additionally like to acknowledge. Thank you to Jacob Baum and his lab for the *Plasmodium* cell culture, which provided the basis for the first large-scale *P.falciparum* tubulin purification and subsequent *in vitro* experiments. Thank you to Kishore Mahalingan of the NIH and Chris Weise and Benno Kuropka of the BioSupraMol at the FU Berlin for contributing the mass spectrometry measurements, and for your help in interpreting the data. Thank you to the Görlich lab, in particular Bastian Hülsmann and Jens Krull, for hosting us at the MPI-BPC and providing support for the *Xenopus tropicalis* tubulin purifications. Thank you to Jan Schmoranzer and the rest of the AMBIO team for your support, troubleshooting, and advice during the many hours of microscopy at the AMBIO facility.

I would like to thank my fellow lab members Abin, Sebastian, Tobias, Ella, Christoph, Dominik, and Soma for making this experience as enjoyable as it was and for being great people to work with. In particular I would like to thank Abin for his contributions to the work we did together on the *Current Biology* paper and the data you contributed that are referenced in this work.

Finally, I would like to thank my partner Anna for being a constant source of support and positivity and for helping me to navigate this process through these strange and confusing pandemic times.

List of Publications

Work completed since the beginning of the doctoral thesis has been published in:

1. **William G. Hirst**, Christine Kiefer, Mohammad K. Abdosamadi, Erik Schäffer, Simone Reber. In vitro Reconstitution and Imaging of Microtubule Dynamics by Fluorescence and Label-free Microscopy. *STAR Protoc*. (Accepted, Editorial Decision STAR-PROTOCOLS-D-20-00136R3)

2. Sebastian Reusch, Abin Biswas, **William G. Hirst**, Simone Reber. Affinity Purification of Label-free Tubulins from *Xenopus* Egg Extracts. *STAR Protoc. 1,* 100151 (2020).

3. **Hirst, W. G.**, Biswas, A., Mahalingan, K. K. & Reber, S. Differences in Intrinsic Tubulin Dynamic Properties Contribute to Spindle Length Control in Xenopus Species. *Curr. Biol*. 30, 2184-2190.e5 (2020).

4. Camargo Ortega G, Falk S, Johansson PA, Peyre E, Broix L, Sahu SK, **Hirst W**, Schlichthaerle T, De Juan Romero C, Draganova K, Vinopal S, Chinnappa K, Gavranovic A, Karakaya T, Steininger T, Merl-Pham J, Feederle R, Shao W, Shi SH, Hauck SM, Jungmann R, Bradke F, Borrell V, Geerlof A, Reber S, Tiwari VK, Huttner WB, Wilsch-Bräuninger M, Nguyen L, Götz M. The centrosome protein AKNA regulates neurogenesis via microtubule organization. *Nature* 567, 113–117 (2019).

5. Kapoor, V., **Hirst, W. G.**, Hentschel, C., Preibisch, S. & Reber, S. MTrack: Automated Detection , Tracking , and Analysis of Dynamic Microtubules. *Sci. Rep*. 1–12 (2019).

Of these publications, parts of this dissertation have been published in (1), (2), and (3).

Summary

Microtubules are filamentous intracellular polymers that are fundamental components of subcellular structures including the spindle, the cytoskeleton, and flagella in eukaryotes. Recent advances in tubulin purification techniques have begun to shed light on the importance of tubulin's intrinsic biochemical and dynamic properties and how they vary in different species and cell types independent of the activities of microtubule-associated proteins. This study uses a comparative approach to investigate how the intrinsic dynamic and biochemical characteristics of tubulin vary between species, and demonstrates their consequences in two different physiological contexts: 1) Spindle size control in *Xenopus* frogs, and 2) The specificity of microtubule inhibitors for *Plasmodium falciparum* microtubules over those of their human host.

In *Xenopus* frog eggs, the length of the meiotic spindle is biochemically controlled and reaches an upper limit independent of spatial constraints. Spindle lengths of *Xenopus tropicalis* frogs are approximately 30% shorter than those of the closely related *Xenopus laevis*. Some spindle proteins have been identified that contribute to the difference in spindle length; however, the role of intrinsic tubulin dynamics in setting spindle length has yet to be addressed. In this study, tubulin was purified from *X. laevis* and *X. tropicalis* egg extracts and dynamic microtubules were assembled *in vitro.* Measurements of *Xenopus* microtubule dynamics show that *X. laevis* microtubules are both faster-growing and longer-lived, independent of the influence of microtubule-associated proteins. Furthermore, quantification of *Xenopus* microtubule length and mass distributions, combined with egg extract spindle assembly reactions, establishes a role for intrinsic microtubule dynamics in modulating spindle length.

Microtubules are established drug targets in fungal and parasitic helminth infections and have in the past decades drawn attention as a potential drug target in the malaria parasite *Plasmodium falciparum.* Attempts to characterize drug-protein interactions and *Plasmodium* microtubule biochemistry *in vitro* have been hindered by the difficulty of purifying active parasite tubulin. In order to characterize *P. falciparum* microtubule dynamics, structure, and drug specificity, we have used an affinity chromatography-based approach to purify tubulin directly from blood-stage parasites. Tubulin purified by this method is assembly-competent and free of host protein contamination. For the first time, dynamic *P. falciparum* microtubules have been

reconstituted *in vitro* and parasite-specific suppression of microtubule dynamics by oryzalin and amiprofos methyl has been directly demonstrated. This study establishes an experimental framework to directly test for parasite-specific microtubule inhibition, microtubule structure, and interactions with MAPs that previously have not observed using existing *in vitro* approaches.

Zusammenfassung

Mikrotubuli sind filamentöse intrazelluläre Polymere, die als grundlegende Bestandteile subzellulärer Strukturen wie der Spindel, des Zytoskeletts und der Flagellen in Eukaryoten dienen. Jüngste Fortschritte bei der Tubulinreinigungstechnik haben begonnen, die Bedeutung der intrinsischen biochemischen und dynamischen Eigenschaften von Tubulin und ihre Unterschiede bei verschiedenen Arten und Zelltypen unabhängig von den Aktivitäten von Mikrotubuli-assoziierten Proteinen aufzuklären. Diese Studie verwendet einen vergleichenden Ansatz, um zu untersuchen, wie sich die intrinsischen dynamischen und biochemischen Eigenschaften von Tubulin zwischen verschiedenen Spezies unterscheiden, und zeigt ihre Konsequenzen in zwei verschiedenen physiologischen Kontexten: 1) Bestimmung der Spindelgröße bei Fröschen der Gattung *Xenopus* und 2) Spezifität von Mikrotubuli-Inhibitoren für *Plasmodium falciparum*-Mikrotubuli über denen ihres menschlichen Wirts.

In den Eiern der Froschgattung *Xenopus* wird die Länge der meiotischen Spindel biochemisch festgelegt und erreicht unabhängig von räumlichen Einschränkungen eine Obergrenze. Die Spindellängen von *Xenopus tropicalis*-Fröschen sind ungefähr 30% kürzer als die der eng verwandten *Xenopus laevis*. Es wurden einige Spindelproteine identifiziert, die das Unterschied in der Spindellänge beeinflussen. Die Rolle der intrinsischen Tubulindynamik bei der Einstellung der Spindellänge muss jedoch noch untersucht werden. In dieser Studie wurde Tubulin aus *X. laevis*- und *X. tropicalis*-Eiextrakten aufgereinigt und dynamische Mikrotubuli wurden *in vitro* zusammengesetzt. Messungen der Dynamik von *Xenopus*-Mikrotubuli zeigen, dass *X. laevis*-Mikrotubuli unabhängig vom Einfluss von mikrotubuliassoziierten Proteinen sowohl schneller wachsen als auch länger leben. Darüber hinaus spielt die Quantifizierung der Länge und Massenverteilung der *Xenopus*-Mikrotubuli zusammen mit den Reaktionen der Eiextrakt-Spindelanordnung eine Rolle für die intrinsische Dynamik der Mikrotubuli bei der Modulation der Spindellänge.

Mikrotubuli sind ausgewiesene Wirkstofftargets bei Pilz- und parasitären Helmintheninfektionen und haben in den letzten Jahrzehnten die Aufmerksamkeit als potenzielles Wirkstoffziel beim Malariaparasiten *Plasmodium falciparum* auf sich gezogen. Versuche, Arzneimittel-Protein-Wechselwirkungen und die Biochemie von *Plasmodium*-Mikrotubuli *in vitro* zu charakterisieren, wurden durch die Schwierigkeit der

Reinigung von aktivem Parasitentubulin gehemmt. Um die Dynamik, Struktur und Spezifität von Mikrotubuli von *P. falciparum* zu charakterisieren, haben wir eine auf Affinitätschromatographie basierende Methode verwendet, um Tubulin direkt von Parasiten in der Blutphase zu reinigen. Mit dieser Methode gereinigtes Tubulin ist aktiv und frei von Kontaminationen des Wirtsproteins. Zum ersten Mal wurden hier dynamische *P. falciparum*-Mikrotubuli *in vitro* rekonstituiert und eine parasitenspezifische Unterdrückung der Dynamik von Mikrotubuli durch Oryzalin und Amiprofos-Methyl direkt nachgewiesen. Diese Studie legt einen experimentellen Rahmen fest, um direkt auf parasitenspezifische Hemmung von Mikrotubuli, Mikrotubuli-Struktur und Wechselwirkungen mit MAPs zu testen, die bisher unter Verwendung bestehender *in-vitro*-Ansätze nicht beobachtet wurden.

Chapter 1. Introduction to Tubulin, Microtubules, and the Tubulin Code

1.1 Microtubule Dynamics in the Cell

Microtubules are dynamic filaments formed by the polymerization of α/β-tubulin heterodimers that form the structural basis of the interphase cytoskeleton, flagella, and the spindle. Central to microtubule function is the phenomenon of dynamic instability, whereby individual microtubules stochastically alternate between phases of polymerization and depolymerization[1,2] (Figure 1). Microtubule dynamics are carefully regulated and vary greatly depending on species, cell type, developmental stage, and cell cycle stage.

Microtubule dynamic instability is driven by tubulin interactions with GTP. As a soluble protein, tubulin exists as an obligate heterodimer of α- and β- tubulin subunits. The subunits each bind one molecule of GTP, one in the nonexchangeable N-site of α-tubulin, and the other at the exchangeable E-site of β-tubulin[3,4]. At the plus-end of the microtubule, the α-tubulin subunit of GTP-bound tubulin binds the exposed β-tubulin at the end of a growing protofilament, followed by stabilizing lateral interactions with other protofilaments that form concurrently and wrap together to give the microtubule its tubular shape. The region of GTP-bound tubulin at the growing end of a microtubule is known as the GTP cap, which confers stability to the microtubule. Over time, GTP is hydrolyzed within the microtubule, which induces a conformational change that destabilizes the microtubule lattice. Loss of the GTP cap results in a switch from growth to shrinkage, called a catastrophe, whereas GTP-bound tubulin remaining in the lattice halts shrinkage and induces a switch back to growth, called a rescue[5,6]. Thus, dynamic instability is an intrinsic property of the microtubule polymer mediated by GTP hydrolysis-induced structural changes in the tubulin dimer.

In addition to the intrinsic dynamic properties of microtubules, cells modulate microtubule dynamics in order to perform diverse functions. In spindles, individual microtubules have an average lifetime of around 20 seconds and bulk microtubule turnover falls within the range of $t_{1/2}$ = 100 s, whereas axonal microtubules in neurons have a turnover half-life of several hours[7–10]. Microtubules show an increase in growth rate combined with more frequent catastrophes and less frequent rescues, and therefore

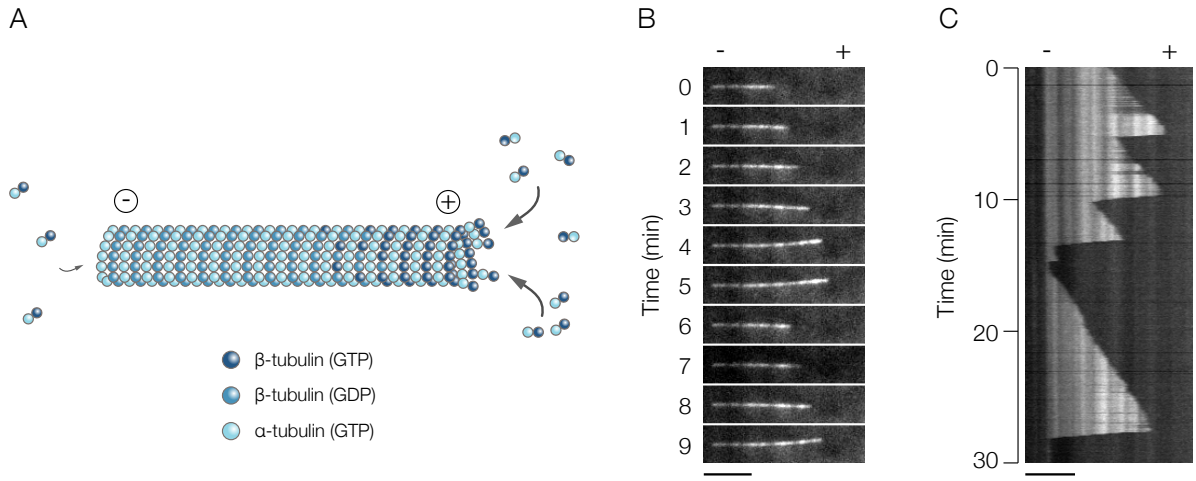

Figure 1.1 Dynamic instability of microtubules. (A) Schematic of a microtubule. Tubulin exists in solution as an α/β tubulin dimer, which is incorporated into the microtubule lattice. As the microtubule ages, β-tubulin hydrolyzes GTP to GDP. GTP-bound tubulin forms the stable GTP cap of the growing microtubule, whereas GDP-bound tubulin is and unstable component of the microtubule and will depolymerize if the GTP cap is lost. (B) Time-lapse montage of an individual fluorescently labeled microtubule imaged by total internal reflection fluorescence (TIRF) microscopy over the course of 9 minutes. (C) A kymograph generated from the video of the same microtubule depicted in (B) over the course of 30 minutes. The depictions in (B) and (C) begin at the same timepoint. The orientation of the plus (+) and minus (-) ends of the microtubule are indicated. The scale bar represents 5 μm.

a higher turnover, during mitosis compared to interphase[11,12]. This reflects the need for longer-lived microtubules that confer cellular structure and facilitate transport during interphase versus the high-turnover environment that enables relatively rapid remodeling of microtubule networks during mitosis. Even within organelles, microtubule dynamics are differentially regulated among subpopulations of microtubules. For example, microtubules near the spindle equator have a higher rate of turnover than those near the spindle pole in budding yeast, which has been shown to be a determinant of proper kinetochore positioning[13]. In neurons, microtubules near the axon terminus and within the dendrites undergo frequent remodeling as a result of frequent severing-induced catastrophes, which is necessary for branching in these structures. At the same time, stable microtubule populations are maintained within the axon proximal to the cell body in order to facilitate intracellular transport. In sum, spatiotemporal control of microtubule dynamics is an essential feature of microtubule function.

For the past several decades, microtubule-associated proteins (MAPs) and motor proteins have been the main focus of investigations into the regulation of microtubules and the structures they form in the cell. However, tubulin is present as a heterogeneous mixture of different isoforms that are further subject to post-translational modifications, and an increasing body of evidence is beginning to reveal the functional importance of the biochemical diversity of the tubulin molecule, otherwise known as the "tubulin code."[14–16]

1.2 Post-translational Modifications of Tubulin

Post-translational modifications (PTMs) of tubulin influence microtubule dynamics both by influencing interactions with MAPs and by changing structural characteristics of the microtubule lattice itself. The disordered c-terminal tail of tubulin is located on the outer surface of microtubules and is the site of many PTMs that modulate interactions with MAPs and motor proteins.

Recent studies have begun to clarify the mechanistic basis for some PTMs' influence on microtubule dynamics and organization. For example, polyglutamylation determines the extent to which microtubules are severed by spastin, an ATPase that induces microtubule breakage by removing tubulin subunits from within the microtubule via interactions with the c-terminal tails of tubulin that decorate the lattice surface to regulate microtubule mass and number[17,18]. Other modifications are found in the structured core of tubulin and can influence the material properties of microtubules. Acetylation of lysine 40 of α-tubulin is a hallmark modification of stable axonal and cytoskeletal microtubules and has been shown to render microtubules resistant to breakage by mechanical stress[19,20]. Tubulin acetylation is correlated with longer lifetimes of cytoskeletal microtubules in vivo and lower rates of microtubule nucleation in vitro, which are both characteristics of decreased microtubule turnover[19,20]. Disruption of TgATAT, the enzyme responsible for acetylating tubulin in *Toxoplasma gondii*, has also been shown to produce replication defects in the organism[21]. However, this does not rule out the effects on other potential TgATAT substrates, and the study lacked experiments using purified tubulin, which would have enabled the authors to test whether the modification truly stabilizes *T. gondii* microtubules or whether it mediates interactions with other proteins. Modifications such as K40 acetylation and glutamylation appear in a

number of different species and cell types, and there still remains much to be learned about their roles in different contexts.

Many other PTMs have been identified whose functions are less clear, largely because of a lack of direct biochemical evidence. The biochemical studies of modified tubulin to date reflect a small fraction of the PTMs and their potential functions that have been identified, and further in vitro work in this vein will be critical for understanding how PTMs influence microtubule dynamics and the consequences for the cell.

1.3 Tubulin Has Many Isoforms

Isotypically pure tubulin purified from cell types containing few isoforms or recombinantly expressed and purified from insect cells has also revealed the contributions of individual tubulin isoforms. The βIII isoform, which is prevalent in and specific to mammalian neurons[22,23], has been shown to decrease the growth rate and increase the catastrophe frequency of microtubule plus ends while stabilizing the minus ends when titrated into mixtures containing the non-neuronal βI and βIV isoforms, demonstrating how cells at different stages of differentiation can modulate microtubule dynamics through expression of different isoforms[24]. Importantly, the tubulins used in this experiment were unmodified, so the differences in observed microtubule dynamics can be directly attributed to differences in the proteins' primary sequences, rather than post-translational modifications that may otherwise be determined by the presence or absence of modifiable residues. Additionally, microtubules assembled from the βIIB and βIVb isoforms show an increase in protofilament number relative to whole-brain purified tubulin, indicative of an influence on the structural characteristics of the microtubule. Therefore, differential expression of tubulin isoforms is a mechanism by which a cell can modulate microtubule structure and dynamics.

Tubulin mutations often result in detrimental phenotypes, which reflects not only tubulin's essentiality, but also that different isoforms are often functionally distinct rather than redundant. For example, a homozygous knockout of Tuba1a in mice results in perinatal lethality despite the presence of 5 other α-tubulin genes in the mouse genome[25]. In *Plasmodium berghei*, a unicellular apicomplexan parasite with only two α-tubulin isoforms, the αII isoform cannot fully complement αI in the sporozoite stage of the life cycle by replacement at the native locus, even when the introns and UTRs are kept

intact[26]. The isoforms share 95% sequence identity, demonstrating that changes in a small number of key residues can be consequential for tubulin function. It remains to be seen whether the differing residues in *P. berghei* α-tubulins are directly responsible for changes in microtubule dynamics or structure, are subject to post-translational modifications, or modulate interactions with MAPs.

1.4 Purified Tubulin Reveals Intrinsic Differences Between Tubulin Isoforms and Whole-Cell Tubulin Populations Between Species and Cell Types

Historically, most *in vitro* experiments involving microtubule dynamics and protein-protein interactions have relied on tubulin purified from bovine and porcine brains, a tissue that contains a high abundance of tubulin. Tubulin is purified from brain tissue through a process of sequential polymerization, sedimentation, and depolymerization cycles, which yields purified protein that represents only a fraction of the original tubulin content of the tissue[27,28]. Many studies have used mammalian brain tubulin to elucidate basic principles of microtubule biology that are conserved among eukaryotes. However, bovine brain tubulin is for most applications a heterologous type of tubulin, and whether the composition of the yield may be biased towards isoforms or PTMs which confer microtubule stability cannot be ruled out if the yield does not contain the full tubulin complement of the cell.

The study of species-specific, cell-type-specific, and single-isoform tubulin have been made possible by recent advances in tubulin purification methods. The characterization of the TOG domains of XMAP/Dis microtubule polymerases, which bind soluble tubulin selectively and with high affinity, led to the development of an affinity chromatography-based approach using TOG fusion proteins to purify native tubulin from cultured cells, selected tissues, and whole organisms[29]. Tubulin purified this way represents the physiological mixture of isoforms and PTM status of tubulin in cells, which reveals intrinsic differences in tubulin biochemistry that result in differing microtubule dynamics between species. For example, tubulin purified from whole *Caenorhabditis elegans* worms polymerizes with a higher growth velocity and catastrophe frequency than bovine brain tubulin[30]. Cryo-EM analysis revealed differences in the interactions between protofilaments within the microtubule lattice resulting from differences in the structured core of the tubulin molecule. Therefore, differences in the tubulin primary

sequence have a direct influence on the tubulin-tubulin interactions that facilitate the microtubule polymer. Because *C. elegans* and humans are highly divergent species, the observed differences in microtubule dynamics are likely the result of multiple evolutionary changes in tubulin sequence and isoform composition. Studying tubulins of more closely related species may be informative for describing more specifically how intrinsic differences in microtubule dynamics have evolved to produce a given phenotype by narrowing down the number of possible mechanisms.

A number of structural and biochemical mechanisms have been proposed to explain the differences in microtubule dynamics seen using different purified tubulins. Microtubule plus-ends are stabilized by a cap of GTP-bound tubulin, which then hydrolyzes the GTP molecule and remains in the microtubule lattice in an unstable GDP-bound state. A study using a purified tubulin mutant that hydrolyzes GTP at a slower rate showed that decreasing the rate of hydrolysis was sufficient to increase the length of the GTP cap, which both increased microtubule lifetimes and growth rates relative to wild type[31]. Primary and secondary structure-based differences in lateral tubulin-tubulin contacts can also modulate the dynamicity of tubulin. The higher growth velocity and catastrophe frequency observed in *C. elegans* microtubules relative to those of bovine brain tubulin have been attributed to a lower activation energy, resulting in more order in the M and H1 loops of *C. elegans* tubulin. Another possible structural mechanism is evident in the study of purified α1b/βI+βIVb tubulin, in that these microtubules have a higher protofilament number, and thus less lateral curvature, than mosaic brain microtubules, which the authors interpret as having a lower energy cost for the conformation change upon GTP hydrolysis, leading to a higher growth velocity[24]. If confirmed, this mechanism may be distinct from the *C. elegans* mechanism, because the *C. elegans* microtubules had a lower (11), rather than a higher, number of protofilaments relative to bovine brain (13).

New methods in tubulin purification, in particular TOG-affinity purification, have thus enabled novel biochemical and biophysical experiments that have revealed mechanisms of modulating microtubule dynamics that were in many cases previously tested only indirectly. Tubulin dynamics and biochemistry show intrinsic variability, distinct from MAPs and motors, highlighting the importance of PTMs, isoform composition, and the structure of the tubulin molecule.

1.5 Aims and Scope of this Study

The relatively recent advent of a technique that allows for the purification of physiologically relevant tubulin from nearly any eukaryotic cell or tissue type, combined with well-established methods for characterizing microtubule dynamics and biochemical characteristics and interactions, has opened the door for interrogating how the tubulin molecule has evolved to confer intrinsic differences in microtubules between species. Imaging techniques such as total internal fluorescence microscopy (TIRF-M) enable high-resolution, quantitative measurement of intrinsic microtubule dynamics of microtubules assembled from purified tubulin *in vitro* (Figure 1.2).

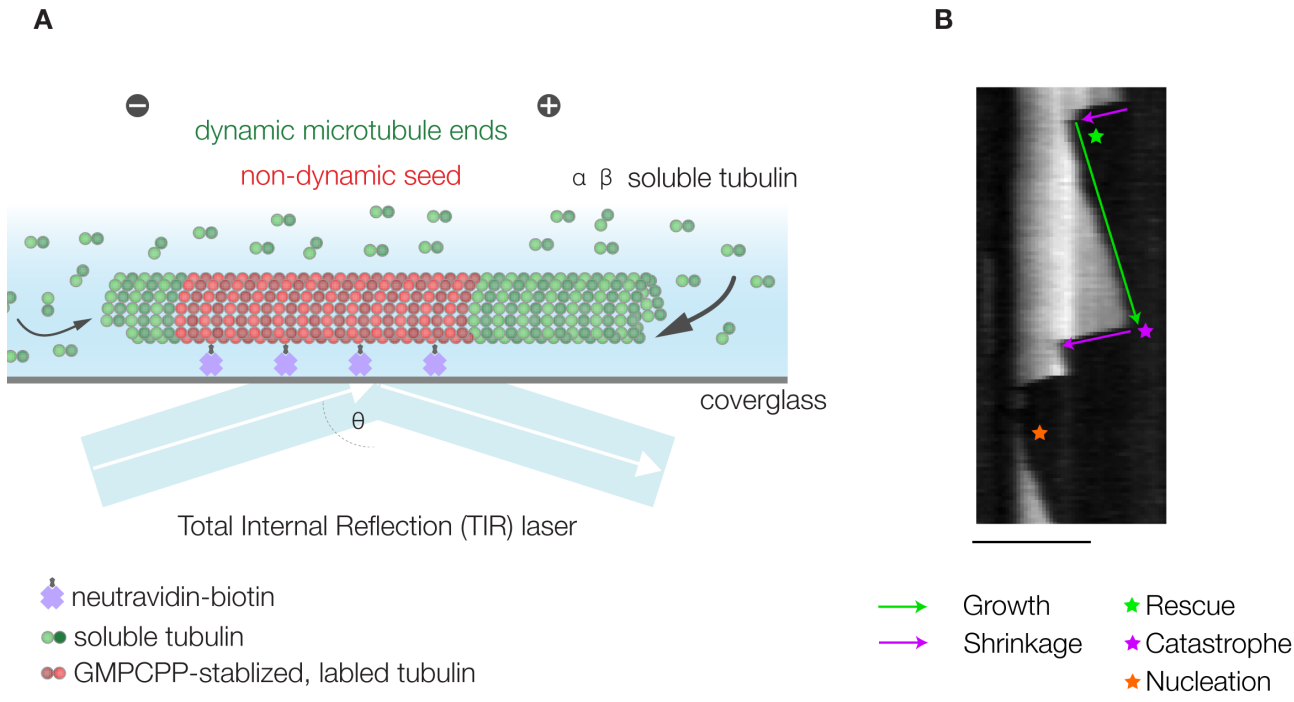

Figure 1.2 Visualization and quantification of dynamic microtubules by TIRF-M. (A) TIRF microscopy uses a collimated laser aimed at the sample at a low angle of incidence such that the difference in refractive indices of the objective oil and aqueous sample causes the laser to reflect back entirely. A resulting evanescent wave illuminates a region extending approximately 100 nm into the sample, thereby restricting the excitation and detection of fluorophores to a thin region. Stabilized, biotinylated microtubules are attached to a neutravidin-covered coverslip (red) and serve as nucleation templates for dynamic microtubules (green) in a solution containing the tubulin of interest and a small amount of labeled tubulin (See Materials and Methods 5.6 and 5.7). (B) A kymograph generated from a TIRF-M time-lapse image that is used to quantify microtubule dynamics. Exemplary growth, shrinkage, rescue, catastrophe, and nucleation events are annotated.

This study uses comparative approaches to explore how the biochemical diversity of tubulin manifests itself in two different physiological contexts: size control of the meiotic spindle of *Xenopus* frogs, and the differences in drug sensitivity between the microtubules of the malaria parasite *Plasmodium falciparum* and its human host. The central questions addressed in this work are:

1. Do the intrinsic dynamic properties of tubulin influence spindle length control?

The closely related frog species *X. laevis* and *X. tropicalis* differ in size at the whole-organism level, and this difference is mirrored at the cellular and subcellular level, with the larger *X. laevis* having a longer spindle than *X. tropicalis.* The size of the meiotic spindle in frogs is biochemically regulated. A few microtubule-associated proteins have been shown to contribute to, but not fully account for, the difference in spindle length between the two species. However, the contribution of tubulin itself has been unexplored. This study compares the intrinsic dynamic properties of *X. laevis* and *X. tropicalis* microtubules using TOG-affinity purified tubulin from egg extracts to assemble microtubules *in vitro* in absence of any proteins that influence microtubule dynamics. Measurements obtained using *in vitro* microtubule reconstitution assays are used to describe how differences in microtubule dynamics modulate the length and mass of microtubule populations. Additionally, possible influences of isoform composition and post-translational modifications on microtubule dynamics are explored, as well as the contribution of measured microtubule dynamics in setting spindle length.

2. Can tubulin serve as a parasite-specific drug target within a eukaryotic host?

Tubulin is an established drug target for treating maladies including parasite and fungal infections. However, tubulin is also a highly conserved protein, and the utility of antimitotic therapies is often limited by their toxicity to host cells. Microtubule inhibitors have gained interest over the past couple of decades for their activity against the malaria parasite *Plasmodium falciparum*, and several compounds are thought to selectively inhibit parasite over host microtubules. However, *in vitro* studies of drug-tubulin interactions have been limited by a lack of reliable methods for purifying functional

parasite tubulin. This study aims to apply TOG-affinity tubulin purification to produce functional *P. falciparum* tubulin and reconstitute microtubule dynamics *in vitro*, and to provide evidence for parasite-specific microtubule inhibition of several compounds in order to establish a robust *in vitro* framework for directly testing putative microtubule inhibitors on their parasite target. The biochemical composition and dynamic properties of *P. falciparum* tubulin will be characterized in comparison to mammalian tubulin, and the potential of various microtubule inhibitors to suppress *P. falciparum* growth.

Chapter 2. Differences in Intrinsic Tubulin Dynamic Properties Contribute to Spindle Length Control in Xenopus Species

2.1 Introduction

2.1.1 Spindle Length Control

Faithful chromosomal segregation requires precise control of the size and shape of the spindle during mitosis and meiosis, and aberrant spindle morphology can lead to aneuploidy and cell death. The spindle is a dynamic structure that emerges from the complex interactions between inherently dynamic microtubules and a wide variety of microtubule-associated proteins (MAPs) that modulate microtubule dynamics and parameters including microtubule nucleation, lifetime, mass, and transport within the spindle.

Unfertilized eggs, cytoplasmic egg extracts, and early embryos of Xenopus frogs, especially Xenopus laevis, have been used to identify many of the molecular players and biophysical principles responsible for controlling spindle size. The pole-to-pole length of the spindle in metaphase-arrested X. laevis eggs has an upper limit of around 40 microns, whereas the eggs themselves have a diameter of around 1.2 mm, a 30-fold difference[32]. Spindles can be reconstituted in cytostatic factor (CSF) egg extracts in vitro and still reach an upper length limit, even in the absence of a bounding membrane[32]. Biochemical perturbations of spindles assembled in CSF extract have demonstrated the connection between microtubule dynamics and spindle length control, culminating in a mass balance model that relates spindle length to parameters including microtubule growth velocity, nucleation, and mass[8]. For example, steady-state spindle length in extracts can be modulated through titration of XMAP215, a spindle protein native to Xenopus eggs that had previously been shown to increase the growth velocity of microtubules assembled from purified tubulin[33]. Extracts with excess XMAP215 form longer spindles, whereas extracts depleted of XMAP215 form shorter spindles. However, the full picture of how spindle size and shape are determined and maintained is still incomplete.

Comparative studies of egg extracts from *X. laevis* and the closely related species *Xenopus tropicalis* have revealed additional mechanisms that play a role in spindle length control by identifying microtubule regulators that are differentially regulated between the two systems. While spindles of both species maintain an upper length limit in CSF-

extracts, *X. tropicalis* spindles reach a length approximately 30% shorter than those of *X. laevis*[34]. Mixing extracts has been shown to produce spindles of intermediate length, indicating one or more soluble titratable factors are responsible for the length difference. One mechanism that has been proposed as limiting spindle length is tubulin acting as a limiting component, where at small enough cytoplasmic volumes relative to the spindle, the pool of soluble tubulin decreases with cytoplasmic volume to the point where spindle length also decreases due to the decrease in available material[35]. However, this mechanism can be ruled out in the case of CSF-extract spindles, because *X. laevis* and *X. tropicalis* extracts have the same tubulin concentration, and the cytoplasm is much larger relative to spindle size than the volume at which the cell size-dependent scaling regime begins during development[32,36]. Subsequent studies have identified differentially regulated *Xenopus* spindle length control proteins such as katanin, a microtubule severing protein that shows higher activity in *X. tropicalis* spindles that leads to increased MT depolymerization, and thus a shorter spindle, in *X. tropicalis* relative to *X. laevis*[37]. However, differences in severing-dependent MT depolymerization do not fully account for the observed difference in spindle length, which suggests additional mechanisms are involved.

2.1.2 Intrinsic Differences in Tubulin Dynamics

Tubulin is the main building block of the spindle, but the lack of physiologically relevant tubulin species has so far prevented the study of how the intrinsic dynamic properties of tubulin contribute to spindle size control. Although tubulin is highly conserved, whole-cell and whole-organism purifications of native tubulin from species such as *Arabidopsis thalania* and *C. elegans* have demonstrated species-dependent variation in microtubule dynamics that deviate greatly from well-characterized mammalian brain microtubule dynamics, which suggests a functional relevance of intrinsic dynamic characteristics distinct from interactions with MAPs and motors[38,39]. Measurements of microtubules assembled in X. laevis and X. tropicalis CSF-extracts have previously shown that X. laevis microtubules grow roughly 25% faster than X. tropicalis, which is consistent with experiments showing higher growth velocities resulting in longer spindles[8,34]. However, because the microtubules were visualized in extract rather than in a system using purified components, the difference could be the result of one or many unknown mechanisms.

Given the many ways that microtubule dynamics can be influenced through isoform composition, PTMs, and the core structure of the tubulin molecule, is it possible that biochemical differences between *X. laevis* and *X. tropicalis* tubulin have a direct impact on microtubule dynamics that contribute to the observed difference in spindle size? To address this question, native tubulin was purified from CSF egg extracts of *X. laevis* and *X. tropicalis*, and differences in isoform composition, posttranslational modifications, and dynamics of microtubules assembled from purified tubulin *in vitro* were characterized. Time-lapse imaging of fluorescently labeled microtubules assembled from purified tubulin using total internal reflection fluorescence microscopy (TIRF-M) was used to measure the four parameters of dynamic instability: growth velocity (v_g), depolymerization velocity (v_d), catastrophe frequency (f_{cat}), and rescue frequency (f_{res}). *Xenopus* microtubules were compared to microtubles assembled from *Bos taurus* neuronal tubulin, as mammalian brain tubulin has been the standard for in vitro microtubule studies for the past few decades.

2.2 Results

2.2.1 *Xenopus laevis* egg extract microtubules polymerize faster than *X. tropicalis*.

Control of microtubule growth rate is an established mechanism for controlling spindle length[8,40,41]. Although previous experiments have shown a higher growth rate of microtubules nucleated from centrosomes in *X. laevis* CSF-extract relative to *X. tropicalis,* a direct role for the modulation of microtubule growth rate in determining the difference in spindle length between the two species has yet to be established. To measure the difference in microtubule dynamics in CSF-extracts between the two species, microtubules were assembled in extract and visualized by TIRF microscopy in a modified version of the microtubule dynamics measurements performed in (34) (Figure 2.1). Instead of using centrosomes, microtubules were nucleated from GMP-CPP stabilized microtubule seeds, and vanadate was added to inhibit katanin-induced microtubule severing. In *X. laevis* extracts, microtubules grow about 20% faster (21.83 ± 2.76 µm/min) than in *X. tropicalis* extracts (17.61 ± 3.25 µm/min), which is comparable to the difference shown in (Brown 2007) (18.5 ± 8.8 µm/min for *X. laevis* and 14.7 ± 4.4 µm/min for *X. tropicalis*).

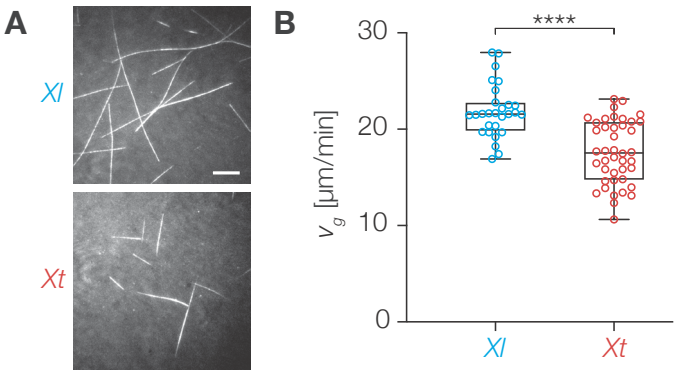

Figure 2.1 Measurement of microtubule growth rates in *Xl* and *Xt* egg extracts. Representative TIRF images of microtubules nucleated from GMPCPP-stabilized microtubule seeds grown in *Xl* or *Xt* extracts. Scale bar represents 10 µm. *Xl* and *Xt* microtubules grew at 21.8 ± 2.8 µm/min and 17.6 ± 3.2 µm/min, respectively, with $p < 0.0001$ (Mann-Whitney). Values were obtained from measurements pooled over at least two independent experiments.

2.2.2 The TOG Column Yields Active Tubulin Free of Contamination

In order to determine whether differences in microtubule dynamics observed in a physiological context are intrinsic to tubulin itself, tubulin was first purified from CSF-extracts by affinity chromatography according to (29) (See Materials and Methods). Importantly, this purification method completely depleted the extract input of tubulin, thus the purified protein is representative of the full tubulin pool available to the cell during spindle assembly (Figure 2.2A). Special attention was paid to sample purity in order to rule out the potential influence of contaminating MAPs in subsequent experiments. Western blot analysis did not detect XMAP215 or katanin in either sample, even when the purified tubulin was loaded in excess relative to its concentration in CSF-extract, in which the two MAPs are readily detectable (Figure 2.2B). Additionally, purified tubulin was subjected to in-solution digest and mass spectrometry analysis, which confirmed that the tubulin was of high purity. Only minor contamination from otherwise highly abundant proteins such as heat-shock proteins (HSPs) and ribosomal protein was found.

The assembly competence of the different tubulins was also qualitatively assessed in order to confirm that the different purifications yielded samples with the same proportion of active tubulin. Microtubule assembly reactions at steady state exist as an equilibrium between polymerized and soluble tubulin, and meaningful interpretations of microtubule dynamics are not possible if a significant amount of the soluble tubulin pool cannot form microtubules. Microtubule stabilizing agents such as Taxol or glycerol push the equilibrium towards the polymerized state, ensuring that any tubulin that can form microtubules will do so. To determine the assembly-competent fraction of purified tubulin, microtubules were assembled in the presence of glycerol and centrifuged over a high-density glycerol cushion (Figure 2.2C). For both *X. laevis* and *X. tropicalis* polymerization reactions, the majority of tubulin was found in the pellet and in the same proportion relative to the supernatant. Commercially available bovine tubulin also demonstrated similar assembly competence. Therefore, any differences observed in microtubule dynamics among the tubulins can be attributed to intrinsic differences in tubulin assembly properties and not differences in the quality of protein preparation.

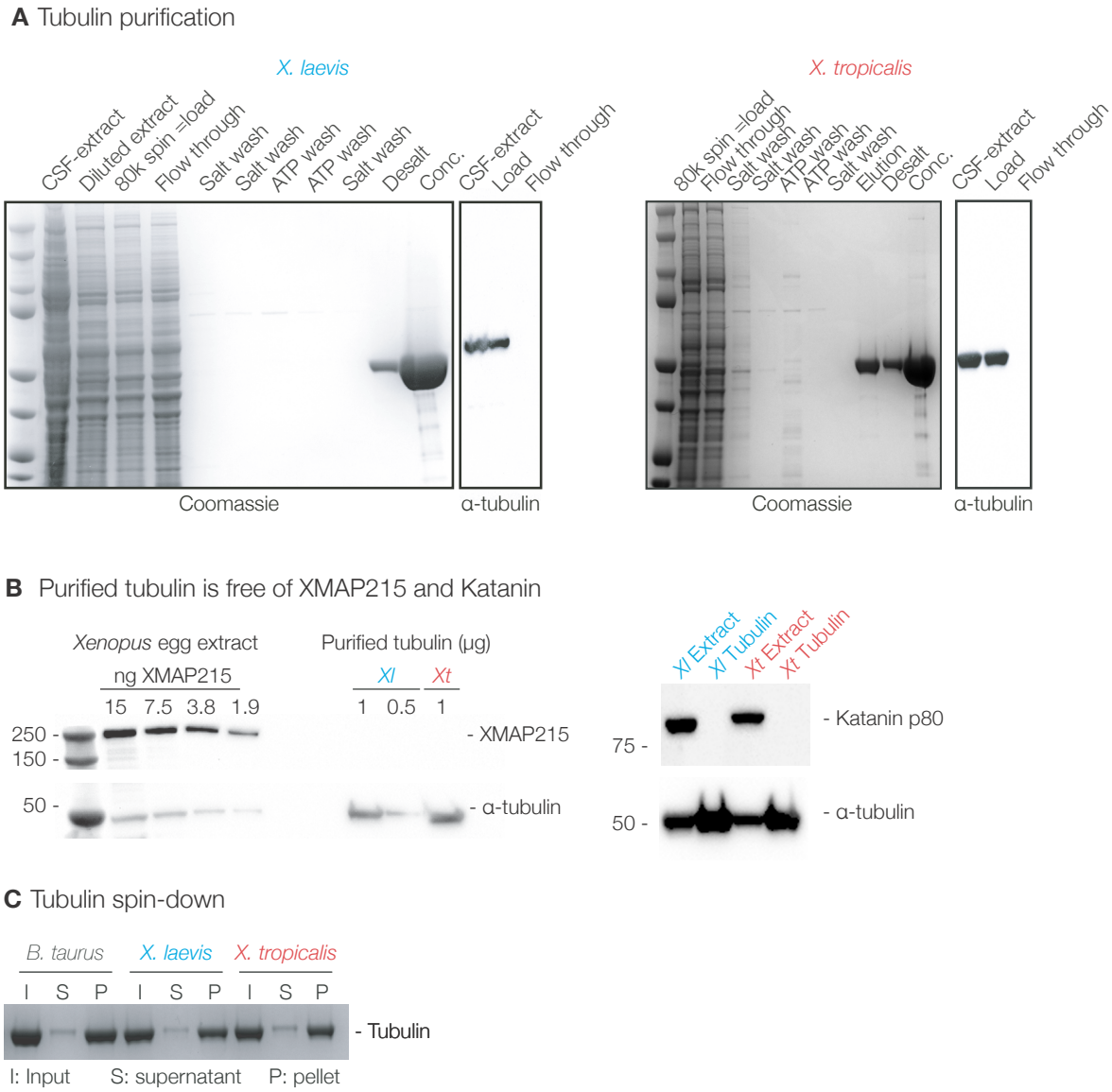

Figure 2.2 Egg extract tubulin and assessment of tubulin activity and purity. (A) Tubulin was purified from *X. laevis* and *X. tropicalis* egg extracts according to (29) and (34). Samples collected throughout each purification were analyzed by SDS–PAGE and stained with Coomassie blue. The CSF-extract, the extract after the 80k spin (load), and the TOG column flow through were transferred to nitrocellulose and probed with DM1 α-tubulin antibody to show that tubulin was depleted from the extract. (B) To test for contamination with the microtubule polymerase XMAP215, 0.5 – 1 µg of purified *Xenopus* tubulin was loaded onto an SDS-PAGE gel, transferred to a nitrocellulose membrane, and probed with an anti-XMAP215 antibody. Volumes of *X. laevis* CSF-extract containing 1.9 – 15 ng XMAP215[8] were loaded in parallel to demonstrate the sensitivity of the assay. *Xenopus* CSF-extracts and purified tubulins were additionally probed with an antibody against the p80 subunit of katanin. (C) To test the assembly competence of each purified tubulin, microtubules were assembled at 20 µM at 37°C in 33% glycerol and centrifuged over a 60% glycerol cushion. Input (I), supernatant (S) and pellet (P) fractions were analyzed by Coomassie. Adapted from Figure S1 of Hirst et. al 2020.

2.2.3 *Xenopus laevis* Microtubules Combine Fast Growth and Infrequent Catastrophes *in vitro*

To measure microtubule dynamics, microtubules were grown from GMP-CPP-stabilized microtubule seeds in vitro and visualized by TIRF-M according to (42) (Figure 2.3). In addition to the two *Xenopus* tubulins, commercially available bovine brain tubulin was tested to serve as a reference. Initially, a range of tubulin concentrations ranging from 1.5 µM to 12 µM was tested in order to determine a suitable concentration at which to compare the three species, which revealed stark differences in microtubule assembly characteristics. Surprisingly, *X. laevis* microtubules nucleated from GMPCPP templates at tubulin concentrations as low as 1.5 µM. In contrast, robust nucleation from templates was observed only at 6 µM tubulin *for X. tropicalis* microtubules. The nucleation threshold for both frog species was below that of Bos taurus tubulin at around 9 µM. At higher concentrations (12 µM and above), *X. laevis* microtubules began to spontaneously nucleate and crowd the field of view, making quantification difficult. Microtubules from all three species were able to robustly nucleate from seeds at 9 µM and these reactions were mostly free of spontaneously nucleated microtubules, so this concentration was chosen for subsequent analysis.

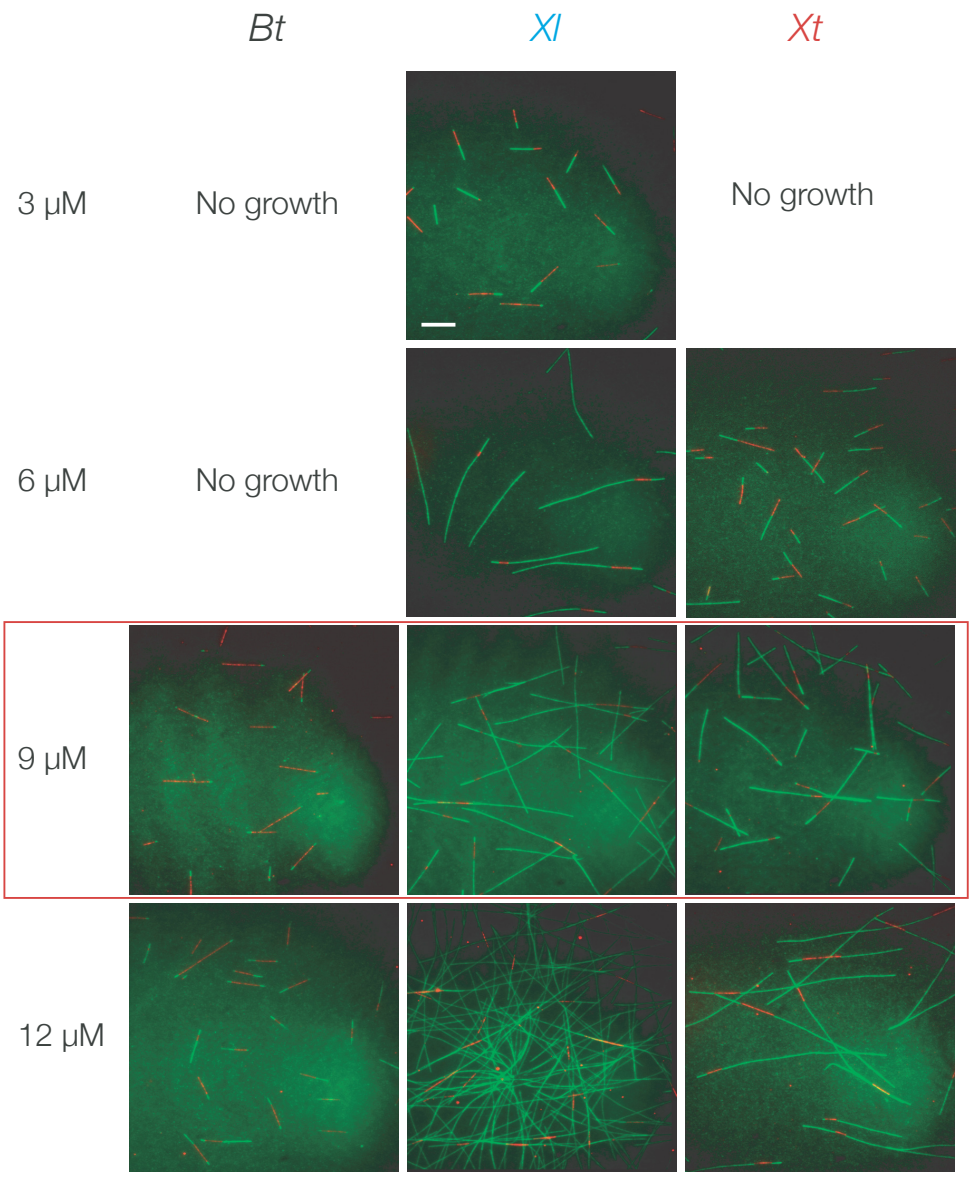

Figure 2.3 Representative TIRF images showing dynamic *B. taurus*, *X. laevis*, and *X. tropicalis* microtubules at 3, 6, 9 and 12 µM tubulin. Dynamic tubulin labeled with Cy3 is shown in green and stabilized Cy5-labeled GMPCPP-seeds are shown in red. "No growth" indicates concentrations at which no dynamic microtubules were observed over a 30-min period. Scale bar: 10 µm. Adapted from Figure S3 of Hirst et al 2020.

Kymographs showing microtubule growth over time were generated from time-lapse images and used to quantify the parameters of dynamic instability: growth velocity, catastrophe frequency, depolymerization velocity, and rescue frequency (Figures 2.4 and 2.5). *X. laevis* microtubules grew nearly twice as fast as *X. tropicalis* (1.92 ± 0.02 µm/min versus 0.96 ± 0.02 µm/min) and had a lower catastrophe frequency (<0.00015 s^{-1} versus 0.0044 ± 0.00076 s^{-1}). While catastrophes were rare for *X. laevis* microtubules, when

they did occur, *X. laevis* microtubules also rescued with a higher frequency than *X. tropicalis* (0.11 ± 0.031 s^{-1} versus 0.013 ± 0.0026 s^{-1}). In comparison to *Xenopus* microtubules, *B. taurus* microtubules grew slowly and had a higher catastrophe frequency. Most depolymerization events did not end in a rescue for *B. taurus* or *X. tropicalis*.

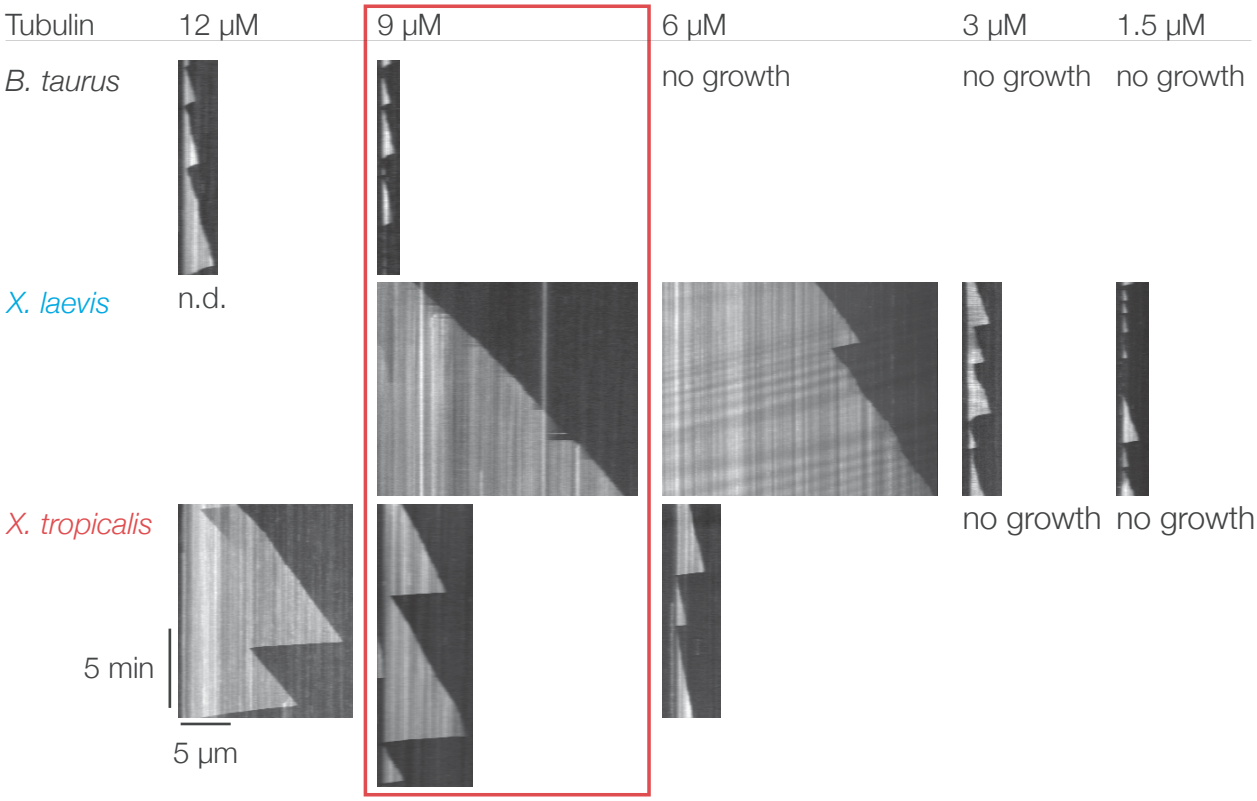

Figure 2.4 Representative TIRF kymographs showing dynamic *B. taurus*, *X. laevis* and *X. tropicalis* microtubules at 12, 9, 6, 3 and 1.5 µM tubulin. *B. taurus* tubulin does not show any growth at 1.5, 3 and 6 µM tubulin, *X. tropicalis* tubulin does not show any growth at 1.5 and 3 µM tubulin. *X. laevis tubulin* grown at 12 µM was very difficult to analyze as the microtubules grew too long and overlapped. Adapted from Figure S1 of Hirst et. al 2020.

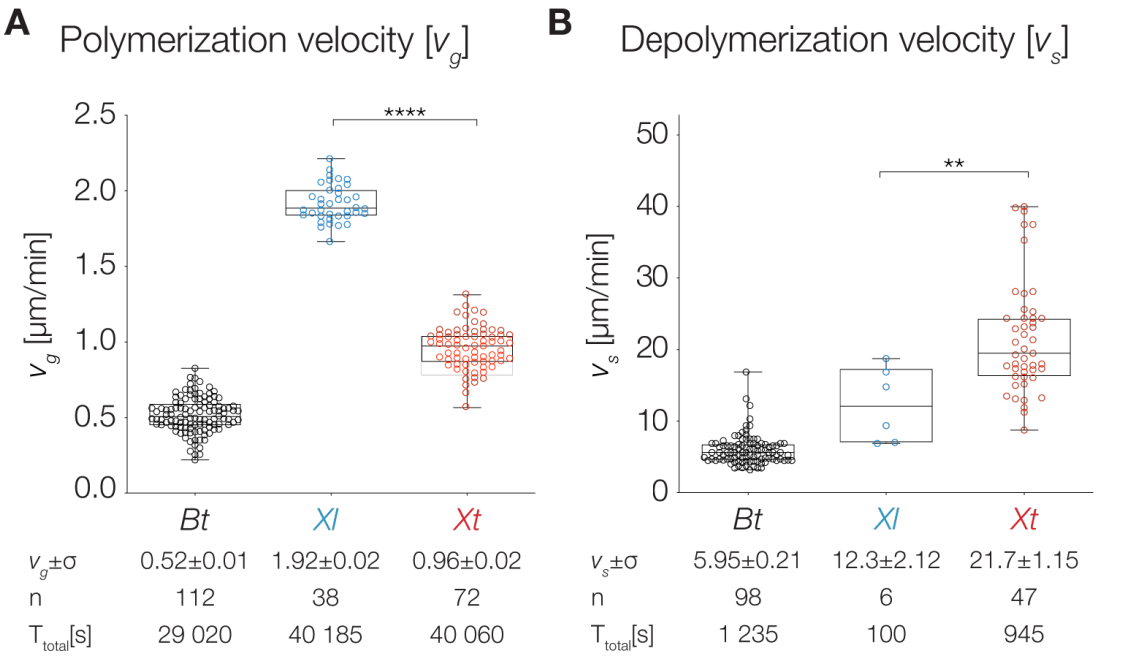

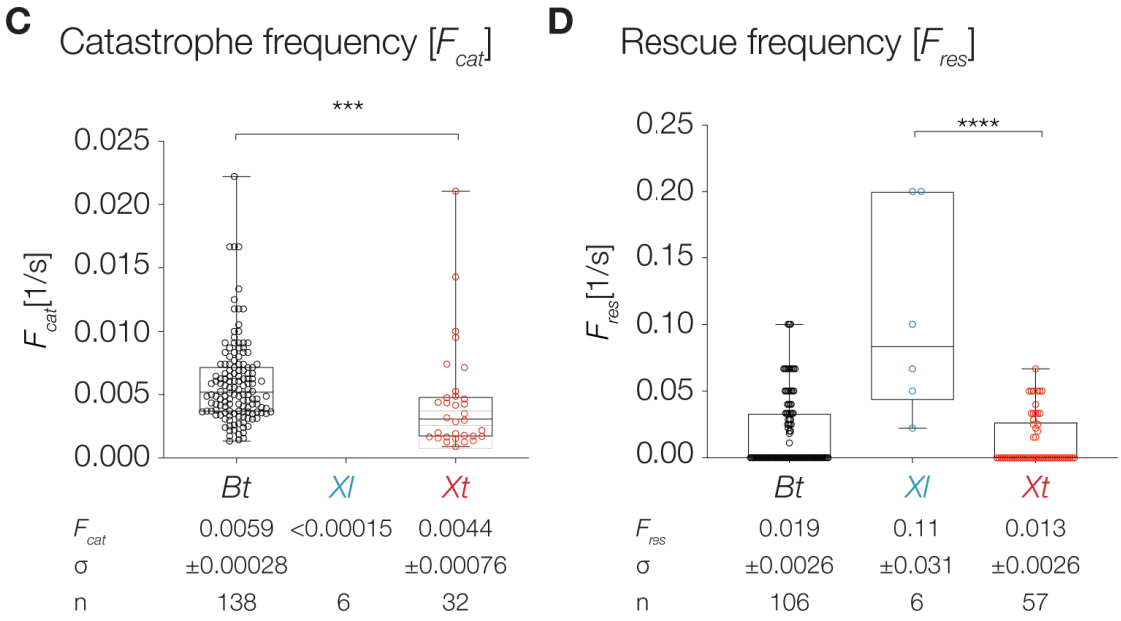

Figure 2.5 Parameters of dynamic instability. All values were obtained from measurements of microtubules pooled over at least 3 independent experiments, and all p values are calculated with the Mann-Whitney test. (A) *Bt* microtubules grow at 0.52 ± 0.01 µm/min (14.0 ± 0.3 dimers/s), *Xl* microtubules at 1.92 ± 0.02 µm/min (51.9 ± 0.5 dimers/s), and Xt microtubules at 0.96 ± 0.02 µm/min (25.9 ± 0.5 dimers/s) with $p_{(Xl, Xt)} < 0.0001$. (B) *Bt* microtubules depolymerize at 5.95 ± 0.21 µm/min (161 ± 5.67 dimers/s), *Xl* microtubules at 12.3 ± 2.12 µm/min (332 ± 57.3 dimers/s), and *Xt* microtubules at 21.7 ± 1.15 µm/min (587 ± 31.2 dimers/s) with $p_{(Xl, Xt)} = 0.0039$. (C) Catastrophe frequencies are reported as the inverse of microtubule lifetimes. *Xl* microtubules catastrophe very rarely (<0.00015 s^{-1}) although *Xt* microtubules catastrophe at 0.0044 ± 0.00076 s^{-1} with $p_{(Bt, Xt)} = 0.0002$. (D) Rescue frequencies are reported as the inverse of the duration of each depolymerization event. Events without a rescue are given a value of zero. *Xl* microtubules rescue at 0.11 ± 0.031 s^{-1} and *Xt* microtubules at 0.013 ± 0.0026 s^{-1}, with p(Xl, Xt) <0.0001. Total time (T_{total}) of observed microtubule growth and

shrinkage, SEM (s), and number of events (n) are indicated. For the modified box-and-whiskers plots, the boxes range from 25th to 75th percentile, the whiskers span the range, and the horizontal line marks the median value. Adapted from Figure 1 of Hirst et al. 2020.

2.2.4 *Xenopus laevis* and *tropicalis* Tubulin Populations Differ in Their Phosphorylation Pattern

The three tubulins were tested for reactivity with a series of antibodies against known tubulin PTMs by western blot (Figure 2.6A). When comparing antibody reactivity between egg extract and purified tubulin, *X. laevis* and *X. tropicalis* PTM patterns were preserved, indicating the PTMs or lack thereof of purified tubulin were representative of the tubulin PTMs in egg extract (Figure 2.6B). Relative to *B. taurus* tubulin, which was recognized by all five antibodies, both *Xenopus* tubulins were unmodified with the exception of *X. laevis* tubulin, which was recognized by a pan-specific antibody against phosphorylated serine residues (Figure 2.6A and C).

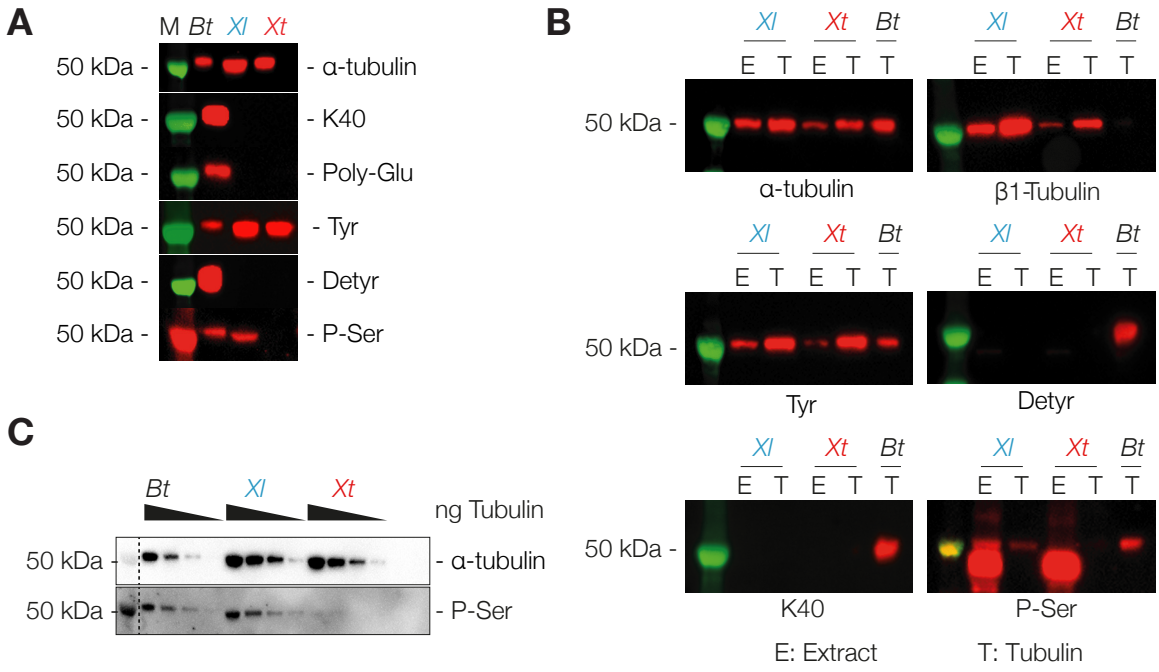

Figure 2.6 PTM analysis of purified tubulin and CSF-extracts by western blot. (**A**) Western blots probing post-translational modifications found in purified *Bt*, *Xl*, and *Xt* tubulin. a-tubulin is a loading control, K40 recognizes acetylated lysine at position 40 of α-tubulin, Poly-Glu recognizes epitopes containing acidic residues modified with a chain of at least 2 glutamyl residues, Tyr recognizes the C-terminal EEY epitope of tyrosinated tubulin, Detyr recognizes the detyrosinated C terminus of a-tubulin, and P-Ser is pan-specific for

phosphorylated serine residues. (**B**) Freshly prepared CSF-extracts (E) and purified tubulin (T) were analyzed by Western blot. (**C**) Adapted from Figures 2 and S2 of Hirst et al 2020.

2.2.5 Tubulin is refractory to dephosphorylation

In order to test whether the difference in phosphorylation between *X. laevis* and *X. tropicalis* tubulin is a result of phosphorylation, several attempts were made to dephosphorylate *X. laevis* tubulin using three different phosphatases (Figure 2.7). Previously published attempts to dephosphorylate the βIII tubulin isoform using lambda phosphatase and PP2A have shown that the isoform is resistant to dephosphorylation[43]. Consistent with these results, incubation of tubulin with PP2A, lambda phosphatase, and alkaline phosphatase did not reduce the reactivity with the phosphoserine antibody as measured by western blot.

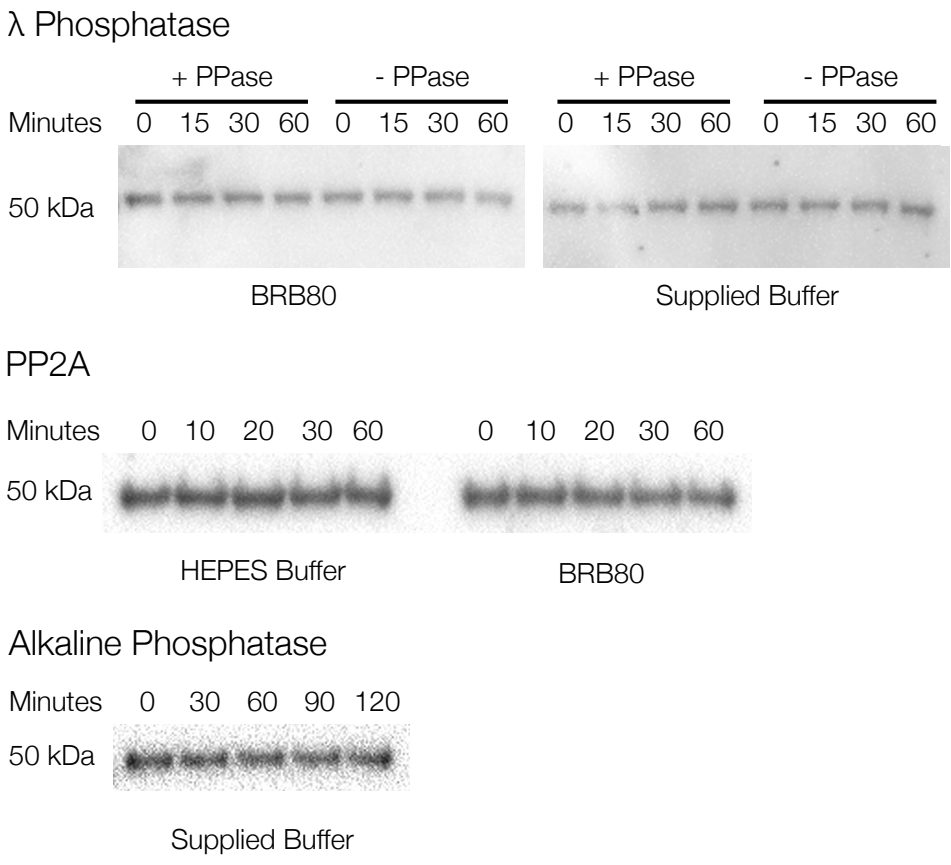

Figure 2.7 Phosphatase reactions with *Xl* tubulin. Dephosphorylation of Xl tubulin was attempted with 3 different phosphatases: bacteriophage lambda phosphatase, alkaline phosphatase, and human PP2A-α/PP2AR. Aliquots of the reaction mixtures taken at different time points were analyzed by Western blot with the P-Ser antibody. Adapted from figure S2 of Hirst et al 2020.

2.2.6 *Xenopus laevis* extract does not phosphorylate stabilized *X. tropicalis* microtubules

To test whether phosphorylation activity in *X. laevis* egg extract could phosphorylate *X. tropicalis* tubulin, taxol-stabilized *X. tropicalis* microtubules were incubated in nocodazole-treated *X. laevis* egg extract and tested for phosphorylation by western blot (Figure 2.8). Taxol and nocodazole were used, respectively, to keep *Xt* tubulin in a polymerized state and *Xl* tubulin soluble, thus keeping the two tubulin populations separate. After incubating for one hour at 20°, the reaction was centrifuged over a 60% v/v glycerol cushion. The pellet, which consisted of stabilized *Xt* microtubules, was washed and analyzed by western blot. The recovered pellet showed a positive α-tubulin signal which was absent in the negative control without *Xt* microtubules, indicating stabilized *Xt* microtubules remained polymerized during the incubation and that endogenous extract tubulin did not polymerize. However, the phosphoserine antibody did not react with the recovered pellet sample, suggesting that either *Xl* CSF-extract does not phosphorylate polymerized *Xt* microtubules, or the phosphosite is absent in *Xt* tubulin.

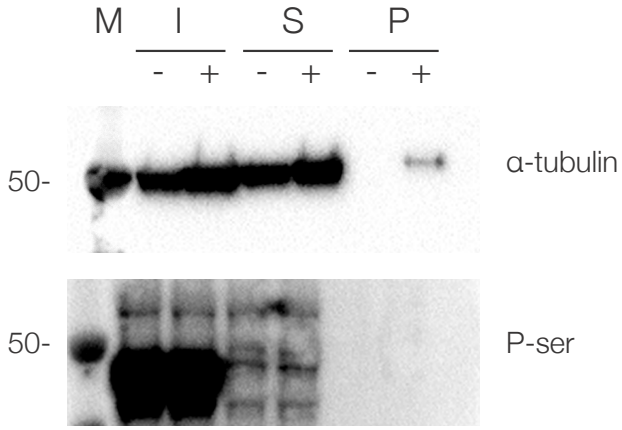

Figure 2.8 *Xl* CSF-extract does not phosphorylate stabilized *Xt* microtubules. M – molecular weight marker; I – extract input; S – extract supernatant after centrifugation; P – washed pellet. Addition or absence of *Xt* microtubules (+/-) is indicated.

2.2.7 *Xenopus laevis* and *tropicalis* Tubulin Populations Differ in Their Mass Spectra

In order to determine the isoform composition of purified *Xl* and *Xt* tubulin, intact tubulin samples were analyzed by mass spectrometry (Figure 2.9 A and B). Of the several α- and β-tubulin isoforms encoded in the *Xl* and *Xt* genomes, four α-tubulin peaks and

one β-tubulin peak could be matched to masses predicted from sequences obtained from uniprot.org (Figure 2.9C). The major α-tubulin peaks corresponded to isoforms annotated as A1C and AL3 on xenbase.org. While the spectra appear qualitatively similar, the intensities of the highest two peaks appear in different ratios between the *Xl* (peak 2 vs 4, both annotated as AL3) and the *Xt* (peak 2 vs 3, annotated as A1C and AL3) spectra. Absolute isoform concentrations cannot be determined from the spectra, but the differences in relative peak intensities may be a consequence of different ratios of the major isoforms expressed by both frogs. It remains to be determined whether the isoforms identified by mass spectrometry individually can modulate *Xenopus* microtubule dynamics.

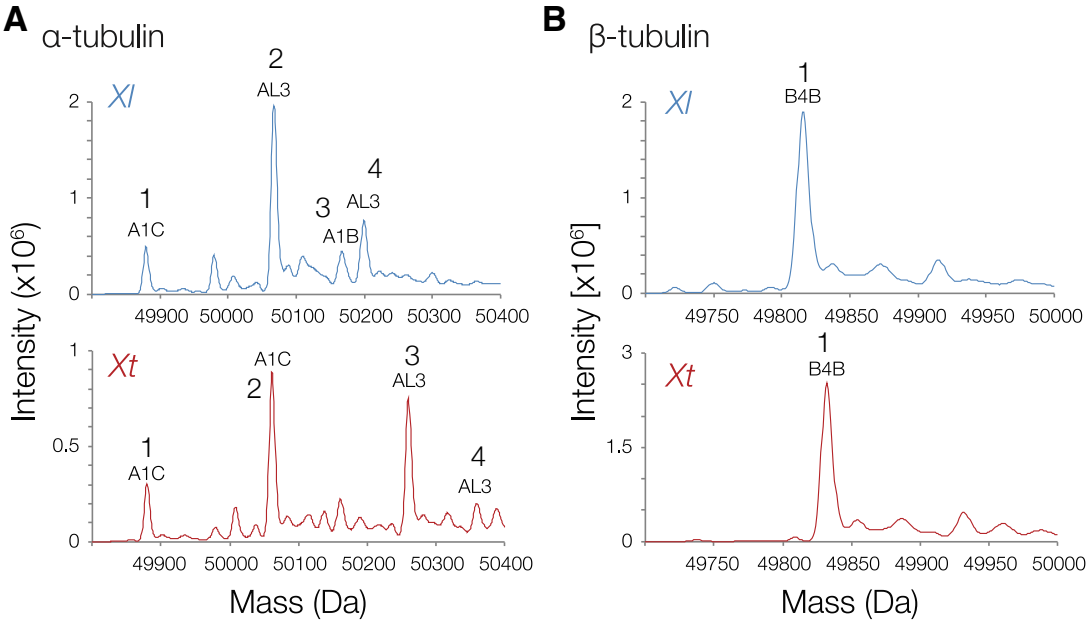

C

		Peak	Mass (Da)	Isoform	Predicted Mass (Da)	BLAST *Mm*	BLAST *Bt*	BLAST *Xl*	BLAST *Xt*	Identity
α-tubulin	Xl	1	49 879	P08537	49 879.33	A1C	A1C	A1Cl	A1C	99%
	Xt	1	49 879	Q6P8G7	49 879.33	A1C	A1C	A1Cs	A1C	
	Xl	2	50 067	Q5U4V6	50 067.46	A1C	A1C	AL3	AL3	94%
	Xt	2	50 061	Q5EB23	50 061.39	A1C	A1C	A3	AL3	
	Xl	3	50167	A0A1L8HHQ5	50167.63	A1B	A1B	A1	A1	90%
	Xt	3	50260	Q6NVN1	50259.74	A1C	A1C	AL3s	AL3	
	Xl	4	50199	Q6NRV3	50199.72	A1C	A1C	AL3s	AL3	97%
	Xt	4	50359	F6Z511	50 358.87	A1C	A1C	AL3s	AL3	
β-tubulin	Xl	1	49 815	P30883	49 815.95	B4B	B4B	B4	B4B	99%
	Xt	1	49 832	Q0IIR4	49 831.95	B4B	B4B	B4	B4B	

Figure 2.9 Intact protein mass spectra and annotation of purified *Xl* and *Xt* tubulin. (A) α-tubulin and (B) β-tubulin mass spectra of *Xl* (blue) and *Xt* (red) tubulin. (C) For each peak (1 – 4), the uniprot.org ("Isoform") and xenbase.org (*Xl, Xt*) identifiers of the isoform are annotated, its predicted mass is calculated and BLAST search results against Mus musculus (*Mm*), Bos taurus (*Bs*), X. laevis (*Xl*) and X. tropicalis (*Xt*) are shown.

2.2.8 *Xenopus tropicalis* and bovine MTs reach steady state at lower MT mass than *X. laevis*

The length distribution and total mass of a population of dynamic microtubules at steady state are determined by the parameters of dynamic instability[8]. For a given nucleation event, the mass m of a microtubule can be calculated as

$$m = v_p \tau \mu$$

where v_p is the microtubule growth velocity, τ is the microtubule lifetime, and μ is the molecular weight per unit length of a microtubule. Therefore, the mass and average length of a population of microtubules increase with growth velocity and average microtubule lifetime (often calculated as the inverse of catastrophe frequency [Gardner]). When a microtubule population is in steady state, the mass of tubulin polymerizing into microtubules is equal to the mass of tubulin returning to the soluble tubulin pool by depolymerization, therefore the total microtubule mass does not significantly change over time.

The timepoint at which microtubule polymerization reactions with 9 μM tubulin reached steady state was determined by measuring microtubule mass per seed at 5-minute intervals over 30 minutes (Figure 2.10). Reactions were considered to have reached steady state when the average mass per seed no longer changed significantly over time according to the Mann-Whitney test. For *B. taurus* and *X. tropicalis* microtubules, steady state conditions were met after 10 and 15 minutes, respectively. The average mass per seed of *X. laevis* microtubules continued to increase after 30 minutes of imaging, at which point microtubules became too long and quantification was limited by the field of view.

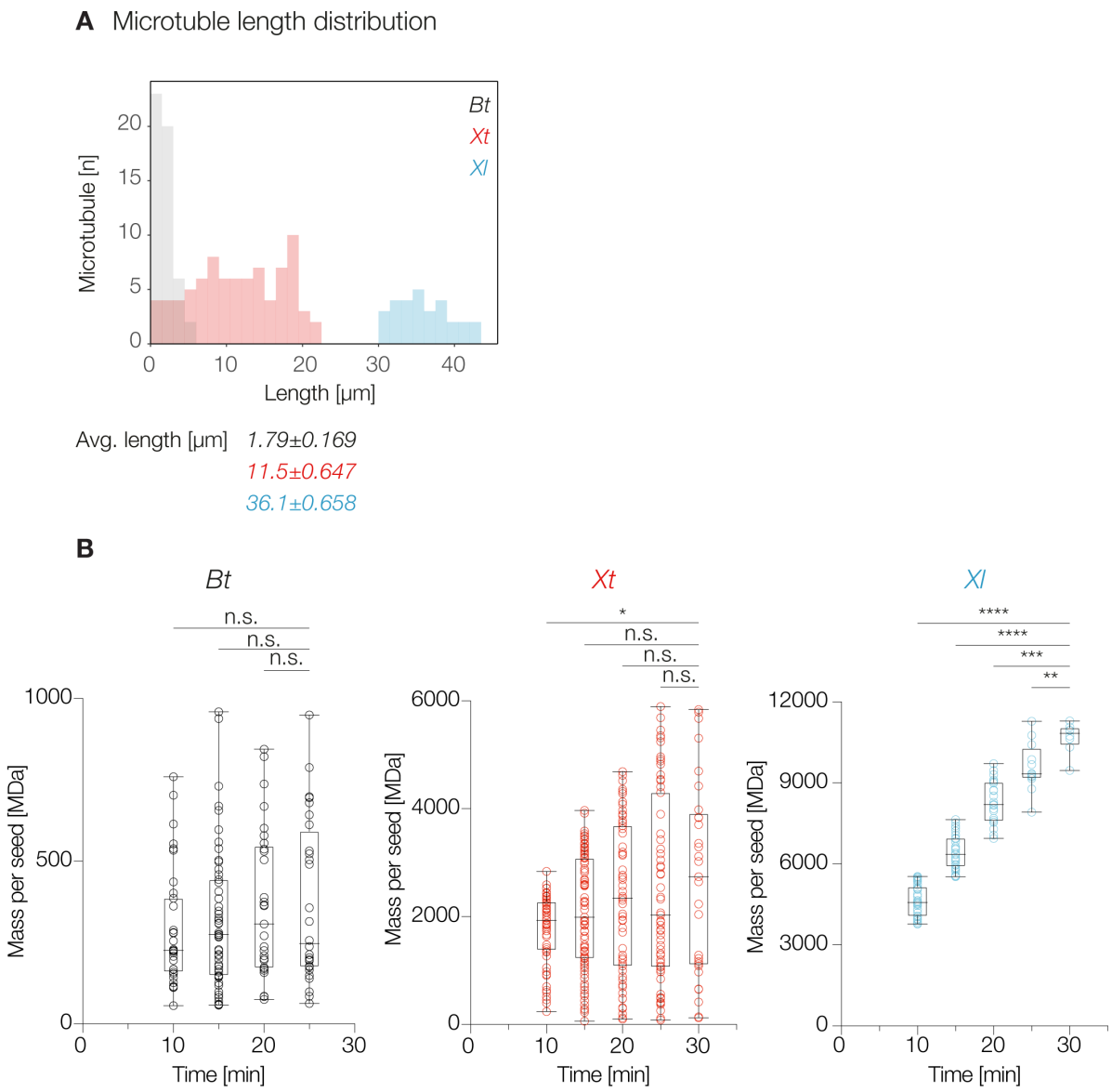

Figure 2.10 Microtubule polymer mass and length distribution. (B) Length histograms of *B. taurus*, *X. laevis* and *X. tropicalis* microtubules grown at 9 µM tubulin after 15 min. The number of microtubules measured in each sample were 51 (*Bt*), 29 (*Xl*), and 83 (*Xt*), with mean lengths of 1.78 ± 0.17, 36.1 ± 0.66, and 11.5 ± 0.65 µm, respectively. Only microtubules grown from the microtubule plus end were measured. (C) Microtubule masses per seed were measured at 5-min intervals for up to 30 min after initiation of the polymerization reaction at 9 µM. Values for each time point were pooled over at least 2 replicate experiments. Mean microtubule masses were calculated and compared to the mean at the final time point using the Mann-Whitney test. Adapted from Figure S3 of Hirst et al 2020.

2.2.9 *Xenopus laevis* microtubules polymerize at low tubulin concentrations

The critical concentration of tubulin is the concentration below which microtubules will not polymerize. Microtubule growth velocity increases linearly with increasing tubulin concentration, and the critical concentration can be estimated as the x-intercept of the line of best fit on a plot of growth velocity against tubulin concentration[44]. To determine the critical concentrations of *Xl, Xt,* and *Bt* tubulin, microtubule growth rates of at least three different tubulin concentrations at 37°, plotted as a function of concentration, and x-intercepts were extrapolated from weighted lines of best fit (Figure 2.11). By this method, the critical concentration for *Bt* tubulin was determined to be 3.4 μM, which is within 3 μM of the previously published value of ~1 μM[44]. *Xt* tubulin had a slightly lower critical concentration of 2.9 μM, whereas the x-intercept for the line of best fit of the *Xl* data gave a negative value of -2.9. While this value cannot correspond to a real concentration and can be attributed to the error of the fit, seed-templated *Xl* microtubule polymerization was observed at 1.5 μM, so it can be concluded that the critical concentration for *Xl* tubulin is between 0 and 1.5 μM and is thus lower than the critical concentration of either *Xl* or *Bt* tubulin.

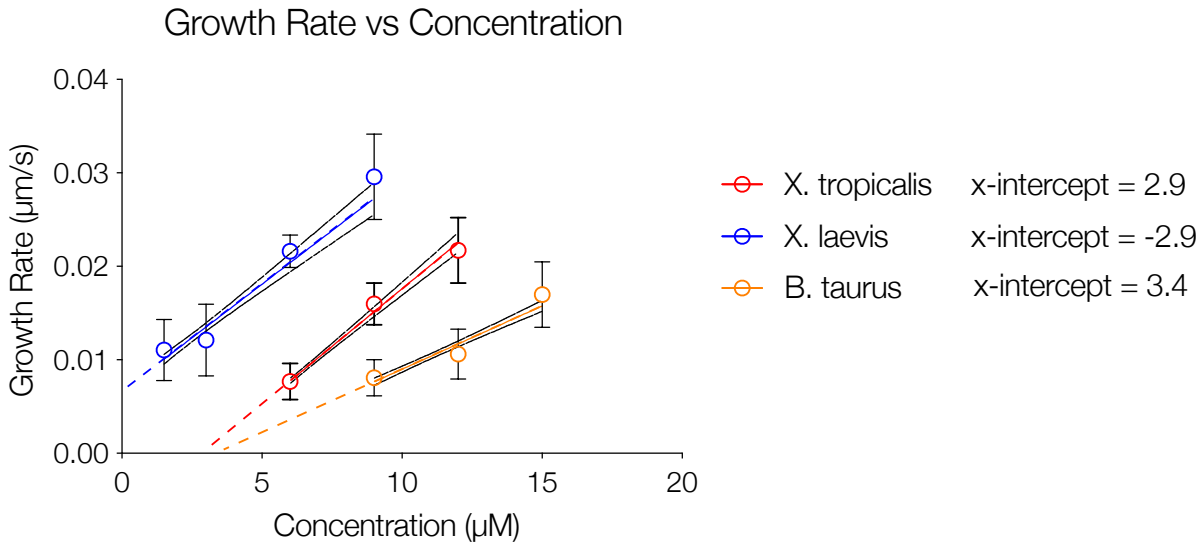

Figure 2.11 Microtubule growth rates at 37° plotted as a function of tubulin concentration. All values were obtained from measurements of microtubules pooled over at least three experiments. X-intercept values were obtained by extrapolation of a weighted linear fit. Error bars indicate SD.

2.2.10 Microtubule Length Can Be Modulated by Titrating Tubulin Sources

Mixing tubulins that differ in activity has been shown to produce microtubules with intermediate dynamic properties[30]. Specifically, if the final tubulin concentration is held constant, the microtubule growth velocity will increase linearly as the relative proportion of the more active tubulin is increased. Growth velocity was measured at 6 μM tubulin in reactions containing *X. laevis* tubulin, *X. tropicalis* tubulin, or a 50/50 mixture (Figure 2.12). At this concentration, *X. laevis* microtubules still grow approximately twice as fast as *X. tropicalis* microtubules. The growth velocity of the 50/50 mixture lies at the midpoint between the growth velocities of the single-species mixtures, indicating a linear increase in growth velocity as the proportion of *X. laevis* tubulin is increased. This trend is also reflected in steady-state microtubule mass, as the mass distribution of mixed tubulin microtubules falls between the single species' distributions.

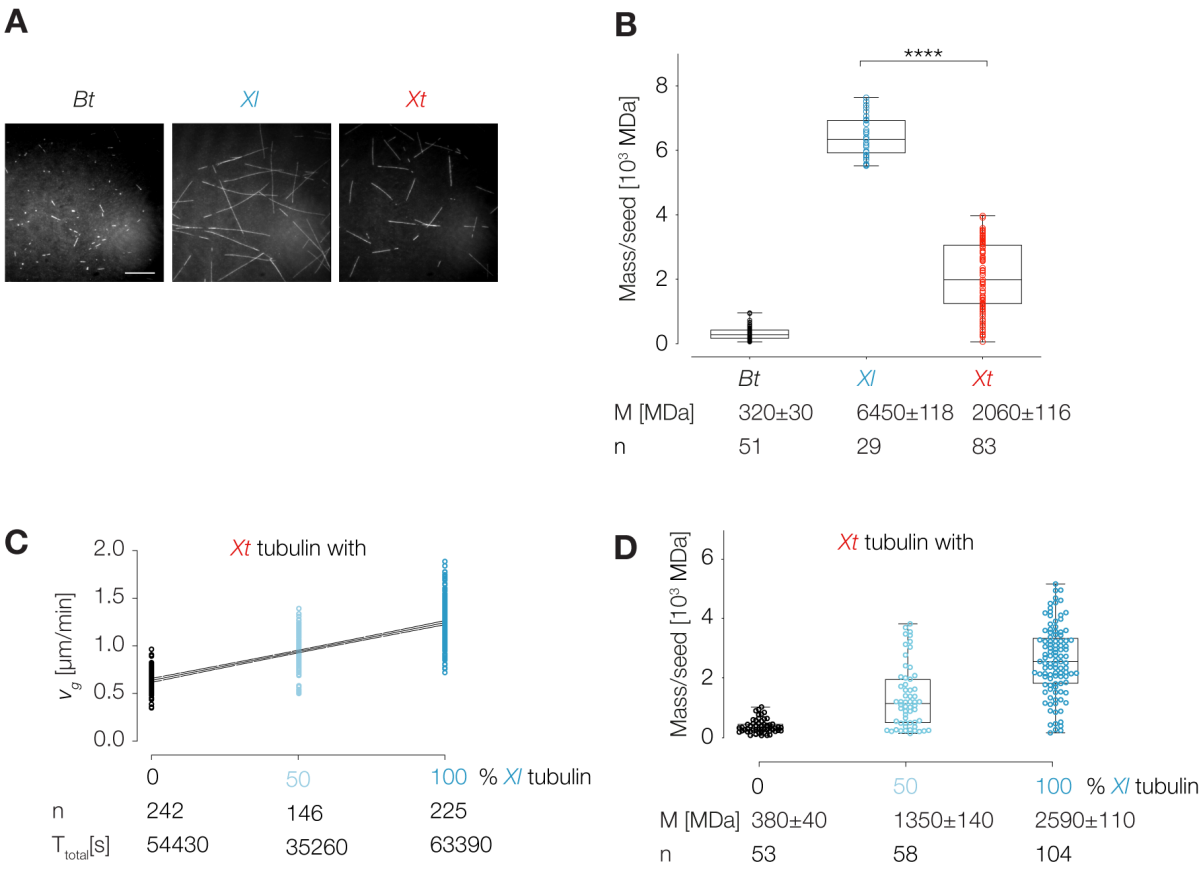

Figure 2.12 Modulation of microtubule length and mass by titrating tubulin sources. (A) Representative TIRF images of microtubules polymerized from *Bt*, *Xl*, and *Xt* tubulin at 9 mM at steady state. Scale bar represents 15 mm. (B) Mean microtubule mass per seed was calculated by measuring the length of each microtubule grown per seed (total

number of measured seeds [n] indicated) and converting length to mass by assuming that one micrometer of microtubule polymer contains 178.75 MDa of tubulin[45]. Mass per seed values were pooled across at least 4 independent experiments for each species. Mean microtubule mass per seed for *Bt*, *Xl*, and *Xt* microtubules were 320 ± 30 MDa, 6,450 ± 118 MDa, and 2,060 ± 116 MDa, respectively, with $p_{(Xl, Xt)} < 0.0001$ (Mann-Whitney test). (C) Growth rates were measured from microtubules assembled from *Xl* tubulin, *Xt* tubulin, and a 50/50 mixture at a final concentration of 6 µM. *Xt* microtubules grew at 0.63 ± 0.006 µm/min, mixed microtubules grew at 0.96 ± 0.015 µm/min, and *Xl* microtubules grew at 1.24 ± 0.015 µm/min. The linear regression is displayed with the 95% confidence interval. (D) Microtubule mass per seed was calculated for single-species and mixed microtubules at 6 µM as in (C). Mean microtubule masses for *Xt*, mixed, and *Xl* microtubules were 380 ± 40 MDa, 1,350 ± 140 MDa, and 2,590 ± 110 MDa, respectively, with $p_{(Xt, Mix)}$, $p_{(Mix, Xl)}$, and $p_{(Xt, Xl)} < 0.0001$. Adapted from Figure 3 of Hirst et al 2020.

2.2.11 Tubulin cannot be depleted from extracts without excessive dilution

Size control factors that have been identified in *X. laevis* and *X. tropicalis* do not individually account for the full difference in spindle length between the two species. To test for the relative contribution of tubulin identity in determining spindle length, several attempts were made to replace the tubulin of one species with that of the other in CSF-extract to test whether tubulin replacement results in a change in spindle length (Figure 2.13). It has been previously reported that pull-down assays do not significantly reduce tubulin concentration in CSF-extract[46]. Indeed, multiple pull-down assays using either an anti-tubulin antibody or the TOG1/2-GST fusion protein coupled to magnetic sepharose beads yielded tubulin in the elutions, but were unable to measurably reduce the tubulin concentration in X. laevis CSF-extracts after multiple rounds of depletion.

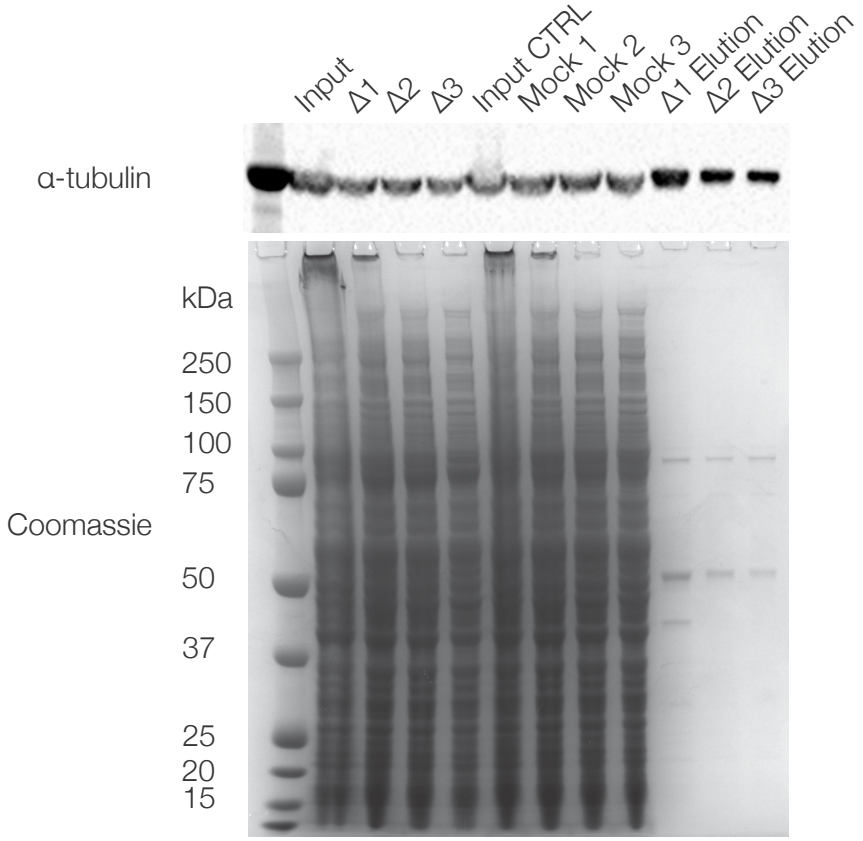

Figure 2.13 Tubulin pull-down from CSF-extracts using TOG1/2-GST-coupled magnetic sepharose beads. Shown are the CSF-extract input and extracts after three rounds of incubation with TOG1/2-GST-coupled (Δ) or empty (Mock) beads, as well as tubulin eluted from the beads using TOG column elution buffer. Extracts and elutions were separated by SDS-PAGE and Coomassie stained, and the tubulin concentration of extracts was monitored by western blot.

2.2.12 Tubulin-dependent changes in microtubule dynamics change spindle length *in silico*

As an alternative approach to *in vitro* tubulin depletion, the CytoSim modeling software (http://www.cytosim.org) was used to test whether the observed differences in microtubule dynamics in vitro account for differences in spindle length and mass in an in silico simulation of CSF-extract spindle assembly (Figure 2.14). CytoSim has been used to model spindle assembly in *Xenopus* egg extracts and *C. elegans* embryos and has demonstrated how modulation of parameters such as microtubule growth rate, catastrophe frequency, and severing rate determine steady-state spindle length[47–49]. To predict whether the observed differences in *Xl* and *Xt* microtubule dynamics influence

control of spindle length and mass, the growth rates of *Xl* and *Xt* microtubules assembled *in vitro* were first used to estimate by extrapolation microtubule growth rates at 20 μM, the physiological tubulin concentration in CSF-extracts[50,51]. These values (0.059 μm/s for *Xl,* 0.041 μm/s for *Xt*) were used as input parameters for spindle simulations of both *Xl* and *Xt* extract, which differed in microtubule severing rate by 100-fold. In both simulated extracts, the higher growth rate attributed to *Xl* tubulin produced spindles of greater length and mass than the *Xt* growth rate. Thus, simulated spindle assembly predicts that the difference in *Xl* and *Xt* microtubule growth rates is sufficient to set a greater spindle length and mass when microtubules are assembled from *Xl* tubulin than from *Xt* tubulin.

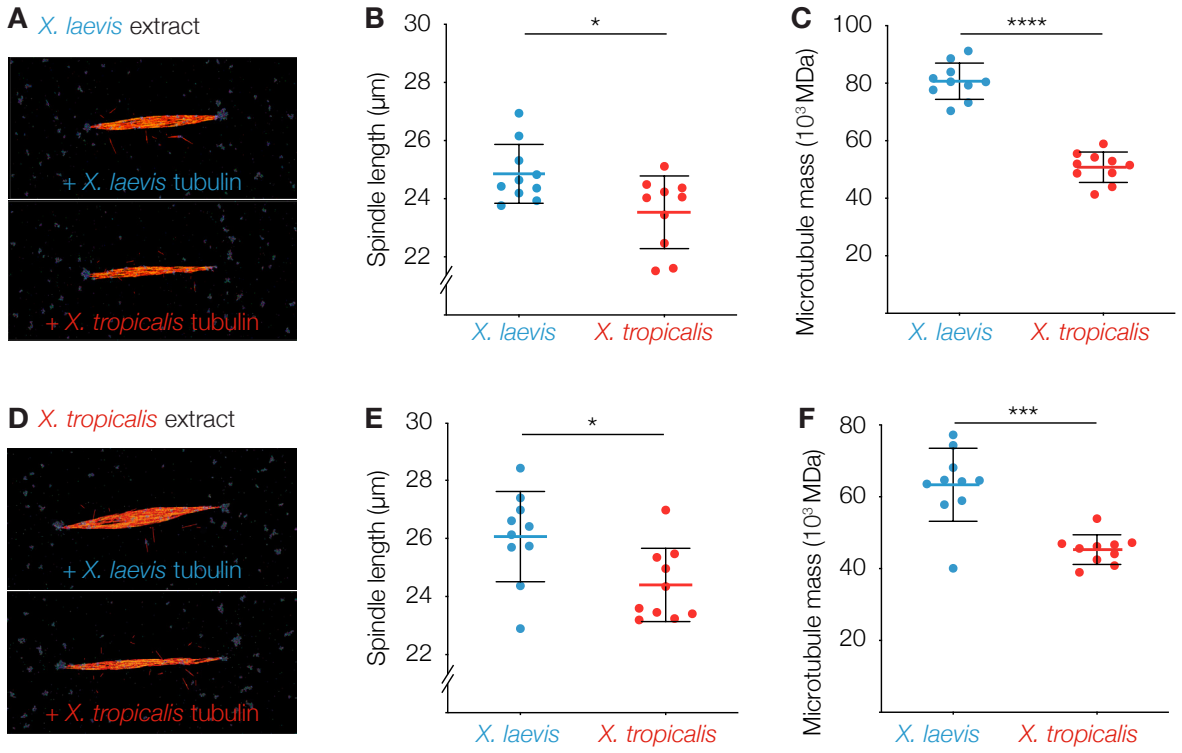

Figure 2.14 Simulated depletion and add-back of tubulin in *Xl* and *Xt* egg extract spindles. (A) Visualization of simulated spindles assembled in *Xl* egg extract with low rates of microtubule severing and *Xl* and *Xt* microtubule growth rates derived from measurements in Figure X. (B) and (C) Quantification of spindle length (μm) and mass (10^3 MDa) using *Xl* and *Xt* microtubule growth rates. (D) Visualization of simulated spindles assembled in *Xt* egg extract with high rates of microtubule severing and either *Xl* or *Xt* microtubule growth rates. (C) and (D) Quantification of spindle length and mass. Horizontal bars indicate mean (red or blue) and SD (black) and p-values (****<0.0001, ***<0.001, and *<0.05) were determined by Student's t-test with Welch's correction. Adapted from Figure S4 of Hirst et al 2020. Experiment and figure contributed by Abin Biswas.

2.2.13 Spindle mass and length increase with additional *Xenopus* tubulin

Purified tubulin from *X. laevis*, *X. tropicalis*, or *B. taurus* was added exogenously to spindle assembly reactions in CSF-extracts of each frog species. It has been previously reported that adding porcine brain tubulin to a concentration of 15 µM to CSF-extract does not change spindle length[46], and indeed, adding *B. taurus* tubulin to either frog extract up to a concentration of 10 µM, corresponding to a final total tubulin concentration of 30 µM, did not change spindle length or mass in our experiments. However, adding tubulin from either frog increased spindle length and mass in both extracts, and *X. laevis* tubulin caused a greater increase in both extracts than *X. tropicalis* tubulin (Figure 2.15). Adding 10 µM *X. tropicalis* to *X. laevis* extract increased spindle length by 21%, and adding *X. laevis* tubulin resulted in an increase of 31% (Figure 2.15 A). The effect was more pronounced in *X. tropicalis* extract even with the addition of a lower concentration of tubulin (8 µM instead of 10 µM), where the addition of *X. tropicalis* tubulin increased spindle length by 23% and *X. laevis* tubulin increased spindle length by 70% (Figure 2.15 B). Thus, highly active *Xenopus* tubulin, but not *Bt* tubulin, is able to increase spindle length and mass when the concentration is increased, and *Xl* tubulin shows a greater increase in both extracts than *Xt* tubulin, and can therefore account for differences in spindle length between species.

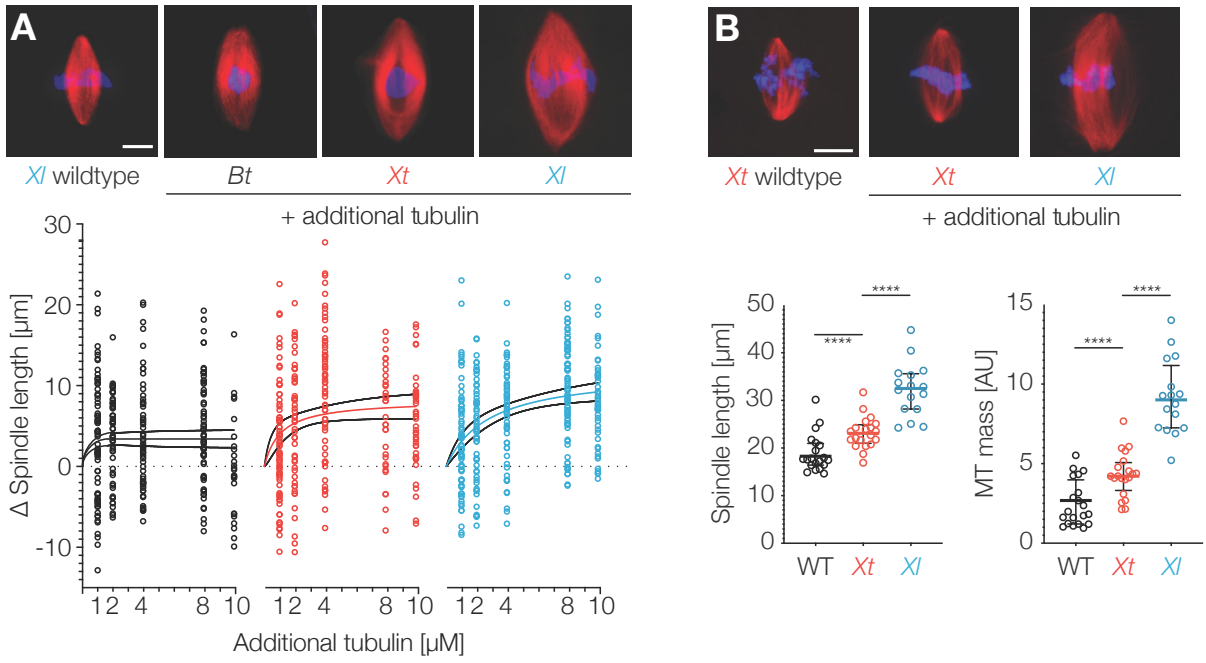

Figure 2.15 Spindle length and mass increase with additional *Xenopus* tubulin. (A) Images of *Xl* CSF-extract spindles assembled with 8 μM additional purified tubulin added to the reaction. Tubulin is shown in red and Hoechst stain in blue. Below is the quantification of the relative change in spindle length with increasing titrations of purified tubulin. (B) Spindles assembled in *Xt* CSF-extracts as in (A). Spindle length and mass, estimated from the fluorescent tubulin signal, are quantified below, with mean and SD shown. Adapted from Figure 4 of Hirst et al 2020. Experiments and figure contributed by Abin Biswas.

2.2.14 *Xenopus laevis* tubulin from different tissues differs in dynamic properties and post-translational modifications

Comparison of *Xenopus* egg and bovine brain tubulin is useful for identifying novel aspects of *Xenopus* tubulin biochemistry in comparison with a tubulin source that has a long history of use in the foundational experiments characterizing microtubule dynamics and interactions with other proteins[1,15]. However, the mammalian brain tubulin used in this and other studies comes from a distantly related vertebrate obtained by a purification method that does not yield the full complement of the cells' tubulin[28]. The isoform composition of brain tubulin, which produces high amounts of βIII tubulin relative to other cell types, is known to confer unique dynamic characteristics relative to other purified tubulins[24,52], but information on how the whole-cell tubulin complement influences microtubule dynamics among different tissues within a single organism remains limited.

To test for cell-type-specific differences in microtubule dynamics and tubulin PTMs in *Xenopus laevis* frogs, tubulin was TOG-affinity purified from whole-organ lysates of *X. laevis* brains and compared with purified egg tubulin in microtubule assembly reactions and western blots probing for PTMs. At 6 μM tubulin, the growth velocity of egg tubulin MTs was approximately twice that of brain tubulin MTs (0.658 ± 0.0978 vs. 0.365 ± 0.0716 μm/min) (Figure 2.16B). *Xl* brain tubulin also did not exhibit the high levels of spontaneous nucleation seen with CSF-extract tubulin at 12 μM (Figure 2.16A). At this concentration, *Xl* brain microtubules grew twice as fast as *Bt* microtubules (1.25 ± 0.173 vs 0.637± 0.160 μm/min) (Figure 2.16C). Thus, concerning their dynamic behavior, *Xl* brain microtubules exhibit an intermediate phenotype between *Xl* egg and *Bt* brain microtubules. Western blot analysis revealed *Xl* brain tubulin to be detyrosinated, polyglutamylated, and phosphorylated in a fashion similar to *Bt* brain tubulin (Figure 2.16D). However, no signal was detected for K40 acetylation or β-tubulin III, which would

be expected in mammalian brain tubulin[23,53,54] and were both present for the *Bt* tubulin sample. Additionally, the phosphoserine antibody appeared to show a stronger signal *Xl* egg than for brain tubulin. Together, these results indicate that TOG-affinity purified *Xl* brain tubulin has dynamic properties and a PTM signature distinct from both *Bt* brain and *Xl* egg tubulin, and that within a species, microtubules have tissue-specific dynamics that arise from intrinsic differences in the tubulins produced in different tissues.

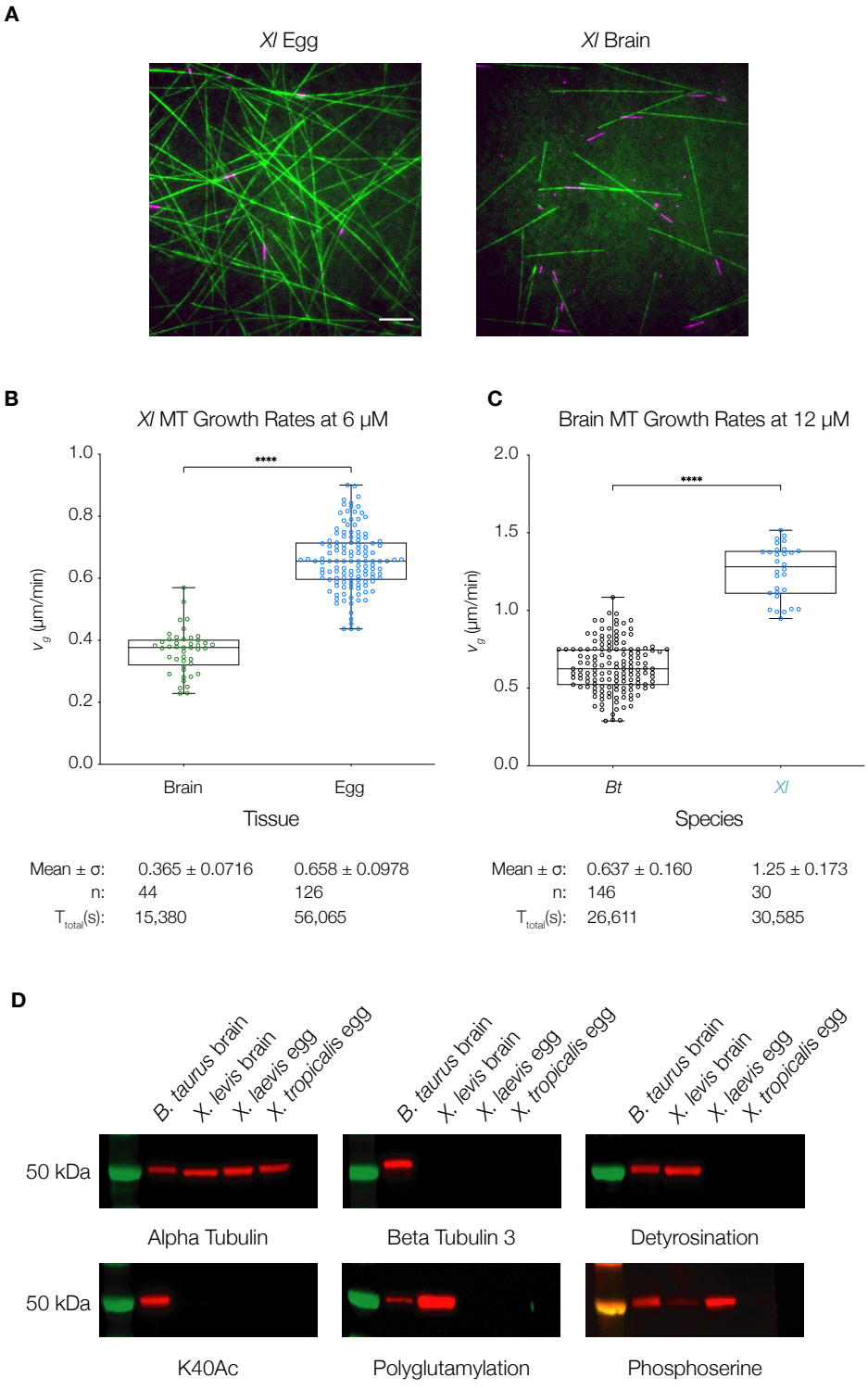

Figure 2.16 Comparison of *Xl* egg and brain tubulin growth rates and posttranslational modifications. (A) Still TIRFM images of microtubules assembled from purified *Xl* egg and brain tubulin after 30 minutes of polymerization at 37°. GMPCPP-stabilized seeds are shown in magenta and dynamic microtubules are shown in green. Scal bar = 10 µm. (B) At 6 µM tubulin, microtubules assembled from *Xl* brain tubulin grew at 0.365 ± 0.0716 µm/min and egg tubulin microtubules grew at 0.658 ± 0.0978 µm/min, with $p_{(brain, egg)} < 0.0001$. (C) At 12 µM tubulin, *Bt* brain microtubules grew at 0.637 ± 0.160 µm/min and *Xl* brain microtubules grew at 1.25 ± 0.173 µm/min, with $p_{(Bt, Xl)} < 0.0001$. (D) Western blots probing post-translational modifications found in purified *Bt* brain, *Xl* brain, *Xl* egg, and *Xt* egg tubulin. 300 ng of each tubulin were probed with antibodies against α-tubulin, mammalian β-tubulin III, detyrosinated tubulin, K40-acetylated α-tubulin (K40Ac), polyglutamylated tubulin, and phosphoserine. Mean v_g values, standard deviations (σ), n, and total times of observed microtubule growth (T_{total}) are indicated. P-values were calculated with the Mann-Whitney test.

Chapter 3. Purification and Biochemical Characterization of Plasmodium falciparum Tubulin

3.1 Introduction

The protozoan parasite *Plasmodium falciparum* provides an example of how microtubules perform diverse functions within a single-celled organism. *Plasmodium* species have a complex life cycle that progresses through the gut and salivary glands of its mosquito vector as well as the liver and blood of its mammalian host[55]. The many stages of *Plasmodium* development each require unique physiological adaptations to distinct intra- and extracellular environments[55–57]. Microtubules perform essential functions in most stages of the parasite life cycle, including formation of the mitotic and meiotic spindles, the flagellum of the male gametocyte, and the subpellicular cytoskeleton that contributes to distinct morphologies at different stages[58–61]. Disruption of *Plasmodium* microtubules has been shown to be detrimental to both parasite replication and transmission[26,62]. During the blood stages of a *Plasmodium falciparum* infection, when the clinical symptoms of malaria are apparent, the parasite undergoes several rounds of mitosis before dividing into individual merozoites that then exit the infected erythrocyte to infect new cells and continue the cycle. *P. falciparum* must also carefully regulate the organization of its microtubule cytoskeleton to retain transmissibility from the mosquito vector to the human host[26]. Cytoskeletal microtubules are highly stable, elastic, and resistant to microtubule destabilizing agents; however, replication of blood-stage parasites is inhibited by drugs that suppress microtubule dynamics, suggesting that these drugs likely target the mitotic spindle rather than structural microtubules in the parasite[26,63].

Studies using purified tubulin have contributed much to our understanding of how microtubule dynamics and interactions with other proteins influence microtubule organization and control parameters such as microtubule length and mass within the cell, but this approach has yet to be successfully applied to *Plasmodium*. Most characterizations of *Plasmodium* microtubules involve techniques such as cryoelectron tomography and fluorescence microscopy of the whole cell, which have in many cases provided detailed snapshots of microtubule organization, but do not capture microtubule dynamics within the parasite[59–62]. The localization of several *Plasmodium* MAPs and

motors have also been described and localized to structures such as the basal body of the flagellum *in vivo*, but there is still much work to be done to describe mechanistically how these proteins interact with tubulin and microtubules to determine the observed phenotypes[64–66]. Experiments utilizing purified tubulin and other components *in vitro* will be an important complement to established *in vivo* techniques for describing *Plasmodium*-specific aspects of microtubule assembly and organization.

The evolution of drug resistance in pathogens necessitates the identification of novel drug targets for treating infectious diseases, and mitotic inhibitors have over the years gained interest as possible antimalarial therapies[63,67,68]. Microtubules play an essential role in cell division in every eukaryote, and drugs that target microtubules are well established as treatments for diseases such as cancer due to their ability to disrupt the rapid, unregulated cell division characteristic of cancer cells[69]. Microtubules are also established drug targets in fungal and parasitic helminth infections[67,68].

Tubulin is a highly conserved protein, so an important property for any antimalarial therapeutic that targets microtubules is specificity for parasite tubulin over that of the host[63,70]. *Plasmodium falciparum* tubulin (*Pf* tubulin) shares greater homology with plant tubulin than mammalian, and indeed, evidence suggests antimitotic herbicides' activity specifically targets plant and, potentially, parasite tubulin. Oryzalin, for example, reversibly binds maize tubulin with a Kd of 95 nM[71], and in cultured cells, the IC_{50} is 37 nM. In comparison, the IC_{50} for vero monkey kidney cells is greater than 32 μM[72]. Mutagenesis studies and simulations suggest that dinitroanilines such as oryzalin bind a unique site on α-tubulin of apicomplexan parasites that is absent in mammalian tubulin[73]. Functional tubulin purified from *Tetrahymena thermophila*, which is sensitive to oryzalin, became resistant to oryzalin when α-tubulin point mutations found in oryzalin-resistant Toxoplasma gondii strains were introduced[74]. However, this has not been validated using purified Plasmodium tubulin or in the parasite itself[75].

Previous attempts to characterize parasite-specific drug-tubulin interactions using purified tubulin recombinantly expressed in bacteria faced a number of fundamental flaws. Tubulin activity is its ability to form dynamic microtubules. Helminth tubulin expressed in bacteria has been shown to form only "microtubule-like" structures, as visualized by cryo-EM[76], and *in vitro* reconstitution of microtubule dynamics have not been demonstrated. These structures appear as rings and small sheets of tubulin, not

fully-assemble microtubules. This suggests that the vast majority of tubulin in solution was not functional. Attempts to purify recombinantly express P. falciparum tubulin yielded protein that co-pelleted with bovine brain tubulin under conditions that promote microtubule assembly, but did not form microtubules when left to polymerize on its own, which suggests it was not fully active and only participated in a limited number of the necessary tubulin-tubulin interactions, only a small number of the tubulin molecules below the critical concentration were active, or the protein simply aggregated.

Attempts to measure herbicide binding to bacterially expressed *Plasmodium tubulin* with point mutations that have been shown *in vivo* to confer resistance to the herbicides oryzalin and APM in *T. gondii* were unable to show K_d increases more than 1.6-fold, which may be a result of improper folding of the putative binding site[75]. The lack of functional tubulin prevented the authors from demonstrating a rescue effect of tubulin activity conferred by the mutations in the presence of the inhibitors. They were also unable to test whether the mutations alone have a detrimental effect on microtubule dynamics, which has been hypothesized to be the mechanism responsible for the reduced fitness of the corresponding *T. gondii* mutants.

In contrast, purification of tubulin from whole organisms, including protozoans, reliably produces assembly-competent tubulin[29,30,74]. Tubulin has been purified from *Tetrahymena thermophila*, which, like *P. falciparum*, is a dinitroaniline-sensitive protist[74]. Cryo-EM showed that the purified protein is capable of forming microtubules, although dynamics were not measured. Furthermore, the authors were able to measure a 25-fold increase in oryzalin affinity relative to wild-type when they tested one of the mutations that had shown the modest change in K_d with recombinant Plasmodium tubulin. Indeed, the K_d value of the wild-type recombinant Plasmodium tubulin binding with oryzalin (15.5 μM) was even higher than the value measured for the natively purified resistant *T. thermophila* mutant (11.0 μM), which emphasizes the importance of having properly folded, functional tubulin when drawing conclusions about inhibitor binding and activity.

In order to characterize *P. falciparum* microtubule dynamics and drug specificity, the TOG-affinity purification approach was used to purify tubulin directly from blood-stage parasites. TIRF microscopy was used to quantify *P.falciparum* microtubule dynamics and provide a readout for tubulin activity in the presence of inhibitors in direct comparison with tubulin derived from its human host, and dose-response assays were

conducted to establish the physiological context of the *in vitro* experiments and to test additional microtubule inhibitors for antiplasmodial activity. Additionally, *P. falciparum* tubulin was profiled according to its isoform composition and PTMs in order to characterize other unique aspects of *P.falciparum* tubulin biology.

3.2 Results

3.2.1 Purification of *Plasmodium falciparum* tubulin from blood-stage cell cultures yields assembly-competent tubulin

The asexual blood stages of *Plasmodium falciparum* are responsible for the clinical symptoms of malaria and can be readily cultured in the lab[55,77]. Tubulin was purified from cultured blood-stage *P. falciparum* cells by TOG-affinity chromatography (Figure 3.1A-C). No tubulin was detected in the wash supernatant during the host erythrocyte lysis or the column flowthrough, confirming that the TOG column was able to deplete the full complement of *Pf* tubulin during purification (Figure 3.1D). As an additional control, the host cell lysis was monitored by western blot with a *P. falciparum*-specific Hsp70 antibody as well as a pan-specific α-tubulin to confirm that parasite cells remained intact until the final lysis step (Figure 3.1B). In contrast to *Xenopus* CSF-extracts, which typically yield 1 – 3 mg tubulin from an input of several milliliters of cell lysate, the tubulin yield from cultured *Plasmodium* cells was very low. The purification with the highest yield used an input of 120 mL of packed RBC pellets at a parasitemia of 5 – 10%, from which 435 µg tubulin was obtained.

Whereas previous attempts to purify affinity-tagged *Pf* tubulin bacterial cells were not able to demonstrate microtubule assembly *in vitro*, *Pf* tubulin purified using the TOG column formed dynamic microtubules, as visualized by TIRF-M (Figure 3.1E). To our knowledge, this is the first time active, assembly-competent tubulin has been purified from *P. falciparum*.

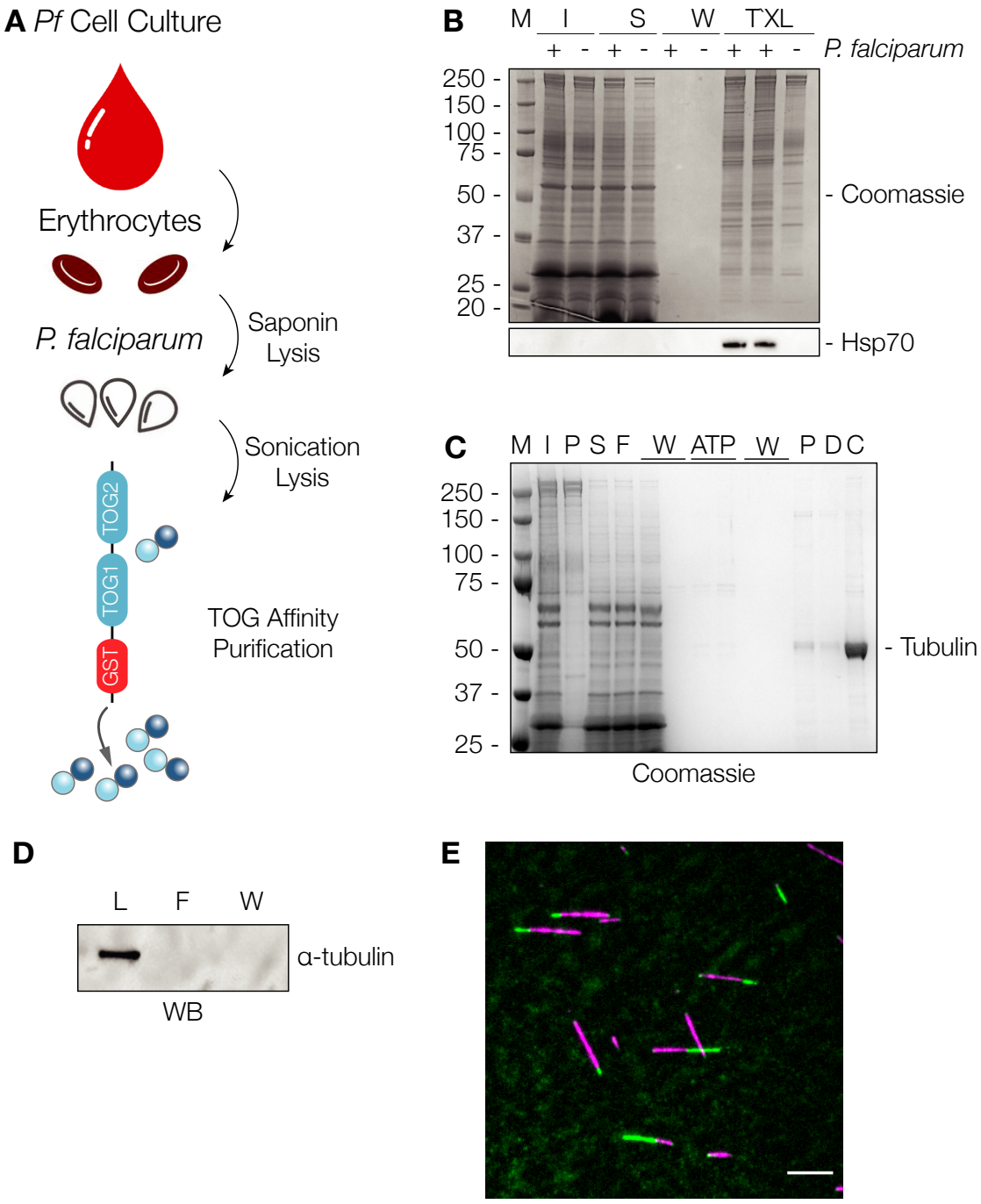

Figure 3.1 Affinity purification of blood-stage Plasmodium falciparum tubulin.
(A) Schematic detailing the Pf tubulin purification strategy. (B) Sequential lysis of infected (+) and uninfected (-) erythrocytes followed by lysis of *Plasmodium falciparum* cells. M: Molecular weight marker in kDa, I: Saponin lysis input, S: Supernatant, W: Wash, TXL: Triton-X lysis. Lower panel: Western blot against PfHsp70 as Pf lysis control. (C) Purification of tubulin from Pf lysate. M: Marker, I: Input, P: Pellet, S: Supernatant, F: Flowthrough, W: wash, ATP: ATP wash, P: Peak fraction, D: Desalt, C: Concentrated. (D) Western blot analysis of lysate (L), flowthrough (F) and wash (W) of the TOG affinity purification. (E) Representative TIRFM microscopy image of dynamic Pf microtubules (green) grown from stabilized seeds (magenta) at 37° with 6 µM tubulin. Scale bar: 5 µm.

3.2.2 Purified tubulin is free of host tubulin contamination

Some evidence suggests that human erythrocytes may contain small amounts of tubulin[78,79]. To exclude the possibility that purified *Pf* tubulin was contaminated with host protein, the presence of tubulin was monitored throughout the sequential host and parasite cell lysis and compared to uninfected erythrocytes by western blot (Figure 3.2A). A pan-specific monoclonal tubulin antibody (B-5-1-2, Abcam) only reacted with samples containing concentrated parasite cells or lysates and did not react with any stage of the lysis of uninfected erythrocytes. Furthermore, a vertebrate-specific beta tubulin antibody (SAP.4G5, Sigma-Aldrich), which recognized a purified HeLa tubulin positive control, reacted neither infected nor uninfected samples. Therefore, host tubulin is either absent from isolated *P. falciparum* cell lysates or is present at a low enough concentration that it is not detectable by western blot, whereas *Pf* tubulin is readily detectable.

To confirm that tubulin purified from isolated *P. falciparum* cells is free of host contamination, purified tubulin was digested with trypsin and analyzed by matrix-assisted laser desorption/ionization mass spectrometry (MALDI-MS) (Figure 3.2B). The corresponding peptide mass fingerprints revealed the presence of *Pf* alpha and beta tubulins. No unique host tubulin peptides were detected, thus confirming that purified *Pf* tubulin is free of host tubulin contamination.

3.2.3 Blood-stage *P. falciparum* tubulin is composed primarily of the α1 and β isoforms

The *P. falciparum* genome encodes one beta tubulin and two alpha tubulin isoforms, and antibody-based experiments have suggested that α1 is the predominant isoform at the protein level during blood stages[80–84]. The alpha tubulin mass fingerprint from the trypsin digest shows peaks corresponding to peptides that are shared by both α1 and α2 tubulins with the exception of the peak at 1,791.7 Da, which is a unique peptide corresponding to amino acids 340 – 352 of α1 tubulin (Figure 3.2B). A Thr→Ser mutation is found in α2 tubulin in this region of the sequence and there was no signal at the corresponding mass of 1,584.7 Da.

As an alternative approach, intact proteins were also analyzed by MS. Preliminary data (not shown) show a dominant α tubulin peak at 50,294 Da, which matches well with the mass predicted from the primary sequence at 50,296 Da of αI (Uniprot ID Q6ZLZ9). Notably, a peak that would correspond to α2 tubulin at 49,651 Da (Uniprot ID Q8IFP3) is

absent from the spectrum. Together, the results from the two mass spectrometry approaches suggest that α1 tubulin is the predominant α tubulin isoform of blood-stage *P. falciparum* together with β tubulin and that no human tubulin contamination is present.

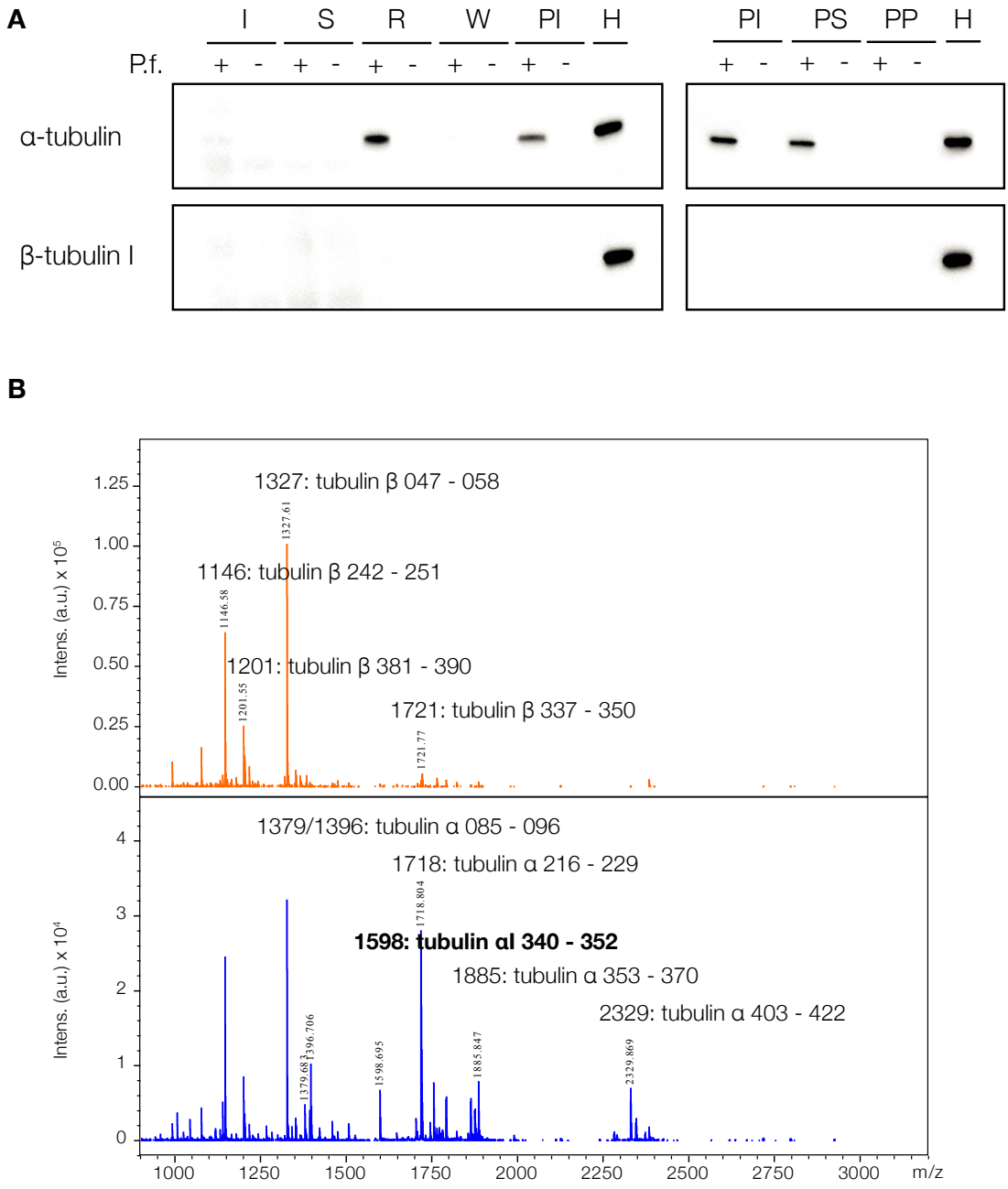

Figure 3.2 Western blots and mass spectra demonstrating purified blood-stage *P. falciparum* tubulin purity and isoform composition. (A) Sequential lysis of host erythrocytes and parasite cells. I = red blood cell (RBC) lysis input, S = RBC lysis supernatant, R = resuspended parasite pellet, W = parasite pellet wash, PI = parasite lysis input, PS = parasite lysis supernatant, PP = parasite lysis pellet, H = HeLa tubulin control. Pf + and - indicate infected and uninfected RBC cultures, respectively. (B) MALDI-MS Trypsin peptide mass fingerprint. *P. falciparum* beta tubulin peptide masses are indicated in orange and alpha tubulin masses are in blue. Bold text indicates the unique α1 isoform peptide that was detected.

3.2.4 Blood-stage *P. falciparum* tubulin is at least partially detyrosinated

Evidence suggests tubulin PTMs are found in apicomplexan parasites, and in some cases are necessary for parasite replication[21,83]. For example, immunofluorescence assays have shown antibodies against polyglutamylated tubulin localizing to microtubule-organizing centers in *P. falciparum* schizonts, and the acetylation of lysine 40 has been shown to be necessary for proper cell division in *T. gondii*[21,83]. In order to characterize the PTM status of purified *Pf* tubulin, tubulin was probed with antibodies against tyrosination, detyrosination, polyglutamylation, and lysine 40 acetylation (Figure 3.3). In contrast to a previous report, the polyglutamylation antibody GT335 did not react with pure *Pf* tubulin; however, western blots from that study show relatively weak signal compared to bovine brain tubulin, so the signal may have been below the detection threshold in this case. Interestingly, *Pf* tubulin interacted with an antibody against detyrosinated tubulin, which has not previously been described in *Plasmodium.* Detyrosination is typically associated with longer-lived microtubules[54], which may indicate that the stable subpellicular microtubules are a substrate for a detyrosinase. Furthermore, no signal was found with an antibody against lysine 40 acetylation, despite lysine 40 being found in the α1 tubulin sequence, so it is yet to be determined whether *P. falciparum* lacks a functional tubulin acetyltransferase or if this modification is found in other stages.

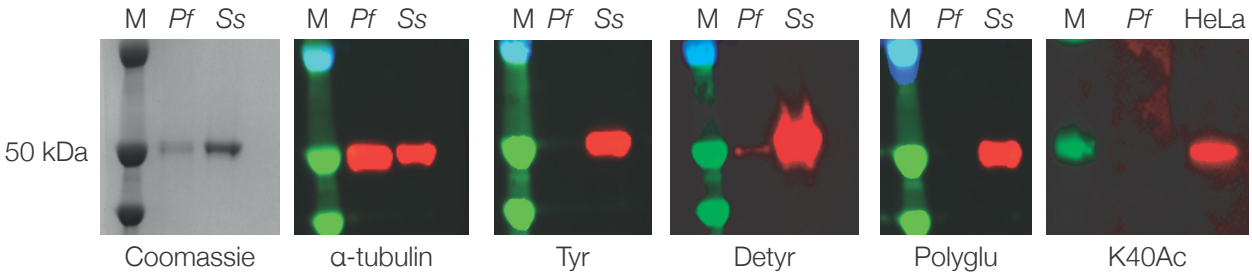

Figure 3.3 Western blots probing post-translational modifications found in purified *Pf* tubulin. α-tubulin is a loading control, Tyr recognizes the C-terminal EEY epitope of tyrosinated tubulin, Detyr recognizes the detyrosinated C terminus of α-tubulin, Poly-Glu recognizes epitopes containing acidic residues modified with a chain of at least 2 glutamyl residues, and K40 recognizes acetylated lysine at position 40 of α-tubulin.

3.2.5 Purified Plasmodium falciparum tubulin has similar dynamic characteristics to mammalian tubulin

Microtubules are known to be found in the *P. falciparum* blood stages as both stable subpellicular microtubules and dynamic spindle microtubules[72,85]. However, the intrinsic dynamic properties of *Pf* microtubules have to date not been characterized. Microtubules were assembled from purified *Pf* tubulin at 6 μM *in vitro* and microtubule dynamics were quantified as in Figures 2.4 and 2.5 and compared to microtubules assembled from tubulin purified from the human kidney cell line HEK293 as well as bovine brain tubulin (Figure 3.4). HEK293 tubulin was used as a host tubulin control because it is purified from an actively dividing human cell line. All parameters showed a statistically significant difference between *Pf* and HEK293 microtubules; however, in general, the effect size was small. *Pf* microtubules exhibited a slightly higher growth rate (0.385 ± 0.097 μm/min vs. 0.348 ± 0.074 μm/min, $p_{Pf,\ HEK} < 0.0001$) and lower catastrophe frequency (0.00469 ± 0.00354 s^{-1} vs 0.00581 ± 0.00124 s^{-1}, $p_{Pf,\ HEK} < 0.0001$) than HEK293 microtubules, whereas HEK293 microtubules had a higher rate of rescue than *Pf* microtubules (2.96 ± 1.70 s^{-1} vs 0.721 ± 1.506 s^{-1}, $p_{HEK,\ Pf} < 0.0001$). Overall, while *Pf* and HEK293 display minor differences in growth rate and microtubule stability, the parasite and host microtubules have similar growth dynamics at 37° *in vitro*.

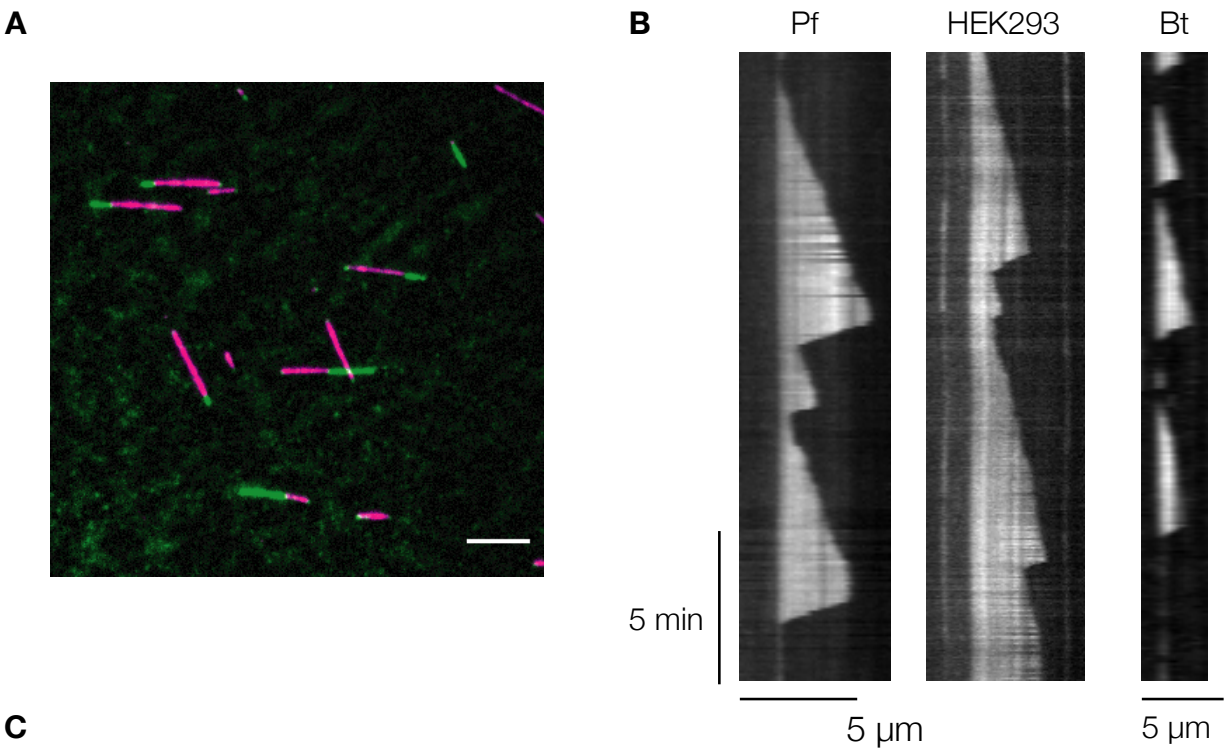
A
B
Pf
HEK293
Bt
5 min
5 µm
5 µm

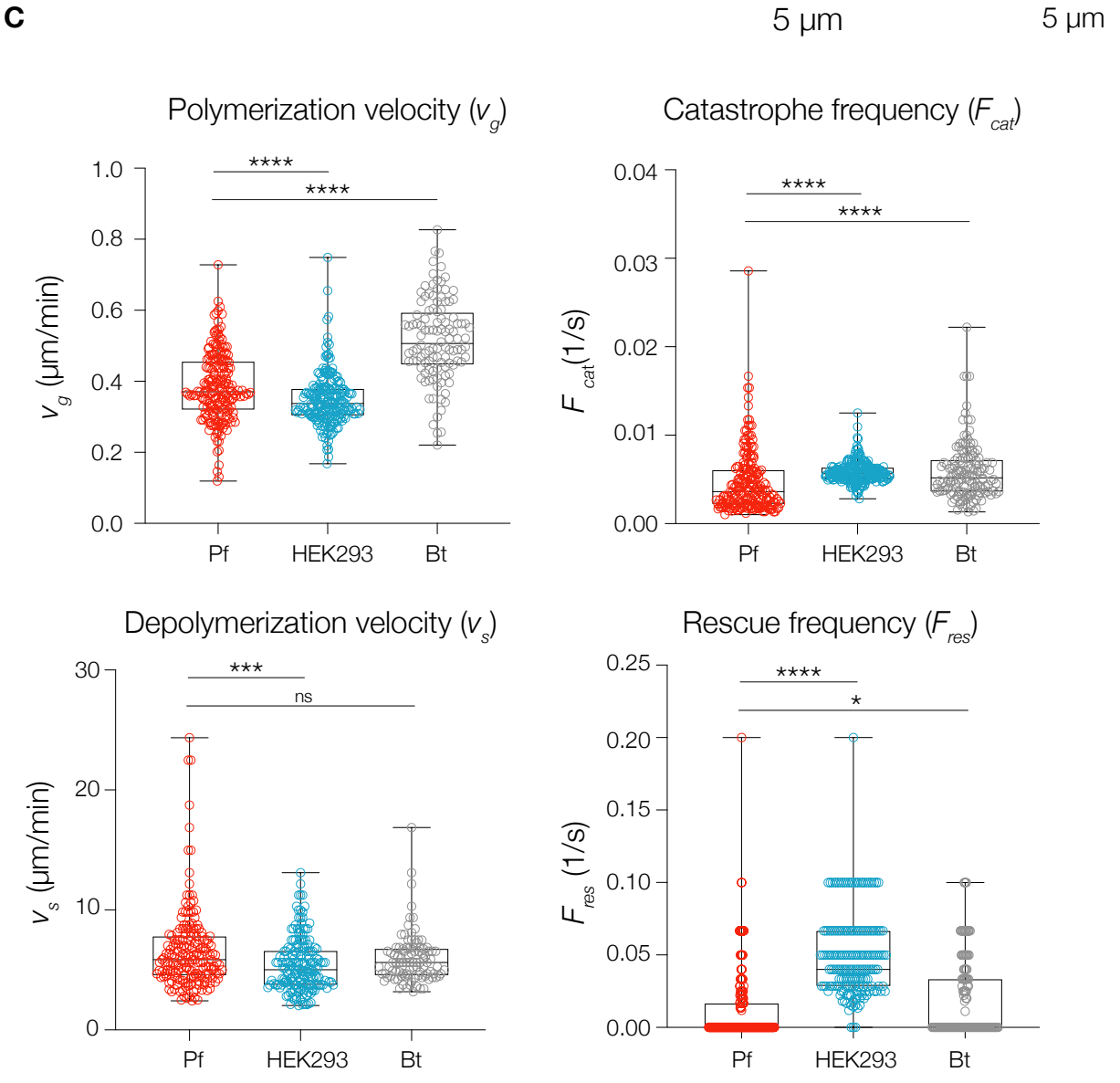
C
Polymerization velocity (v_g)
v_g (µm/min)
1.0
0.8
0.6
0.4
0.2
0.0
****
****
Pf
HEK293
Bt
Catastrophe frequency (F_{cat})
F_{cat} (1/s)
0.04
0.03
0.02
0.01
0.00
****
****
Pf
HEK293
Bt
Depolymerization velocity (v_s)
v_s (µm/min)
30
20
10
0
***
ns
Pf
HEK293
Bt
Rescue frequency (F_{res})
F_{res} (1/s)
0.25
0.20
0.15
0.10
0.05
0.00
****
*
Pf
HEK293
Bt

Figure 3.4 *P. falciparum* microtubules exhibit dynamic properties similar to mammalian microtubules *in vitro.* (A) Representative TIRF microscopy image of dynamic Pf microtubules (green) grown from stabilized seeds (magenta). Scale bar: 5 µm. (B) Representative TIRF kymographs showing dynamic HEK293 and *Pf* microtubules at 6 µM tubulin and bovine brain microtubules at 9 µM. (C) Parameters of dynamic instability. All values were obtained from measurements of microtubules pooled over at least three independent experiments and all p-values are calculated with the Mann-Whitney test. HEK293 microtubules grow at 0.348±0.074 µm/min (9.44±2.01 dimers/s), Pf microtubules at 0.385±0.097 µm/min (10.4±2.63 dimers/s) with $p<0.0001$ (n = 198 and 194, respectively). HEK293 microtubules depolymerize at 5.46±2.22 µm/min (148±60.0 dimers/s), Pf microtubules at 6.62±3.36 µm/min (179±90.9 dimers/s) with $p=0.0002$ (n = 174 and 185, respectively). Catastrophe frequencies are reported as the inverse of microtubule lifetimes. HEK293 microtubules catastrophe at 0.00581±0.00124 s^{-1} and Pf microtubules catastrophe at 0.00469±0.00354 s^{-1} with $p<0.0001$ (n = 198 and 194, respectively). Rescue frequencies are reported as the inverse of the duration of each depolymerization event. Events without a rescue are given a value of zero. Pf microtubules rescue at 0.721±1.506 s-1 and HEK293 microtubules at 2.96±1.70 s-1, with $p<0.0001$ (n = 174 and 185, respectively). For the modified box-and-whiskers plots the boxes range from 25th to 75th percentile, the whiskers span the range, and the horizontal line marks the median value. Measurements of *Bt* microtubule dynamics are adapted from Figure 2.5 for comparison.

3.2.6 Microtubule-targeting herbicides selectively inhibit taxol-stabilized and dynamic *P. falciparum* microtubules

Previous studies have suggested that inhibition of blood-stage *P. falciparum* cell growth by the herbicides oryzalin and amiprofos methyl (APM) is the result of the inhibition of microtubule assembly, and that these compounds selectively inhibit parasite rather than host microtubules[72,74,75]. However, parasite-specific microtubule inhibition by oryzalin and APM has not previously been directly demonstrated. To test whether microtubule inhibition is indeed the mechanism of action of these compounds against the parasite, and whether the compounds selectively interact with parasite over host microtubules, taxol-stabilized (Figure 3.5A) and dynamic microtubules (Figure 3.5B) were assembled *in vitro* in the presence or absence of oryzalin and APM in comparison with mammalian tubulin controls. Taxol-stablized *Pf* microtubules at 3 µM tubulin were inhibited by oryzalin concentrations as low as 1 µM, and dynamic *Pf* microtubules at 6 µM showed no polymerization at 2.5 µM oryzalin. In both cases, mammalian microtubule growth (porcine brain and HEK293 tubulin) remained unchanged. APM also inhibited *Pf* microtubule growth at 10 µM and did not inhibit HEK293 microtubules. Titrations of

oryzalin at 6 μM tubulin show that *Pf* microtubule growth velocity decreases with increasing oryzalin concentration over the range of 0.5 – 2.5 μM oryzalin, whereas HEK293 microtubule polymerization remains unchanged up to 25 μM oryzalin (Figure 3.5C). Thus, oryzalin and APM both selectively inhibit *Pf* over mammalian microtubule growth *in vitro*, and oryzalin is able to inhibit polymerization at substoichiometric concentrations relative to *Pf* tubulin.

An additional observation was that taxol caused *Pf* microtubules to spontaneously nucleate, branch, and grow with greater curvature than porcine brain microtubules, which remained straight and only nucleated from seed ends at the same concentration. The structure of *Pf* microtubules is unknown, and the possibility that taxol exerts novel effects on the *Pf* microtubule lattice warrants further study.

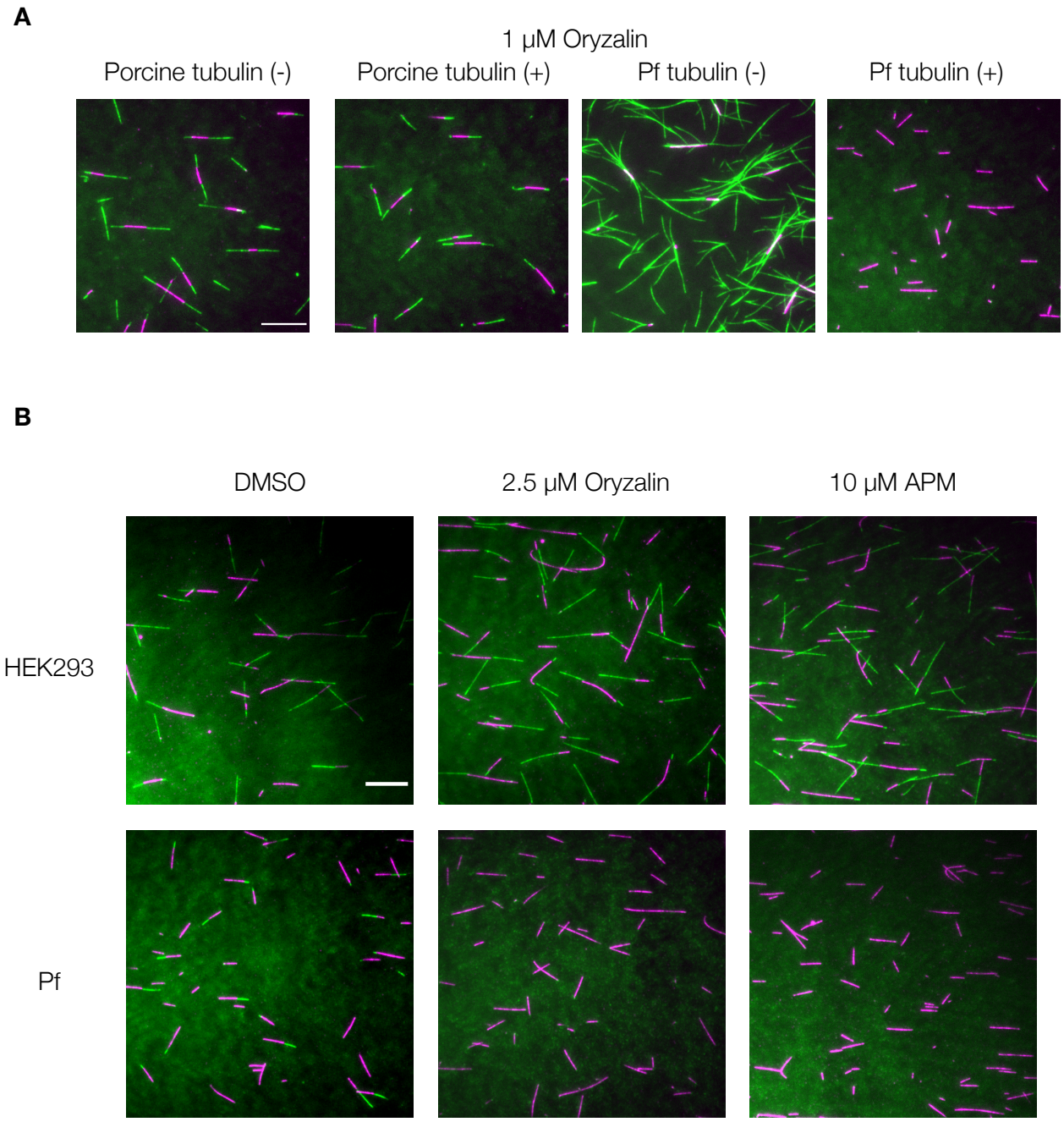
A
1 μM Oryzalin
Porcine tubulin (-)
Porcine tubulin (+)
Pf tubulin (-)
Pf tubulin (+)
B
DMSO
2.5 μM Oryzalin
10 μM APM
HEK293
Pf
C
Pf MT Growth at 6 μM Tubulin
HEK293 MT Growth at 6 μM Tubulin
v_g (μm/min)
1.5
1.0
0.5
0.0
No growth
0
1
2
3
[Oryzalin] (μM)
1.0
0.8
0.6
0.4
0.2
0.0
No growth
0
50
100
[Oryzalin] (μM)

Figure 3.5 Oryzalin and APM are Pf-specific microtubule inhibitors. (A) Images of microtubules assembled from porcine brain and Pf tubulin in the presence of 3 μM taxol with (+) or without (-) 1 μM oryzalin. (B) Microtubules assembled from purified HEK293 or Pf tubulin assembled in the presence of 1% DMSO, 2.5 μM Oryzalin, or 10 μM APM. All images were captured after 10 minutes of imaging at 37°. Taxol-stabilized or dynamic microtubules are shown in green, GMPCPP-stabilized microtubule seeds are shown in magenta. Scale bars: 10 μm. (C) *Pf* and HEK293 microtubule growth rates in the presence of oryzalin with 6 μM tubulin.

3.2.7 Oryzalin and amiprofos methyl inhibit blood-stage parasite growth

To test for inhibition of blood-stage parasite growth in the presence of oryzalin and APM, static *P. falciparum* cultures were grown for 96 hours with serial dilutions of the two herbicides (Figure 3.6). Parasite growth at the end of 96 hours was measured by fluorescence with the SYBR Safe DNA dye, and IC_{50} values were estimated from the dose-response curves. Average IC_{50} values for oryzalin and APM were 3.7 μM over five experiments and 4.3 μM from one experiment, respectively. These values are close to previously published values[72] and, notably, are within several μM of the concentrations needed to fully inhibit microtubule polymerization *in vitro*. Together, these results suggest that the inhibitory activity of oryzalin and APM against *P. falciparum* growth can be mechanistically explained by their inhibition of microtubule polymerization.

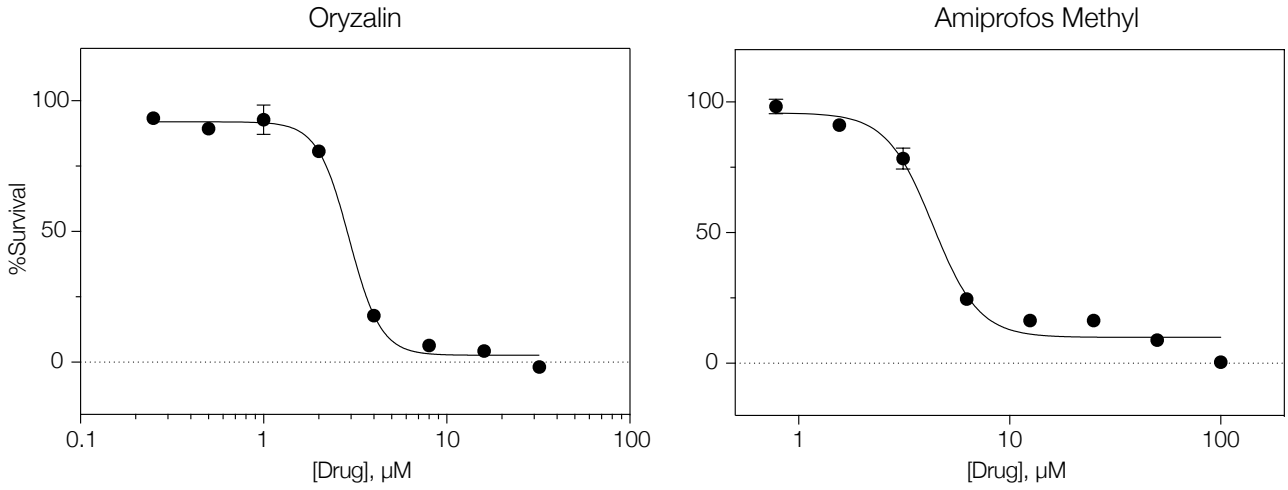

Figure 3.6 Representative dose-response curves of static *P. falciparum* cultures grown in the presence of oryzalin and APM. Each point represents %survival, as measured by SYBR Safe fluorescence relative to the untreated control, with three technical replicates for each condition. Error bars indicate SD between technical replicates.

3.2.8 Antihelmintic benzimidazoles and the insecticide azadirachtin are ineffective against *P. falciparum* blood stage growth

In an attempt to identify additional *Plasmodium*-specific microtubule inhibitors, dose-response assays were carried out with several additional established or putative microtubule inhibitors, including fenbendazole, albendazole, and azadirachtin. (Figure 3.7) Benzimidazoles such as fenbendazole and albendazole are a class of microtubule-targeting compounds used as fungicides and to treat infections by parasitic helminths and some protozoans[67,86–89], and azadirachtin is a pesticide that has shown activity against *Plasmodium berghei* that is suspected to disrupt microtubule organization during gametogenesis[90–92]. Of these three compounds, fenbendazole was the most effective in suppressing parasite growth with 50% parasite survival around 100 μM. However, as the effective concentrations of these compounds appeared to be at least 1 – 2 orders of magnitude higher than the IC50s of oryzalin and APM, they were not selected for follow-up *in vitro* experiments with purified *Pf* tubulin.

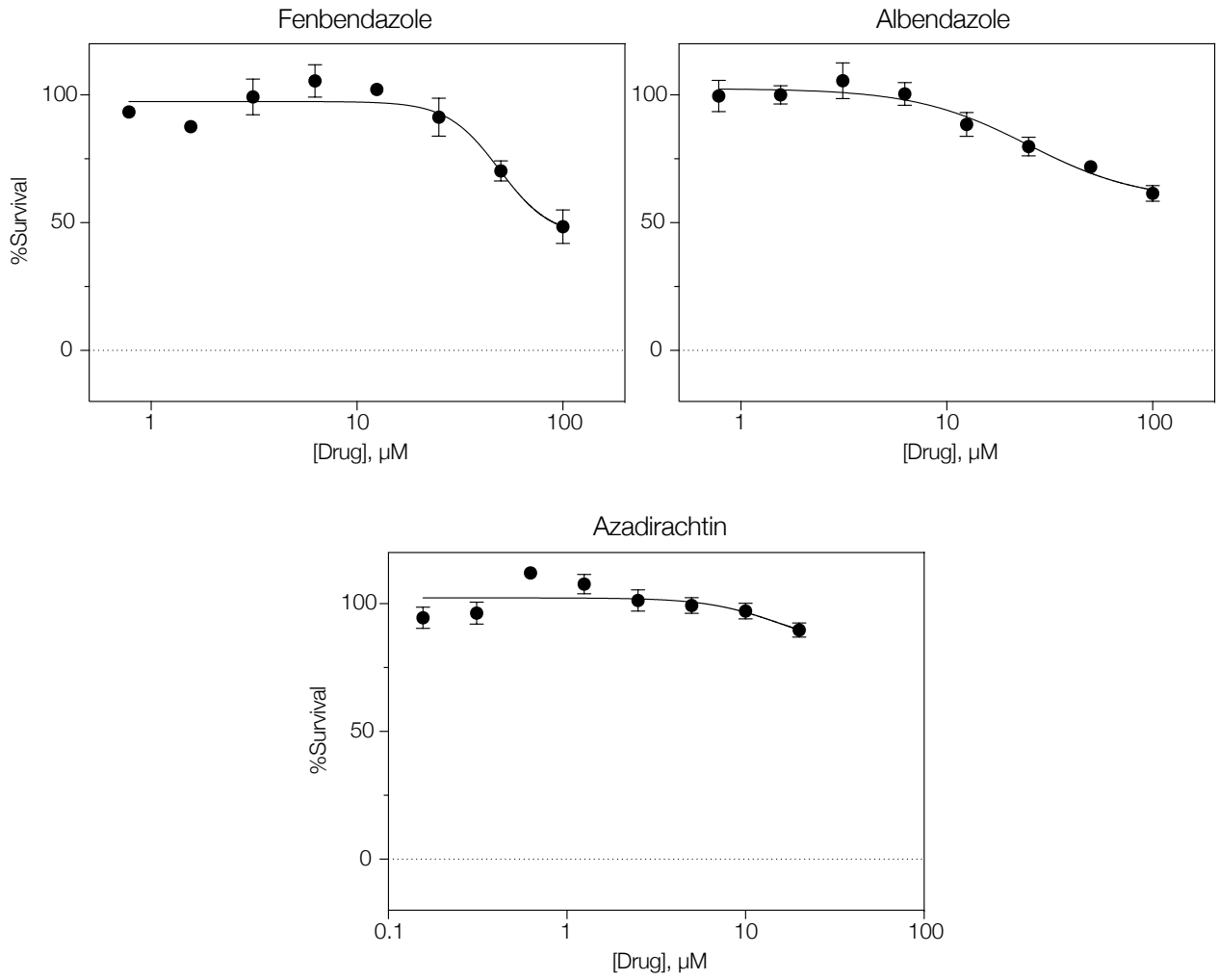

Figure 3.7 Dose-response curves of static *P. falciparum* cultures grown in the presence of fenbendazole, albendazole, and azadirachtin. Each point represents %survival, as measured by SYBR Safe fluorescence relative to the untreated control, with three technical replicates for each concentration. Error bars indicate SD between three technical replicates.

3.2.9 Ivermectin inhibits blood-stage parasite growth by an unknown mechanism

Ivermectin is a synaptic transmission blocker used to treat some arthropodal and helminthic parasite infections, and has recently gained interest as an agent for controlling malaria due to its ability to kill *Anopheles* mosquitoes[93]. Two previous studies have provided conflicting evidence as to whether ivermectin is also active against blood-stage *P. falciparum*[94,95]. While *Plasmodim spp.* are unicellular organisms and thus lack a nervous system, ivermectin has also been shown to inhibit importin α/β-mediated nuclear transport and has been suggested, but not definitively confirmed, to inhibit the dynamics of helminth microtubules by acting as a microtubule stabilizer[76,96].

A dose-response assay was carried out to evaluate the activity of ivermectin against blood-stage *P. falciparum* (Figure 3.8). Ivermectin was indeed able to inhibit with an average IC_{50} value of 418 nM across three experiments, roughly an order of magnitude lower in concentration than oryzalin or APM. Whether ivermectin can stabilize *Pf* microtubules was also tested *in vitro* with TIRF-M. *Pf* tubulin at 4 μM did not polymerize in the presence of 1 μM ivermectin (data not shown), whereas *Pf* tubulin readily polymerizes in the presence of 1 μM Taxol (see Figure 3.5A), suggesting that if ivermectin indeed acts as a microtubule stabilizer, it is less potent than Taxol. The limited availability of *Pf* tubulin prevented follow-up experiments to definitively determine whether ivermectin inhibits *Pf* microtubule dynamics *in vitro*, but the clear activity against blood-stage *Plasmodium falciparum* warrants further study into its mechanism of action.

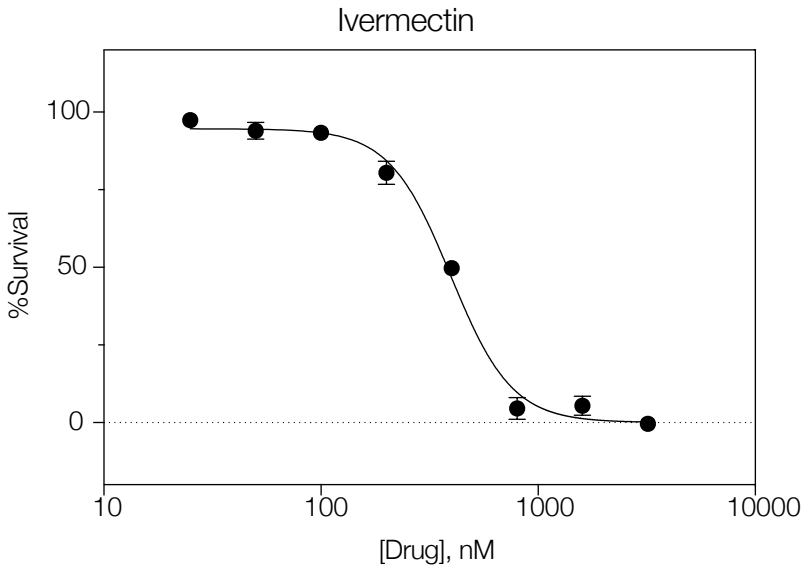

Figure 3.8 Representative dose-response curve of static *P. falciparum* cultures grown in the presence of ivermectin. Each point represents %survival, as measured by SYBR Safe fluorescence relative to the untreated control, with three technical replicates for each condition. Error bars indicate SD of technical replicates.

Chapter 4. Discussion and Outlook

4.1 Purified *Xenopus* tubulin reveals intrinsic differences in tubulin dynamic properties

The development of TOG-affinity purification of tubulin has enabled experiments demonstrating intrinsic, tubulin-dependent differences in microtubule dynamics between eukaryotes including plants, worms, mice, bovids, and humans[38,39,97]. Studies such as these have begun to shed light on the mechanistic basis for tubulin-dependent differences in microtubule dynamics and how cells can regulate microtubule dynamics by modulating isoform expression and posttranslational modifications[97,98]. Less clear, however, is how these observed differences in microtubule dynamics fit into a physiological context. How, for example, do the fast-growing and less-stable microtubules of *C. elegans* better serve the needs of that organism's cells than the slow-growing, stable microtubules of mammalian neurons? Are emergent phenomena that are known to be dependent on microtubule dynamics, such as spindle size control and scaling, also controlled by the characteristics of the tubulin pool itself that is made available by the cell?

This study has demonstrated that tubulin biochemistry confers intrinsic differences in microtubule dynamics even between closely related species. Furthermore, a direct connection is shown between these differences and their physiological consequence at the mesoscale, namely, that intrinsic tubulin dynamic properties can account for differential control of spindle size in the same cell type between *Xenopus laevis* and *Xenopus tropicalis*.

Control of microtubule growth rate and stability are established mechanisms for setting spindle length and modulating spindle size through development and between species[8,47,49,99]. Previous data has demonstrated that centrosome-nulceated microtubules grow roughly 20% faster in *X. laevis* CSF-extracts than *X. tropicalis* extracts, which suggests a connection between differential control of microtubule growth rate and the observed difference in spindle length between the two frogs.

While some tubulin PTMs and isoforms have been shown to influence microtubule dynamics, the list is far from complete, and none have been shown in *Xenopus*. An isoform or PTM difference in *Xl* vs *Xt* tubulin could reveal a novel mechanism for

controlling microtubule dynamics. To determine the mechanistic basis for the differences in microtubule dynamics, we looked for differences in posttranslational modifications and isoform composition between *Xl* and *Xt* tubulin. While the isoforms and PTMs were overall very similar, *Xl* tubulin appeared to carry a phosphorylation that *Xt* tubulin did not. Tubulin phosphorylation can have different effects on microtubule dynamics depending on the modified isoform and the position of the modification. For example, phosphorylation of Ser-165 of alpha tubulin increases microtubule growth velocity in MCF-10A cells, whereas the modification has an inhibitory effect at Ser-172 of beta tubulin[100,101]. Alternatively, the differences in dynamics may be encoded in subtle differences in the primary sequence of the tubulin homologs in the regions that determine the structure of the lateral protofilament interface. A structural comparison of *C. elegans* and mammalian brain tubulin has shown that higher structural order in the M-loop and H1-S2 loop of alpha tubulin is correlated with faster microtubule growth; structural experiments may reveal whether this holds true for Xenopus[30]. While we have identified possible mechanisms for the differences in *Xl* and *Xt* microtubule dynamics, more experiments will be needed to confirm them.

4.2 Intrinsic differences in tubulin dynamic properties account for differences in spindle size

Whereas previous studies of spindle size control and scaling have focused on microtubule-associated proteins and motors that regulate microtubule dynamics, this study address the question of whether differences in tubulin itself can contribute to setting spindle length. *X. laevis* microtubules grow faster and have longer lifetimes and an increased length when compared to *X. tropicalis* microtubules *in vitro*. Both of these parameters predict a longer spindle length in *X. laevis* than *X. tropicalis* according to the mass balance model.

Computational modeling of spindle assembly indicated that the measured differences in microtubule dynamics between *X. laevis* and *X. tropicalis* can influence spindle length and mass even when microtubule severing is accounted for. Depletion of tubulin from CSF-extracts under conditions that would allow subsequent spindle assembly were unsuccessful, which prevented direct experimental confirmation of the *in silico* models of tubulin depletion and add-back. However, we were able to add

concentrated purified *Xl* and *Xt* tubulin to CSF-extracts of both frogs for spindle assembly reactions that supported our inferences of the effects of tubulin dynamics on spindle size control.

Increasing tubulin concentration increases both microtubule growth rate and stability, which has been demonstrated here and in other studies[30,44]. However, the degree to which microtubule growth rate, and by extension spindle length, is increased depends on the source of tubulin. The addition of slow-growing bovine brain tubulin to spindle assembly reactions in CSF-extracts of either *Xenopus* species did not result in an increase in spindle length, whereas adding the relatively more active *Xenopus* tubulins did. Furthermore, the addition of *Xl* tubulin appeared to cause a greater increase in spindle length than that achieved by *Xt* tubulin at the same concentration. These results support the hypothesis that higher microtubule growth rates and lifetimes lead to a longer spindle and that the differences in intrinsic *Xl* and *Xt* microtubule dynamics are sufficient to produce a larger spindle in *Xl* eggs and CSF-extracts, even when accounting for other microtubule regulators that differ between the two species.

4.3 Purified *Xenopus laevis* brain and egg tubulins reveal tissue-dependent intrinsic differences in tubulin dynamic properties

Recent studies have provided evidence that different cell types produce tubulin with different intrinsic dynamic properties[97]. However, the existing data, to our knowledge, has not fully controlled for species and purification method. In this study, a direct comparison between TOG-affinity-purified tubulin of egg and brain tubulin of *X. laevis* frogs has demonstrated intrinsic tubulin-dependent differences in microtubule dynamics between different tissues derived from the same organism.

Microtubules assembled from purified *Xl* brain tubulin showed dynamic characteristics and a PTM pattern distinct from both *Xl* egg and bovine brain tubulin. For example, *Xl* brain microtubules grow slower than egg microtubules and appear to have a higher critical concentration, as evidenced by a lack of spontaneous nucleation at higher concentrations. This points to cell-type specific regulation of microtubule dynamics stemming from modulation of the biochemical makeup of the cell's tubulin population. On the other hand, they grow faster than bovine brain microtubules and are recognized by some, but not all, of the antibodies against PTMs shown in bovine brain

tubulin, showing that *Xl* brain microtubule dynamics are also distinct from microtubules of the same tissue type from a different species.

It is still unclear whether the differences between *Xl* and bovine brain microtubule dynamics stem from intrinsic differences between the species themselves, the different purification methods used to obtain the tubulin, or both. Our lab is in a position to address this question. We have obtained a bovine brain sample which we will use for a side-by-side comparison of the TOG-affinity purification and the classical tubulin cycling purification methods. This will allow us to show, for example, which isoforms (if any) the cycling method is biased towards and will help demonstrate the extent to which tubulin activity is lost during the cycling method relative to TOG-affinity purification. Additionally, we will have a bovine brain tubulin sample purified the same way as the *Xl* tubulin, which will allow for a better controlled comparison of these tubulins derived from the same tissues of different species.

4.4 TOG-affinity tubulin purification yields active, physiologically relevant *Plasmodium falciparum* tubulin

This study presents, to our knowledge, the first successful purification of active *P. falciparum* tubulin and reconstitution of *P. falciparum* microtubule dynamics *in vitro.* Previous studies produced tagged parasite tubulin expressed in and purified from bacteria, which was able to co-precipitate with bovine brain tubulin but, importantly, was not shown to form proper microtubule structures or reconstitute microtubule dynamics *in vitro*[75], precluding the study of the effects of parasite-specific microtubule inhibitors on microtubule dynamics and calling into question whether the binding affinity studies performed used properly folded protein. In contrast, we have purified physiologically relevant *Pf* tubulin from cultured *P. falciparum* cells and directly visualized and measured microtubule dynamics using TIRF microscopy, establishing a robust system for *in vitro* characterization of *Plasmodium* microtubule biology and drug inhibition.

A previous study that analyzed the *P. falciparum* tubulin pool by western blot suggested that both the α1 and α2 tubulin isoforms are present in the blood stages; however, the authors did not rule out cross-reactivity between the two antibodies, and the secondary antibodies used to for western blots relied on peroxidase luminescence and thus may not provide a quantitative picture of the isoform composition[83]. Our mass

spectrometry data demonstrate at the protein level that α1 is indeed the predominant tubulin isoform in *P. falciparum* blood stages. Given that α2 tubulin, rather than α1, has been shown to be the predominant isoform in *P. berghei* blood stages, it is unknown whether the two isoforms confer different intrinsic dynamic properties to microtubules. Replacing *Pf* α1 tubulin with the α2 isoforms of either *P. falciparum* or *P. berghei* may shed light on whether the essentiality of the α1 isoform in *P. falciparum* is a consequence of the protein itself or the genomic context of the α1 tubulin gene.

The relative simplicity of the isoform composition of tubulin in *P. falciparum* makes it a unique system for addressing questions that are of general interest to the fields of cell and microtubule biology. For example, microtubules are present as both stabilized subpellicular filaments and dynamic spindle microtubules in the blood stages. That α1 appears to be the only relevant α-tubulin isoform in these stages suggests that subpellicular microtubule stability and organization are determined by as yet unidentified proteins or PTMs. Determining how *Pf* cells are able to manage populations of both dynamic and stable microtubules from a low-complexity tubulin population is an interesting topic for future work, and can now be better addressed thanks to the availability of purified *Pf* tubulin that will allow, for example, studies of potential stabilization factors with physiologically relevant parasite tubulin.

Purification of single-isoform *Pf* tubulin may also provide insight on the utility of emerging tubulin purification techniques. A direct comparison of TOG-affinity-purified and recombinant *Pf* tubulin would be straightforward, because the analysis can be limited to the α1 and β isoforms, and native *Pf* tubulin appears to be mostly unmodified. Recombinant single-isoform tubulin purifications from insect cells that have shown success so far have generally relied on the use of multiple affinity tags, columns, and tag cleavage reactions[102], whereas the TOG-affinity purification method requires the use of only a single affinity column followed by rapid desalting and concentration steps. It has not yet been described to what extent recombinant tubulin retains its activity relative to the physiologically relevant tubulin obtained by the TOG-affinity method. If, however, an insect cell-based expression system can be utilized for *P. falciparum* tubulin, it would enable *in vitro* studies of dynamics and drug sensitivity of the α2 isoform is well, which could shed light on whether the two isoforms are functionally distinct.

4.5 Oryzalin and APM are species-specific microtubule inhibitors

This study describes the first direct evidence that antimitotic herbicides such as oryzalin and APM suppress microtubule dynamics through interactions with the soluble tubulin dimer and that these interactions are specific to parasite tubulin. Oryzalin and APM were able to inhibit parasite microtubule growth *in vitro,* whereas microtubules assembled from tubulin derived from the actively dividing human cell line HEK293 was left unchanged at the same tubulin and inhibitor concentration. Comparisons of microtubule dynamics between *Pf* tubulin and HEK293 tubulin revealed that the dynamic properties of *Pf* and host microtubules are similar *in vitro*, which suggests the sensitivity of *Pf* tubulin and relative resistance of HEK293 tubulin to inhibitor treatment is indeed the result of different binding affinities rather than a difference in tubulin activity.

The oryzalin binding site on *Plasmodium* tubulin has been predicted but not confirmed experimentally, and the structural consequences of oryzalin binding are as yet unknown. Mutations in α-tubulin have been associated with oryzalin resistance in two other oryzalin-sensitive parasites, *Tetrahymena thermophila* and *Toxoplasma gondii.* However, many of these mutations also alter the assembly properties of tubulin, making it difficult to distinguish the mechanism of decreased oryzalin affinity from the effects of altered tubulin dynamics such as increased microtubule stability or a reduction in critical concentration[74,103]. Many oryzalin resistance mutations come at a cost to fitness, supporting the hypothesis that they alter microtubule dynamics. Additionally, the protozoa in which oryzalin resistance has been described have diverse microtubule structures. The cells of *T. thermophila*, for example, are decorated with cilia, structures that contain stabilized microtubules that are not found in the blood stages of *P. falciparum*. Given the diverse roles microtubules play among these different organisms, it is unclear whether a resistance mutation that impacts microtubule dynamics and/or fitness in one organism will have similar consequences in another.

A study investigating the effects of ivermectin on the polymerization of *Haemonchus contortus* tubulin hypothesized that ivermectin interacts directly with tubulin to disrupt microtubule dynamics and acts as a microtubule stabilizer[76]. The authors showed an increase in absorbance at 340 nm in reactions containing recombinantly expressed and purified associated with the presence of ivermectin; however, they were not able to demonstrate that their purified tubulin formed dynamic

microtubules. Therefore, it is unknown whether, under the conditions tested, ivermectin truly stabilizes microtubules, or simply causes off-pathway aggregates to form at high concentrations.

In this study, the first steps were made to address whether ivermectin is indeed active against *P. falciparum* microtubules. Dose-response assays of *P. falciparum* with ivermectin clearly demonstrate activity at nanomolar concentrations against the blood-stage parasite, supporting a recent study that showed similar results[94]. The mechanism of action of ivermectin against *P. falciparum* has yet to be established, and the assays implemented here provide a method for testing interactions between ivermectin and microtubules that have previously been hypothesized.

Three experimental approaches currently in progress will solidify the mechanistic link between *Pf* microtubule inhibition by oryzalin, APM, and other compounds and their inhibition of parasite growth: visualization of mitotic cells treated with oryzalin, generating resistant mutants, and determining the structure of *Pf* microtubules and inhibitor-bound tubulin through structural techniques such as cryo-EM.

Structural information on *P. falciparum* tubulin will be instrumental in elucidating the mechanisms of binding and microtubule inhibition by oryzalin and other compounds, as well as the structural consequences of resistance mutations. Many resistance mutations that have been identified in *T. gondii* and *T. thermophila* are located in the H1-S2 and M loops, which based on cryo-EM data and comparisons of microtubule dynamics between *C. elegans* and mammalian tubulin are proposed to be important for microtubule dynamics based on how they determine the lateral contacts between protofilaments[74,103]. Thus, it is unclear whether resistance is achieved by a reduced affinity for oryzalin, by compensating for inhibition with mutations that confer increased microtubule stability, or a combination of both.

Spindle length in *Plasmodium* cells is in the range of 1 – 3 μm, much lower than the length of well-characterized spindles such as those of *Xenopus spp.,* making fluorescence-microscopy-based characterization of spindle structure and microtubule dynamics challenging[83]. Blood-stage *Pf* spindle microtubule structures have recently been visualized using expansion microscopy, which may be useful in determining the structural consequences of treating *Pf* spindles with inhibitors such as oryzalin.

The *in vitro* reconstitution of *Pf* and mammalian host microtubules has shown to be instrumental in demonstrating the efficacy and selectivity of oryzalin and APM against *Plasmodium* microtubules. Screening potential parasite-specific inhibitors will require a larger amount of tubulin than was produced over the course of this study, which is an ongoing effort. This study has utilized recently developed technical advances in microtubule research to overcome a key challenge that has limited the impact of previous research on *Plasmodium falciparum* microtubules, namely, a lack of functional purified *P. falciparum* tubulin. The *in vitro* assembly of *P. falciparum* microtubules and their direct and selective inhibition by two different antimitotic herbicides have been demonstrated, establishing a framework for directly testing known and novel parasite-specific inhibitors of a promising drug target in *P falciparum*, as well as for characterizing novel aspects of *Plasmodium* microtubule biology *in vitro.*

Chapter 5. Materials and Methods

5.1 Antibodies

A monoclonal anti-a-tubulin (SIGMA, T5168, Clone B-5-1-2) was used in western blots as a loading control. In addition, we used sheep polyclonal ATN02 also directed against α-tubulin and β-tubulin (Sigma T7816). K40: Acetylated lysine 40 of a-tubulin (Sigma Aldrich T7451 clone 6-11 B-1). Poly-Glu: Polyglutamylation of acidic residues (Adipogen gt335). Tyr: Tyrosinated C terminus of tubulin (Abcam ab6160). Detyr: Tubulin C terminus with tyrosine removed (Abcam ab48389). P-Ser: Phosphorylated serine residues (Abcam ab9332). The anti-XMAP215 antibody was raised against a peptide containing the last 15 amino acids of XMAP215 and affinity purified against this peptide in a previous study (Reber 2013). Secondary antibodies were HRP-conjugated anti-rabbit IgG (Proteintech 0001-2) and anti-mouse IgG (Proteintech 0001-1) from goat.

5.2 Purification of *Xenopus* egg tubulin

Cytostatic factor (CSF) extracts were prepared from *X. laevis* and *X. tropicalis* eggs arrested in metaphase of meiosis II as described previously [34]. Briefly, *X. laevis* frogs were primed with 100 U of pregnant mare serum gonadotrophin (PMSG) 3-7 days before the experiment and were boosted with 1000 U human chorionic gonadotrophin (HCG) to induce egg laying. *X. tropicalis frogs* on the other hand were primed with 10 U of HCG 16-24 hours and boosted with 200 U HCG 5 hours before the experiment to induce egg laying. Eggs arrested in the metaphase stage of meiosis II were collected, dejellied using L-Cysteine and fractionated via centrifugation. The cytoplasmic layer was isolated and supplemented with Cytochalasin D and Complete EDTA-free protease inhibitor. CSF-extract was kept on ice (*X. laevis*) or at room temperature (*X. tropicalis*) and was either used for spindle assembly reactions or for subsequent tubulin purification. Tubulin was purified as described in [29] using a fusion protein of GST and TOG domains 1 and 2 of S. cerevisiae Stu2 (GST-TOG1/2) coupled to a 5 mL HiTrap NHS-activated HP column (GE Healthcare). The extract was first diluted with an equal volume of BRB80 buffer (80 mM PIPES, 1 mM EGTA, 1 mM MgCl2, pH 6.9) and centrifuged at 80,000 rpm in an MLA-80 rotor (Beckman-Coulter) for 10 min at 4°C. The supernatant was cycled through the column at 0.5 column volumes per minute (CV/min) for 20 min. The column

was washed with 8 CV of BRB80 supplemented with 100 mMMg2+ GTP (wash buffer) followed by 3 CV of BRB80 supplemented with 10 mM MgCl2 and 5 mM ATP and incubated for 15 min to induce dissociation of chaperone proteins. The column was then washed with 3 CV BRB80/ATP buffer and 20 CV of wash buffer. Tubulin was eluted at 1 mL/min with wash buffer supplemented with 0.5 M (NH4)2SO4. Peak fractions were determined by measuring A280 values with a NanoDrop spectrophotometer (Thermo), pooled, buffer-exchanged into BRB80 containing 10 mM GTP using PD10 desalting columns (GE Healthcare) and concentrated to at least 30 mM using a concentration filter column with a 30 kDa cut-off (Amicon). Concentrated tubulin was incubated on ice for 30 min to fully depolymerize microtubules, centrifuged for 15 min at 2°C in a TLA-100 rotor at 80,000 rpm, aliquoted into 5 or 10 mL single-use aliquots, and snap-frozen in liquid nitrogen. Tubulin dimer concentration was determined by measuring absorbance at 280 nm with a NanoDrop. Purified tubulin was determined to be free of the major microtubule polymerase XMAP215 and the severing enzyme katanin by Coomassie and western blot (Figure S1B) and free of other known MAPs and motors using mass spectrometry (see Table S1).

5.3 Cycled porcine brain tubulin

Porcine brain tubulin was prepared in a previous study according to (Gell 2011) and stored in 4 mL aliquots at 5.2 mg/mL at -80°. In order to prepare the tubulin for use in dynamic assays or for preparing GMPCPP-stabilized seeds, one or more aliquots were subjected to a polymerization-depolymerization cycle to select for active tubulin and to distribute the protein into smaller working aliquots. Cycling was performed first by rapidly thawing a large aliquot in a 37° water bath and then immediately placing on ice. $MgCl_2$, DTT, and GTP were added to 1 mM each and the solution was incubated on ice for 5 minutes. Pre-warmed (37°) glycerol was added to a final concentration of 33%, mixed gently, and the solution was incubated at 37° for 30 minutes to allow the tubulin to polymerize. The polymerized mixture was then layered on top of an equal volume of pre-warmed 1x BRB80 containing 60% w/v glycerol and then centrifuged at 70,000 rpm in an MLA80 rotor at 35° for 10 minutes.

5.4 Tubulin activity measurements

Tubulin activity was assessed by polymerizing 20 mM tubulin in 1x BRB80 in the presence of 1 mM GTP and 33% v/v glycerol at 35°C for 40 min, layering the reaction on top of an equal volume of 1xBRB80 containing 60% glycerol, and centrifuging in a TLA100 rotor at 35°C for 10 min at 80,000 rpm. Polymerized microtubules form the pellet, whereas non-polymerized tubulin remains in the reaction mixture above the 60% glycerol layer. Relative tubulin abundance in the input, supernatant, and pellet fractions was assessed by SDS-PAGE and western blot analysis.

5.5 Depletion / add-back experiments and pull-down assays

Tubulin was pulled down from CSF-extracts using either Protein G Dynabeads (Invitrogen) coupled to anti-tubulin antibodies (a-tubulin clone b-5-1-2 (Sigma-Aldrich) / sheep polyclonal ATN02) or Pierce Glutathione Magnetic Agarose beads (Thermo Scientific) coupled to the recombinant GST-TOG1/2 protein. Coupling was performed by suspending beads in saturating concentrations of antibody or protein and incubating with gentle agitation at room temperature for 1 hour or overnight at 4°C. Beads were washed with CSF-XB (100 mM KCl, 0.1 mM CaCl2, 2 mM MgCl2, 5 mM EGTA, 50 mM sucrose, 10 mM HEPES, pH 7.7.), one volume of beads corresponding to no more than 10% of the extract volume was used for extract depletion at 4°C for 30 min. The beads were then removed from the extract, washed with CSF-XB, and eluted with either SDS-PAGE loading buffer without DTT (antibody-coupled beads) or TOG column elution buffer (GST-TOG1/2-coupled beads). Fresh beads were added to the extract and this process was repeated for up to 4 rounds of depletion per extract sample. The amount of tubulin pulled down was evaluated by SDS-PAGE stained with Coomassie and by western blot.

5.6 Preparation of GMPCPP-stabilized microtubule seeds

To serve as nucleation templates for *in vitro* microtubule assembly, stabilized microtubule seeds were prepared using GMPCPP, a slowly-hydrolyzing GTP analogue that prevents rapid microtubule depolymerization[104]. Additionally, biotinylated tubulin was incorporated to facilitate adhesion to the surface of neutravidin-functionalized coverslips, and labelled tubulin was used to visualize the seeds. A seed assembly reaction was

prepared on ice by mixing bovine brain tubulin (final concentration 2.8 μM), fluorescently labelled tubulin (final concentration 0.4 μM), biotin-labeled tubulin (final concentration 0.8 μM), $MgCl_2$ (final concentration 2 mM, and GMPCPP (final concentration 1 mM) in 1x BRB80 in a microreaction tube. The reaction was left on ice for 10 minutes to allow for nucleotide exchange, and then transferred to a ThermoMixer (Eppendorf) and incubated at 37° for 2 hours. The reaction was then removed from the incubator and microtubules were gently resuspended by flicking the tube. Using a 200 μL pipette with cut-off tip to avoid shearing, the suspension was gently layered over 100 μL of a pre-warmed (37°) BRB80 solution supplemented with 60% v/v glycerol and 0.5 mM GMPCPP in a 230 μL thick-walled centrifuge tube (Beckman-Coulter). Care was taken to maintain the two distinct liquid phases. The reaction was centrifuged in a pre-warmed (37°) TLA-100 rotor at 220000 xg for 10 minutes at 35°. The top layer was removed, and the cushion interface was washed with warm BRB80, after which the cushion was removed, and the pellet was gently washed twice with warm BRB80. Finally, the pellet was resuspended in warm BRB80 supplemented with 1 mM DTT using a cut-off pipette tip, separated into 5 μL working aliquots, and flash-frozen in liquid nitrogen.

5.7 TIRF assays, image acquisition, and data processing

Flow chambers were constructed with glass coverslips passivated with dichlorodimethylsilane [42] or trimethylchlorosilane [105] mounted onto glass slides using thin strips of parafilm. Chambers were functionalized by perfusing 20 μL of 100 mg/mL Neutravidin in BRB80 through the chamber and incubating for 5 min at room temperature. The chamber was rinsed twice with 20 μL BRB80, twice with a blocking buffer consisting of 1% w/v Pluronic F-127 (Sigma-Aldrich) in BRB80, and incubated at room temperature for 15 min. Wash buffer containing 1 mg/mL K-casein in BRB80 was flowed through the chamber followed by 2 x 20 μL of GMPCPP-stabilized microtubule seeds containing 10% Cy5-labeled and 20% biotin-labeled tubulin suspended in wash buffer.

Polymerization reactions were carried out at 37°C in BRB80 buffer supplemented with 1 mg/mL k-casein, 1% β-mercaptoethanol, 2 mM Trolox, 2.5 mM PCA, 25 nM PCD, and 0.15% methylcellulose at different concentrations of purified tubulin with 10% Cy3- or Atto488-labeled porcine brain tubulin. Assays using *P. falciparum* tubulin also included

5% w/v glycerol to promote microtubule growth. 50 µL of reaction solution were perfused through the chamber, then both ends were sealed with silicone grease. The slide was mounted on the objective and left for 10 min to allow the temperature to equilibrate before imaging with the exception of 9 mM reactions, which were imaged immediately in order to determine when steady state was reached (see Figure 2.10).

To measure microtubule dynamics in extract, BRB80 was replaced with CSF-XB and reactions were carried out at room temperature. Flow chambers were prepared as with the purified tubulin reactions, except the seed binding and final wash steps used CSF-XB supplemented with 10% sucrose. Reactions contained 5 µL of egg extract, 0.5 mM vanadate, 0.5 mM Cy5-labeled tubulin, 0.15% methylcellulose, and were diluted in CSF-XB supplemented with 10% sucrose to a final volume of 20 µL.

Images were taken on an inverted Nikon Eclipse Ti-E microscope with a motorized TIRF angle, a Nikon Plan Apochromat 100x/1.49NA oil immersion objective lens, and an Andor iXon Ultra X3 987 EMCCD camera or a Photometrics Prime 95B sCMOS camera. Atto488-labeled microtubules were imaged with a 488 nm laser, Cy3-labeled microtubules were imaged with a 561 nm laser and Cy5-labeled microtubule seeds were imaged with a 647 nm laser. Time-lapse images were taken at a frame rate of 0.2 fps with an exposure time of 500 or 700 ms. To measure microtubule dynamics in extract, images were acquired at 1 fps with an exposure time of 200 ms. Recording was controlled with the Nikon ND Acquisition software.

Microtubule dynamics were measured by producing kymographs using the Multi Kymograph function of the FIJI image analysis software [106] and manually fitting lines to growth and shrinkage events according to [107]. Growth and shrinkage velocities were calculated from the slopes of the fitted lines. Catastrophe frequencies were calculated as the inverse of the mean of microtubule lifetimes, with the exception of *X. laevis* microtubules, where the catastrophe frequency was estimated as the total number of observed catastrophes divided by the total measured time microtubules spent in the growth phase. Rescue frequencies were calculated as the inverse of the mean duration of depolymerization events; events without a rescue were assigned a value of 0. Microtubule lengths were measured in still frames of individual timepoints in FIJI by fitting a segmented line from the point of nucleation to the plus end of dynamic microtubules.

Microtubule masses were calculated assuming 1625 tubulin dimers per µm microtubule[45].

5.8 *Plasmodium falciparum* cell culture

The chloroquine (CQ)-resistant 3D7 wild-type strain of *P. falciparum* was used for all cell culture and purification of *Pf* tubulin. Parasites were cultured in RPMI supplemented with 3 mM L-glutamine, 25 mM HEPES, 20 mM glucose, 24 µg/mL gentamycin, 200 µM hypoxanthine, and 0.6% AlbuMAX II bovine serum albumen (Gibco). Routine cultures were maintained at 3 – 4% haematocrit in a 37° incubator with a gas mixture of 1% CO_2, 3% O_2, and 96% N_2 with a shaking platform. Parasitaemia was monitored every 48 – 72 hours by Giemsa stain and cultures were split when the parasitaemia reached 1 – 10%.

5.9 Sorbitol synchronization of *P. falciparum* cultures

Cultures with >1% ring-stage parasitaemia were centrifuged at 500 x g for 5 minutes at room temperature and the supernatant was discarded. Pellets were resuspended in 10 pellet volumes of pre-warmed (37°) 5% w/v sorbitol and incubated at 37° for 15 minutes. The cell suspension was centrifuged again for 5 minutes at 500 x g at room temperature, the supernatant was discarded, and the pellet was resuspended in complete RPMI to the desired haematocrit to continue culturing.

5.10 Purification of *P.falciparum* tubulin

To purify tubulin from *P. falciparum,* parasite cells were first isolated from host red blood cells by saponin lysis. Synchronized cultures at >5% parasitaemia were pelleted at 500 x g at 4° in a Beckmann 5810 R centrifuge and the supernatant was discarded. The pellet was resuspended on ice in an equal volume of saponin lysis buffer and incubated on ice for 5 minutes with occasional inversion of the tube. The pellet was centrifuged for 5 minutes at 500 x g at 4°, the supernatant was discarded, and the pellet was resuspended in a volume of PBS equivalent to the total original saponin lysis suspension. The pellet was again centrifuged and the PBS wash was repeated twice. Finally, the pellet was resuspended in a minimal volume of PBS (1 mL or less), flash

frozen, and stored at -80°. On the day of tubulin purification, aliquots were quickly thawed, pooled, resuspended in BRB80, and supplemented with 100 µM GTP, 2 mM DTT, and 1x protease inhibitors. Cells were sonicated at full power at 0.5 second intervals totalling 30 seconds with a sonicator probe (Sonorex GM 2070) and then centrifuged for 10 minutes at 80,000 rpm at 4° in an MLA-80 rotor. The supernatant was loaded onto an equilibrated TOG affinity column and tubulin purification proceeded as detailed in Section 5.2 of Materials and Methods (see previous).

One large-scale *Pf* tubulin preparation was performed using a total of 120 mL of frozen infected red blood cell (iRBC) pellets pooled from a 60 mL pellet provided by the laboratory of Jacob Baum of the Imperial College London and pellets collected over several weeks in-house by Ylva Veith of the Matuschewski lab. In order to avoid tubulin loss by cell lysis during thawing, the whole iRBC pellet was resuspended in an equal volume of BRB80 with GTP, DTT, and protease inhibitors and sonicated as described above. The lysate was centrifuged for 45 minutes at 45,000 rpm at 4° in a 50.2 Ti rotor (Beckman-Coulter), and the supernatant was loaded onto the column by cycling for a full hour before proceeding with the next steps of tubulin purification.

5.11 Dose-response assays

Synchronous blood-stage shaking cultures between 1% and 7% parasitaemia were used for dose-response assays. A 10 mL aliquot of culture suspension was removed from the culture flask and the iRBCs were washed by centrifuging at 500 x g for five minutes, removing the supernatant, resuspending the pellet in CCM, and incubating for 1 hour in a 37°C water bath. In parallel, 2 mL of fresh uRBCs were washed by adding the cells to 10 mL CCM and incubating at 37°C for 1 hour. Tubes containing cell suspensions were inverted every 15 – 20 min to keep the cells suspended.

While the cells were incubating during the wash, medium containing the inhibitor of interest was prepared by diluting the inhibitor stock in CCM and sterile filtering with a syringe attached to a 0.2 µM syringe filter. The working solution inhibitor concentration was 2x the highest concentration tested during the assay. The volume of CCM used corresponded to the number of rows of the 96-well culture plate used for each inhibitor; generally, 1.6 mL of medium was prepared each time, corresponding to 200 µL per row for 3 technical replicates plus 1 mL extra in case any solution was lost during filtering.

Additionally, CCM containing 1 mM CQ was prepared as a positive control in the same manner to a final volume of 1 mL per plate.

Dose-response assays were carried out in 96-well culture plates with the rows labelled A – H and the columns labelled 1 – 12. Only rows B – G and columns 2 – 11 contained samples; all peripheral wells contained 200 µL RPMI to prevent evaporation from experimentally important wells. To prepare the wells for cell culture, 100 µL of CQ working solution were added to the remaining wells of column 2, 200 µL of each inhibitor working solution were added to column 4, and 100 µL of CCM were added to the remaining wells. The inhibitor solution of column 4 was then serially diluted at a ratio of 1:2 from column 4 to column 11, leaving a volume of 100 µL in each well.

To prepare the working iRBC cell suspension, the iRBC and uRBC suspensions were removed from the water bath, centrifuged at RT for 5 min at 500 xg, and the supernatant was discarded. iRBCs and uRBCs were resuspended in CCM at an appropriate ratio to achieve 2% hematocrit at 0.5% parasitaemia. 100 µL of the cell suspension were added to each well to achieve a final culture volume of 200 µL at 1% hematocrit. Finally, plates were incubated in sealed humidified chambers with 3% oxygen and 1% CO_2 and incubated at 37°C without shaking for 96h.

Parasite growth was quantified by measuring the quantity of DNA using the DNA dye SYBR Safe. At the end of 96 hours, cell cultures were resuspended in their wells, transferred to a new 96-well plate, and mixed with a lysis buffer (20 mM TRIS, 5 mM EDTA, 0.008% w/v saponin, 0.08% v/v Triton X-100, pH 7.5) containing 0.02% v/v SYBR Safe dye. Fluorescence at the 490 nm excitation and 520 nm emission wavelengths was measured using a FLUOstar OPTIMA plate reader (BMG Labtech). The signals were normalized to a scale of 0 – 100% based on the mean signals of the CQ-treated (0%) and untreated (100%) wells.

5.12 Intact protein mass spectrometry

The isolated tubulins were analyzed using reverse-phase liquid chromatography–mass spectrometry (LC–MS). To analyze the purified tubulin via LC–MS, 2 µL of 5 mM tubulin were mixed with 10 ml of 0.1% trifluoroacetic acid (TFA) and centrifuged at 16,000 x g for 10 min at 4°C. The sample was loaded onto a Zorbax 300SB-C18 column (50 mm x 2.1 mm) (Agilent) attached in-line with an Agilent 6224 electrospray ionization time-

of-flight LC–MS. A 0%–70% acetonitrile gradient in 0.05% TFA at a 0.2 ml/min flow rate was used. The data were analyzed using the Agilent Mass Hunter Workstation platform[108]. Intact protein mass spectrometry was carried out by Kishore K. Mahalingan at the Cell Biology and Biophysics Unit, NINDS, National Institutes of Health, Bethesda, MD, USA.

5.13 Trypsin-digest fingerprint mass spectrometry

Tubulin sample purity was evaluated by LC-MS/MS analysis of in-solution tryptic digests of purified tubulin aliquots. Digested samples were reconstituted in 20 µL of 0.05% TFA, 2% acetonitrile, 2 µL were analyzed by a reversed-phase nano liquid chromatography system (Ultimate 3000, Thermo Scientific) connected to an Orbitrap Velos mass spectrometer (Thermo Scientific). Samples were injected and concentrated on a trap column (PepMap100 C18, 3 mm, 100 A˚ ,75 mm i.d. x 2 cm, Thermo Scientific) equilibrated with 0.05% TFA, 2% acetonitrile in water. After switching the trap column inline, LC separations were performed on a capillary column (Acclaim PepMap100 C18, 2 mm, 100 A˚ ,75 mm i.d. x 25 cm, Thermo Scientific) at an eluent flow rate of 300 nL/min. Mobile phase A contained 0.1% formic acid in water, and mobile phase B contained 0.1% formic acid in acetonitrile. The column was pre-equilibrated with 3% mobile phase B followed by an increase of 3%–50% mobile phase B in 50 min. Mass spectra were acquired in a data-dependent mode using a single MS survey scan (m/z 350–1500) with a resolution of 60,000 in the Orbitrap, and MS/MS scans of the 20 most intense precursor ions in the linear trap quadrupole. The dynamic exclusion time was set to 60 s and automatic gain control was set to 1 x 106 and 5,000 for Orbitrap-MS and LTQ-MS/MS scans, respectively. Data processing and identification of proteins was performed using the Mascot Daemon software (version 2.5.0, Matrix Science). Processed spectra were used to search against the *X. laevis* protein database downloaded from Uniprot (Proteome ID UP000186698; last modified December 1, 2019) and the *P. falciparum* protein database (Proteome ID UP000001450). A maximum of three missed cleavages was allowed and the mass tolerance of precursor and sequence ions was set to 15 ppm and 0.35 Da, respectively. Methionine oxidation and acetylation (protein N terminus) were used as variable modifications and carbamidomethylation of cysteine residues was used as fixed modification. Only peptides with Mascot scores

greater than the homology threshold were considered and a significance threshold of 0.05 was used based on decoy database searches. In addition, a peptide ion score cut-off of 20 was applied and only proteins with at least two significant sequences are reported in the output tables. Tryptic digest LC-MS/MS was carried out by Benno Kuropka and Chris Weise from the Core Facility BioSupraMol of the Freie Universität Berlin.

5.14 Experimental model and subject details

The *Xenopus* frogs (adult females) used in this study are part of the Xenopus colony maintained at the animal husbandry of the Humboldt-Universität zu Berlin. Mature *X. laevis* and *X. tropicalis* frogs were obtained from NASCO (Fort Atkinson, WI). *Xenopus* frogs were maintained in a recirculating tank system with regularly monitored temperature and water quality (pH, conductivity, and nitrate/nitrite levels). *X. laevis* were housed at a temperature of 18-20°C and *X. tropicalis* housed at 23-26°C. Frogs were fed with food pellets (V7106-0202) from ssniff Spezialdiäten GmbH. All experimental protocols involving frogs were performed in accordance with national regulatory standards and ethical rules and reviewed and approved by the LaGeSo under Reg.-Nr. 0096/15.

5.15 Reagents and Resources

Reagent or Resource	Source	Identifier
Chemicals, Peptides, and Recombinant Proteins		
Complete EDTA-free Protease Inhibitor Tablets	Roche	Cat#: 4693132001
Pregnant mare serum gonadotrophin	MSD, Tiergesundheit	Intergonan ® 240 IU/ml
Human chorionic gonadotrophin	SIGMA	Cat#: CG-10
Cytochalasin D	SIGMA	Cat#: C8273
Cycled bovine brain tubulin	PurSolutions	Cat#: 032005
Porcine brain tubulin	[8]	N/A
Xenopus laevis egg tubulin	This study	N/A
Xenopus tropicalis egg tubulin	This study	N/A
Plasmodium falciparum tubulin	This study	N/A
HEK293 tubulin	This study	N/A
Bradford reagent	SIGMA	Cat#: B6916
Bacteriophage lambda phosphatase	Sigma-Aldrich	Cat#: P9614
Human PP2A-α/PP2AR complex	BPS Bioscience	Cat#: 30056
FastAP Thermosensitive Alkaline Phosphatase	ThermoFisher	Cat#: EF0651
Pluronic F-127	Sigma-Aldrich	Cat #: P2443
NeutrAvidin Protein	Thermo-Fisher	Cat #: 31000
κ-Casein from bovine milk	Sigma-Aldrich	Cat #: C0406
Dichlorodimethylsilane (DDS)	Sigma-Aldrich	Cat #: 440272
GMPCPP	Jena Bioscience	Cat #: NU-405L
Protocatechuic Acid (PCA)	Sigma-Aldrich	Cat #: 03930590
Protocatechuate-3,4-dioxygenase (PCD)	Sigma-Aldrich	Cat #: P8279
Trolox	Sigma-Aldrich	Cat #: 238813
Cy3 Mono NHS Ester	GE Healthcare	Cat #: PA13101
Cy5 Mono NHS Ester	GE Healthcare	Cat #: PA15101
Atto-488 NHS Ester	Atto-Tec	Cat #: AD 488-35
Oryzalin	Sigma-Aldrich	Cat #: 36182
Amiprofos-Methyl	Sigma-Aldrich	Cat #: 03992
Albendazole	Sigma-Aldrich	Cat #: A4673
Fenbendazole	Sigma-Aldrich	Cat #: F5396
Azadirachtin	Sigma-Aldrich	Cat #: A7430
Ivermectin	Sigma-Aldrich	Cat #: I8898
RPMI 1640	PAN Biotech	Cat #: P04-18050
Gentamicin	Gibco	Cat #: 15750-060
Hypoxanthin	c.c.pro	Cat #: Z-41-M
SYBR Green Stain	Sigma	Cat #: S7563
Sorbitol	Sigma	Cat #: S1876

Reagent or Resource	Source	Identifier
Commercial Assays		
TOG columns	[29]	
PD10 desalting columns	GE Healthcare	Cat#: 17085101
Amicon®Ultra Centrifugal filters	Merck	Cat#: UFC8030
Protein G Dynabeads	Invitrogen	Cat#: 10009D
Pierce Glutathione Magnetic Agarose beads	Thermo Fisher	Cat#: 78601
Animal Model Organisms		
Xenopus laevis	Nasco	Cat#: LM00535
Xenopus tropicalis	Nasco	Cat#: LM00822
Software and Algorithms		
NIS-Elements Advanced Research	Nikon	https://www.microscope.healthcare.nikon.com/en_EU/products/software/nis-elements/nis-elements-advanced-research
FIJI	[34]	https://imagej.net/Fiji/Downloads
Cytosim	[30]	https://github.com/nedelec/cytosim
Prism version 8.0 for Mac OS X	GraphPad	https://www.graphpad.com/

5.16 Buffers and Media

1x BRB80

- 80 mM PIPES
- 1 mM EGTA
- 1 mM $MgCl_2$
- pH to 6.9 using KOH

TOG Wash Buffer

- 1x BRB80
- 100 µM GTP

TOG ATP Wash Buffer

- 1x BRB80
- 100 µM GTP
- 10 mM $MgCl_2$
- 5 mM Mg^{2+}ATP

TOG Elution Buffer

- 1x BRB80
- 100 µM GTP

TOG Desalting Buffer

- 1x BRB80
- 10 µM GTP

RPMI Complete Culture Media

- 500 mL RPMI (w/ stable Glutamine, 25 mM HEPES, 2.0 g/L $NaHCO_3$)
- 20 mM Glucose
- 24 µg/mL Gentamycin
- 200 µM Hypoxanthine
- 0.6% w/v Albumax II

SYBR Safe Lysis Buffer

- 1x BRB80
- 10 µM GTP

10x MMR

- 1M NaCl
- 20 mM KCl
- 10 mM $MgCl_2$
- 20 mM $CaCl_2$
- 1 mM EDTA
- 50 mM HEPES pH 7.8

20x XB-Salts

- 2M KCl
- 20 mM $MgCl_2$
- 2 mM $CaCl_2$

CSF-XB

- 10 mM HEPES
- 50 mM Sucrose
- 1x XB-Salts
- 5 mM EGTA
- pH to 7.7 with KOH

- 20 mM TRIS
- 5 mM EDTA
- 0.008% Saponin (w/v)
- 0.08% Triton X100 (v/v)
- pH = 7.5

Saponin Lysis Buffer

- 1x PBS
- 0.15% w/v Saponin

References

1. Mitchison, T. & Kirschner, M. Dynamic instability of microtubule growth. *Nature* **312**, 237–242 (1984).
2. Walker, R. A. *et al.* Dynamic Instability of Individual Microtubules. *J. Cell Biol.* **107**, 1437–1448 (1988).
3. Nogales E., Wolf S.G. & Downing K.H. Structureof the a-b tubulin dimer by electron crystallography. *Nature* **6**, 786–787 (1998).
4. Alushin, G. M. *et al.* High-Resolution microtubule structures reveal the structural transitions in αβ-tubulin upon GTP hydrolysis. *Cell* **157**, 1117–1129 (2014).
5. Dimitrov, A. *et al.* Detection of GTP-tubulin conformation in vivo reveals a role for GTP remnants in microtubule rescues. *Science* **322**, 1353–1356 (2008).
6. Vemu, A. *et al.* Severing enzymes amplify microtubule arrays through lattice GTP-tubulin incorporation. *Science (80-.).* **361**, eaau1504 (2018).
7. Needleman, D. J. *et al.* Fast Microtubule Dynamics in Meiotic Spindles Measured by Single Molecule Imaging: Evidence That the Spindle Environment Does Not Stabilize Microtubules. *Mol. Biol. Cell* **21**, 323–333 (2010).
8. Reber, S. B. *et al.* XMAP215 activity sets spindle length by controlling the total mass of spindle microtubules. *Nat. Cell Biol.* **15**, 1116–22 (2013).
9. Edson, K. J., Lim, S. -S, Borisy, G. G. & Letourneau, P. C. FRAP analysis of the stability of the microtubule population along the neurites of chick sensory neurons. *Cell Motil. Cytoskeleton* **25**, 59–72 (1993).
10. Sawin, K. E. & Mitchison, T. J. Poleward microtubule flux in mitotic spindles assembled in vitro. *J. Cell Biol.* **112**, 941–954 (1991).
11. Rusan, N. M., Fagerstrom, C. J., Yvon, A. M. C. & Wadsworth, P. Cell cycle-dependent changes in microtubule dynamics in living cells expressing green fluorescent protein-α tubulin. *Mol. Biol. Cell* **12**, 971–980 (2001).
12. Piehl, M. & Cassimeris, L. Organization and Dynamics of Growing Microtubule Plus Ends during Early Mitosis. *Mol. Biol. Cell* **14**, 916–925 (2003).
13. Pearson, C. G. *et al.* Measuring Nanometer Scale Gradients in Spindle Microtubule Dynamics Using Model Convolution Microscopy. *Mol. Biol. Cell* **17**, 4069–4079 (2006).
14. Janke, C. & Magiera, M. M. The tubulin code and its role in controlling

microtubule properties and functions. *Nature Reviews Molecular Cell Biology* **21**, 307–326 (2020).

15. Roll-Mecak, A. The Tubulin Code in Microtubule Dynamics and Information Encoding. *Dev. Cell* **54**, 7–20 (2020).
16. Roll-Mecak, A. How cells exploit tubulin diversity to build functional cellular microtubule mosaics. *Current Opinion in Cell Biology* **56**, 102–108 (2019).
17. Valenstein, M. L. & Roll-Mecak, A. Graded Control of Microtubule Severing by Tubulin Glutamylation. *Cell* **164**, 911–921 (2016).
18. Kuo, Y., Trottier, O., Mahamdeh, M. & Howard, J. Spastin is a dual-function enzyme that severs microtubules and promotes their regrowth to increase the number and mass of microtubules. **116**, (2019).
19. Portran, D., Schaedel, L., Xu, Z., Théry, M. & Nachury, M. V. Tubulin acetylation protects long-lived microtubules against mechanical ageing. *Nat. Cell Biol.* **19**, 391–398 (2017).
20. Xu, Z., Schaedel, L., Portran, D., Aguilar, A. & Gaillard, J. Microtubules acquire resistance from mechanical breakage through intralumenal acetylation. **000**, 1–5 (2017).
21. Joseph M. Varberg, a Leah R. Padgett, a Gustavo Arrizabalaga, a, b William J. Sullivan, J. TgATAT-Mediated-Tubulin Acetylation Is Required for Division of the Protozoan Parasite Toxoplasma gondii. *mSpere* **1**, 1–16 (2016).
22. Roach, M. C., Boucher, V. L., Walss, C., Ravdin, P. M. & Ludueña, R. F. Preparation of a monoclonal antibody specific for the class I isotype of??-tubulin: The?? isotypes of tubulin differ in their cellular distributions within human tissues. *Cell Motil. Cytoskeleton* **39**, 273–285 (1998).
23. Leandro-García, L. J. *et al.* Tumoral and tissue-specific expression of the major human β-tubulin isotypes. *Cytoskeleton* **67**, 214–223 (2010).
24. Vemu, A., Atherton, J., Spector, J. O., Moores, C. A. & Roll-Mecak, A. Tubulin isoform composition tunes microtubule dynamics. *Mol. Biol. Cell* mbc.E17-02-0124 (2017). doi:10.1091/mbc.E17-02-0124
25. Bittermann, E. *et al.* Differential requirements of tubulin genes in mammalian forebrain development. *PLoS Genet.* **15**, 1–28 (2019).
26. Spreng, B. *et al.* Microtubule number and length determine cellular shape and

function in Plasmodium . *EMBO J.* e100984 (2019). doi:10.15252/embj.2018100984

27. Gell, C. *et al.* Purification of tubulin from porcine brain. *Methods Mol. Biol.* **777**, 15–28 (2011).
28. Weingarten, M. D., Suter, M. M., Littman, D. R. & Kirschner, M. W. Properties of the Depolymerization Products of Microtubules from Mammalian Brain. *Biochemistry* **13**, 5529–5537 (1974).
29. Widlund, P. O. *et al.* One-step purification of assembly-competent tubulin from diverse eukaryotic sources. *Mol. Biol. Cell* **23**, 4393–401 (2012).
30. Chaaban, S. *et al.* The Structure and Dynamics of C. elegans Tubulin Reveals the Mechanistic Basis of Microtubule Growth. *Dev. Cell* **47**, 191-204.e8 (2018).
31. Roostalu, J. *et al.* The speed of GTP hydrolysis determines GTP cap size and controls microtubule stability. *Elife* **9**, 1–22 (2020).
32. Wühr, M. *et al.* Evidence for an Upper Limit to Mitotic Spindle Length. *Curr. Biol.* **18**, 1256–1261 (2008).
33. Brouhard, G. J. *et al.* XMAP215 Is a Processive Microtubule Polymerase. *Cell* **132**, 79–88 (2008).
34. Brown, K. S. *et al.* Xenopus tropicalis egg extracts provide insight into scaling of the mitotic spindle. *J. Cell Biol.* **176**, 765–770 (2007).
35. Hazel, J. *et al.* Changes in cytoplasmic volume are sufficient to drive spindle scaling. *Science* **342**, 853–6 (2013).
36. Helmke, K. J. & Heald, R. TPX2 levels modulate meiotic spindle size and architecture in Xenopus egg extracts. *J. Cell Biol.* **206**, 385–393 (2014).
37. Loughlin, R., Wilbur, J. D., McNally, F. J., Nédélec, F. J. & Heald, R. Katanin contributes to interspecies spindle length scaling in Xenopus. *Cell* **147**, 1397–1407 (2011).
38. Chaaban, S. *et al.* The Structure and Dynamics of C . elegans Tubulin Reveals the Mechanistic Basis of Microtubule The Structure and Dynamics of C . elegans Tubulin Reveals the Mechanistic Basis of Microtubule Growth. 1–14 (2018). doi:10.1016/j.devcel.2018.08.023
39. Hotta, T. *et al.* Affinity purification and characterization of functional tubulin from cell suspension cultures of Arabidopsis and tobacco. *Plant Physiol.* **170**,

pp.01173.2015 (2016).

40. Lacroix, B. *et al.* Microtubule Dynamics Scale with Cell Size to Set Spindle Length and Assembly Timing. *Dev. Cell* **45**, 496-511.e6 (2018).
41. Milunovic-Jevtic, A., Jevtic, P., Levy, D. L. & Gatlin, J. C. In vivo mitotic spindle scaling can be modulated by changing the levels of a single protein: the microtubule polymerase XMAP215. *Mol. Biol. Cell* **29**, 1311–1317 (2018).
42. Gell, C. *et al.* Microtubule dynamics reconstituted in vitro and imaged by single-molecule fluorescence microscopy. *Methods Cell Biol.* **95**, 221–245 (2010).
43. Khan, I. A. & Ludueña, R. F. Phosphorylation of βIII-tubulin. *Biochemistry* **35**, 3704–3711 (1996).
44. Wieczorek, M., Bechstedt, S., Chaaban, S. & Brouhard, G. J. Microtubule-associated proteins control the kinetics of microtubule nucleation. *Nat. Cell Biol.* **17**, 907–918 (2015).
45. Waterman-Storer, C. M. & Salmon, E. D. How microtubules get fluorescent speckles. *Biophys. J.* **75**, 2059–2069 (1998).
46. Good, M. C., Vahey, M. D., Skandarajah, A., Fletcher, D. A. & Heald, R. Cytoplasmic volume modulates spindle size during embryogenesis. *Science (80-.).* **342**, 856–860 (2013).
47. Loughlin, R., Wilbur, J. D., McNally, F. J., Nédélec, F. J. & Heald, R. Katanin contributes to interspecies spindle length scaling in xenopus. *Cell* **147**, 1397–1407 (2011).
48. Loughlin, R. & Heald, R. A computational model predicts. **191**, 1239–1249 (2010).
49. Lacroix, B. *et al.* Microtubule Dynamics Scale with Cell Size to Set Spindle Length and Assembly Timing. *Dev. Cell* **45**, 496-511.e6 (2018).
50. Wühr, M. *et al.* Deep proteomics of the xenopus laevis egg using an mRNA-derived reference database. *Curr. Biol.* **24**, 1467–1475 (2014).
51. Gard, D. L. & Kirschner, M. W. Microtubule assembly in cytoplasmic extracts of Xenopus oocytes and eggs. *J. Cell Biol.* **105**, 2091–2201 (1987).
52. Pamula, M. C., Ti, S. C. & Kapoor, T. M. The structured core of human β tubulin confers isotype-specific polymerization properties. *J. Cell Biol.* **213**, 425–433 (2016).

53. Janke, C. & Chloë Bulinski, J. Post-translational regulation of the microtubule cytoskeleton: mechanisms and functions. *Nat. Rev. Mol. Cell Biol.* **12**, 773–786 (2011).
54. Fukushima, N., Furuta, D., Hidaka, Y., Moriyama, R. & Tsujiuchi, T. Post-translational modifications of tubulin in the nervous system. *J. Neurochem.* **109**, 683–693 (2009).
55. Maier, A. G., Matuschewski, K., Zhang, M. & Rug, M. Plasmodium falciparum. *Trends Parasitol.* **xx**, 10–11 (2018).
56. Wright, G. J. & Rayner, J. C. Plasmodium falciparum Erythrocyte Invasion: Combining Function with Immune Evasion. *PLoS Pathog.* **10**, 1–7 (2014).
57. Le Roch, K. G. *et al.* Discovery of gene function by expression profiling of the malaria parasite life cycle. *Science (80-.).* **301**, 1503–1508 (2003).
58. De Niz, M. *et al.* Progress in imaging methods: insights gained into Plasmodium biology. *Nat. Rev. Microbiol.* **15**, 37–54 (2016).
59. Kudryashev, M. *et al.* Structural basis for chirality and directional motility of Plasmodium sporozoites. *Cell. Microbiol.* **14**, 1757–1768 (2012).
60. Cyrklaff, M. *et al.* Cryoelectron tomography reveals periodic material at the inner side of subpellicular microtubules in apicomplexan parasites. *J. Exp. Med.* **204**, 1281–7 (2007).
61. Gerald, N., Mahajan, B. & Kumar, S. Mitosis in the human malaria parasite plasmodium falciparum. *Eukaryot. Cell* **10**, 474–482 (2011).
62. Fowler, R. E., Fookes, R. E., Lavin, F., Bannister, L. H. & Mitchell, G. H. Microtubules in Plasmodium falciparum merozoites and their importance for invasion of erythrocytes. *Parasitology* **117 (Pt 5**, 425–433 (1998).
63. Kappes, B. & Rohrbach, P. Microtubule inhibitors as a potential treatment for malaria. *Futur. Microbiol* **2**, 409–423 (2007).
64. Zeeshan, M. *et al.* Plasmodium Kinesin-8X associates with mitotic spindles and is essential for oocyst development during parasite proliferation and transmission. *bioRxiv* 665836 (2019). doi:10.1101/665836
65. Zeeshan, M. *et al.* Kinesin-8B controls basal body function and flagellum formation and is key to malaria transmission. *Life Sci. Alliance* **2**, e201900488 (2019).

66. Fowler, R. E. *et al.* Microtubule associated motor proteins of Plasmodium falciparum merozoites. *Mol. Biochem. Parasitol.* **117**, 187–200 (2001).
67. Fennell, B. *et al.* Microtubules as antiparasitic drug targets. *Expert Opin. Drug Discov.* **3**, 501–518 (2008).
68. Chatterji, B. P., Jindal, B., Srivastava, S. & Panda, D. Microtubules as antifungal and antiparasitic drug targets. *Expert Opin. Ther. Pat.* **21**, 167–186 (2011).
69. Jordan, M. A. & Wilson, L. Microtubules as a target for anticancer drugs. *Nat. Rev. Cancer* **4**, 253–65 (2004).
70. Little, M. *et al.* TUBULIN SEQUENCE CONSERVATION * Introduction The elaborate structure of microtubules and their participation in diverse cellular processes suggests the presence of a large number of binding sites on the tubulin mole- cule . For example , a minimum of two . **14**, (1981).
71. Murthy, J. V., Kim Hyong Ha, Hanesworth, V. R., Hugdahl, J. D. & Morejohn, L. C. Competitive inhibition of high-affinity oryzalin binding to plant tubulin by the phosphoric amide herbicide amiprophos-methyl. *Plant Physiol.* **105**, 309–320 (1994).
72. Fennell, B. J., Naughton, J. A., Dempsey, E. & Bell, A. Cellular and molecular actions of dinitroaniline and phosphorothioamidate herbicides on Plasmodium falciparum: Tubulin as a specific antimalarial target. *Mol. Biochem. Parasitol.* **145**, 226–238 (2006).
73. Morrissette, N. S., Mitra, A., Sept, D. & Sibley, L. D. Dinitroanilines Bind α-Tubulin to Disrupt Microtubules. *Mol. Biol. Cell* **15**, 1960–1968 (2004).
74. Lyons-Abbott, S. *et al.* A-Tubulin Mutations Alter Oryzalin Affinity and Microtubule Assembly Properties To Confer Dinitroaniline Resistance. *Eukaryot. Cell* **9**, 1825–1834 (2010).
75. Dempsey, E. *et al.* Antimitotic herbicides bind to an unidentified site on malarial parasite tubulin and block development of liver-stage Plasmodium parasites. *Mol. Biochem. Parasitol.* **188**, 116–127 (2013).
76. Ashraf, S., Beech, R. N., Hancock, M. A. & Prichard, R. K. Ivermectin binds to Haemonchus contortus tubulins and promotes stability of microtubules. *Int. J. Parasitol.* **45**, 647–654 (2015).
77. Maier, A. G. & Rug, M. In Vitro Culturing Plasmodium falciparum Erythrocytic

Stages. **923**, 3–15 (2012).

78. Bryk, A. H. & Wiśniewski, J. R. Quantitative Analysis of Human Red Blood Cell Proteome. *J. Proteome Res.* **16**, 2752–2761 (2017).
79. Nigra, A. D., Casale, C. H. & Santander, V. S. Human erythrocytes: cytoskeleton and its origin. *Cell. Mol. Life Sci.* **77**, 1681–1694 (2020).
80. Delves, C. J. *et al.* Cloning of a β-tubulin gene from Plasmodium falciparum. *Mol. Microbiol.* **3**, 1511–1519 (1989).
81. Holloway, S. P., Sims, P. F. G., Delves, C. J., Scaife, J. G. & Hyde, J. E. Isolation of α-tubulin genes from the human malaria parasite, Plasmodium falciparum: sequence analysis of α-tubulin. *Mol. Microbiol.* **3**, 1501–1510 (1989).
82. Holloway, S. P. *et al.* The tubulin genes of the human malaria parasite Plasmodium falciparum, their chromosomal location and sequence analysis of the α-tubulin II gene. *Mol. Biochem. Parasitol.* **43**, 257–270 (1990).
83. Fennell, B. J., Al-shatr, Z. a. & Bell, a. Isotype expression, post-translational modification and stage-dependent production of tubulins in erythrocytic Plasmodium falciparum. *Int. J. Parasitol.* **38**, 527–539 (2008).
84. Rawlings, D. J. *et al.* α-Tubulin II is a male-specific protein in Plasmodium falciparum. *Mol. Biochem. Parasitol.* **56**, 239–250 (1992).
85. Bannister, L. H. *et al.* Plasmodium falciparum apical membrane antigen 1 (PfAMA-1) is translocated within micronemes along subpellicular microtubules during merozoite development. *J. Cell Sci.* **116**, 3825–3834 (2003).
86. Dogra, N., Kumar, A. & Mukhopadhyay, T. Fenbendazole acts as a moderate microtubule destabilizing agent and causes cancer cell death by modulating multiple cellular pathways. *Sci. Rep.* **8**, 1–15 (2018).
87. Gupta, K. *et al.* Antimitotic antifungal compound benomyl inhibits brain microtubule polymerization and dynamics and cancer cell proliferation at mitosis, by binding to a novel site in tubulin. *Biochemistry* **43**, 6645–6655 (2004).
88. Aguayo-Ortiz, R. *et al.* Molecular basis for benzimidazole resistance from a novel β-tubulin binding site model. *J. Mol. Graph. Model.* **45**, 26–37 (2013).
89. Lacey, E. & Gill, J. H. Biochemistry of benzimidazole resistance. *Acta Trop.* **56**, 245–262 (1994).
90. Lucantoni, L. *et al.* Transmission blocking activity of a standardized neem

(Azadirachta indica) seed extract on the rodent malaria parasite Plasmodium berghei in its vector Anopheles stephensi. *Malar. J.* **9**, 1–10 (2010).

91. Tapanelli, S. *et al.* Transmission blocking effects of neem (Azadirachta indica) seed kernel limonoids on Plasmodium berghei early sporogonic development. *Fitoterapia* **114**, 122–126 (2016).
92. Sindew, R. E. Azadirachtin Disrupts Formation of Organised Microtubule Arrays during Microgametogenesis of Plasmodium berghei. **49**, (2002).
93. Chaccour, C., Hammann, F. & Rabinovich, N. R. Ivermectin to reduce malaria transmission I. Pharmacokinetic and pharmacodynamic considerations regarding efficacy and safety. *Malar. J.* **16**, 1–16 (2017).
94. de Carvalho, L. P. *et al.* Ivermectin Impairs the Development of Sexual and Asexual Stages of Plasmodium falciparum In Vitro . *Antimicrob. Agents Chemother.* **63**, 1–9 (2019).
95. Nasveld, P., Russell, B., Kotecka, B. & Rieckmann, K. Lack of in vitro effect of ivermectin on Plasmodium falciparum. *Southeast Asian J. Trop. Med. Public Health* **34**, 552–553 (2003).
96. Wagstaff, K. M., Sivakumaran, H., Heaton, S. M., Harrich, D. & Jans, D. A. Ivermectin is a specific inhibitor of importin α/β-mediated nuclear import able to inhibit replication of HIV-1 and dengue virus. *Biochem. J.* **443**, 851–856 (2012).
97. Vemu, A., Atherton, J., Spector, J. O., Moores, C. A. & Roll-Mecak, A. Tubulin isoform composition tunes microtubule dynamics. *Mol. Biol. Cell* mbc.E17-02-0124 (2017). doi:10.1091/mbc.E17-02-0124
98. Valenstein, M. L. & Roll-Mecak, A. Graded Control of Microtubule Severing by Tubulin Glutamylation. *Cell* **164**, 911–921 (2016).
99. Levy, D. L. & Heald, R. Mechanisms of Intracellular Scaling. *Annu. Rev. Cell Dev. Biol.* **28**, 113–135 (2012).
100. De, S., Tsimounis, A., Chen, X. & Rotenberg, S. A. Phosphorylation of α-tubulin by protein kinase C stimulates microtubule dynamics in human breast cells. *Cytoskeleton* **71**, 257–272 (2014).
101. Ori-McKenney, K. M. *et al.* Phosphorylation of β-Tubulin by the Down Syndrome Kinase, Minibrain/DYRK1a, Regulates Microtubule Dynamics and Dendrite Morphogenesis. *Neuron* **90**, 551–563 (2016).

102. Ti, S., Kapoor, T. M., Ti, S., Wieczorek, M. & Kapoor, T. M. Purification of Affinity Tag-free Recombinant Tubulin from Insect Cells Purification of Affinity Tag-free Recombinant Tubulin from Insect Cells. *STAR Protoc.* 100011 doi:10.1016/j.xpro.2019.100011
103. Ma, C. *et al.* Mutations in alpha-tubulin confer dinitroaniline resistance at a cost to microtubule function. *Mol. Biol. Cell* **18**, 4711–20 (2007).
104. Hyman, A. A., Salser, S., Drechsel, D. N., Unwin, N. & Mitchison, T. J. Role of GTP Hydrolysis in Microtubule Dynamics : Information from a Slowly Hydrolyzable Analogue , GMPCPP. **3**, 1155–1167 (1992).
105. Szkop, M., Kliszcz, B. & Kasprzak, A. A. A simple and reproducible protocol of glass surface silanization for TIRF microscopy imaging. *Anal. Biochem.* **549**, 119–123 (2018).
106. Schindelin, J. *et al.* Fiji: An open-source platform for biological-image analysis. *Nat. Methods* **9**, 676–682 (2012).
107. Gardner, M. K. *et al.* Rapid microtubule self-assembly kinetics. *Cell* **146**, 582–592 (2011).
108. Vemu, A., Garnham, C. P., Lee, D. Y. & Roll-Mecak, A. *Generation of differentially modified microtubules using in vitro enzymatic approaches*. *Methods in Enzymology* **540**, (Elsevier Inc., 2014).

Conferences, Courses, and Other Events

Conferences and Retreats

IRTG2290 Kickoff Meeting 2017

Deutsche Gesellschaft für Zellbiologie Conference 2018, Charite

- Presented a poster and a short talk

ZIBI Retreat 2018

- Presented a talk and a poster

Australian Society for Parasitology Conference 2018

- Presented a poster

Kioloa Retreat 2018

ZIBI Retreat 2019

- Held a chalk talk

DivIDE conference 2019, Centre for Genomic Regulation, Barcelona

- Presented a poster

IRTG Stellenbosch Symposium 2019

- Presented a talk
- Chaired a session

IRTG Retreat 2020

- Presented a talk

Courses and Workshops

05. – 08.09.2017	Confocal Microscopy Course, the University of York
23. – 25.10.2017	Introduction to Image Analysis, MPI-CBG Dresden
04. – 07.2020	Writing for Publication Workshop with Iain Patten
13.07 + 20.07.2020	Science Graphics Workshop with Thomas Fetter
04.09.2020	Good Scientific Practice Minisymposium

Teaching

07.06.2019	Beuth Hochschule für Technik. One hour lecture on malaria and thesis project

DOI of this thesis: https://doi.org/10.18452/22956